Master's thesis

NTNU
Norwegian University of Science and Technology
Faculty of Natural Sciences
Department of Materials Science and Engineering

Ragnhild Hyllnes Klaussen

Flexible, biocompatible lead-free piezoelectric thin films for biomedical applications

Master's thesis in Chemical Engineering and Biotechnology
Supervisor: Tor Grande
July 2019

NTNU
Norwegian University of
Science and Technology

Ragnhild Hyllnes Klaussen

Flexible, biocompatible lead-free piezoelectric thin films for biomedical applications

Master's thesis in Chemical Engineering and Biotechnology
Supervisor: Tor Grande
July 2019

Norwegian University of Science and Technology
Faculty of Natural Sciences
Department of Materials Science and Engineering

NTNU
Norwegian University of
Science and Technology

Preface

This thesis is submitted to the Norwegian University of Science and Technology in the course TMT4900 Materials Chemistry and Energy Technology, Master's Thesis, as a part of the Master of Science degree in Materials Science. Professor Tor Grande has supervised this project, and Ph.D. candidate Nikolai Helth Gaukås has served as co-supervisor.

The precursor solutions were prepared and characterised in laboratories at the Department of Materials Science and Engineering (IMA) at NTNU and the thin films were manufactured in NTNU NanoLab. The BT precursor was prepared by Ph.D. candidate Kristine Bakken. The IR measurements were conducted in cooperation with Ph.D. candidate Kristine Bakken. The KNN thin film on a SiPt substrate was prepared by Ph.D. candidate Nikolai Helth Gaukås. The preparation of the KNN precursor solution and deposition of platinum electrodes were conducted in cooperation with Ph.D. candidate Nikolai Helth Gaukås. The author performed all the other work presented in this thesis.

Trondheim 01 July 2019

Ragnhild Hyllnes Klaussen

Acknowledgements

I would first like to thank my supervisor, Professor Tor Grande, for your guidance and motivation throughout this project. I know how busy you are, yet you always set aside time for our weekly meetings. The feedback has been valuable to me, and you have restrained me when I get overeager and managed to see the positive side of not always positive results.

Secondly, I would like to thank my awesome co-supervisor, Ph.D. candidate Nikolai Helth Gaukås for helping and continually pushing me towards the end goal. I am particularly grateful for the company during lab work (including weekends!) as well as the bad jokes along the way. I would not have managed this without your friendly support.

Huge thanks to my partner for supporting me throughout the semester and for coming all the way from Oslo to make me dinner and do the laundry, especially during the final weeks of the project. I also want to thank my partner’s father, Jarle Leirpoll, for designing the illustrations of a piezoelectric energy harvester on a heart.

I want to thank the Functional Materials and Materials Chemistry (FACET) Research Group for helpful discussions and feedback on my presented results during group meetings. I wish to thank Ph.D. candidate Kristine Bakken for her help with the BT precursor solution, IR spectroscopy and helpful discussions. Thanks to Julian Walker for valuable input and Silje Marie Dale for valuable advice during the project. I am also grateful for the help with XRD plots given by Trond Brandvik and Susanne Linn Skjærvø. I would also like to thank my fellow students in the fourth-floor study hall in K2. Coffee, chocolate and a lot of laughter got us through the semester!

Finally, I would like to thank the technical staff at NTNU NanoLab and the Department of Materials Science and Engineering. Their guidance and help with the equipment have been crucial for a rookie master student like me. Mathilde Barriet at NTNU NanoLab deserves an honourable mention for valuable assistance with equipment and questions during the project.

Abstract

In this project phase pure, piezoelectric ceramic thin films were deposited on a thermally robust substrate using chemical solution deposition (CSD) and successfully transferred onto a polymer support. Dense oxide thin films require annealing at high temperatures, where most polymers decompose. Therefore, the ceramic film must first be grown on a thermally robust substrate and then transferred onto the polymer using a release layer.

Ten layers of zinc oxide (ZnO) solution were deposited and grown on a thermally robust platinum coated silicon (SiPt) substrate using CSD. The result was a dense and uniform thin film, that constituted the release layer. The same approach was used to deposit two layers of barium titanate (BT) solution on top of the ZnO thin film. Ten layers of potassium sodium niobate (KNN) solution were deposited on top of the BT thin film and formed a dense and uniform piezoelectric thin film. On top of the KNN thin film, a platinum bottom electrode was deposited. A few drops of polydimethylsiloxane (PDMS) were spin-coated on top of the Pt electrode and cured in room temperature for seven days. The curing of PDMS in room temperature prevented fractures in the ceramic thin film induced by shrinkage of the PDMS layer. The ZnO layer was etched away by immersing the sample stack (PDMS-Pt-KNN-BT-ZnO-SiPt) in 33 % acetic acid, preheated to 60 °C. Due to fracturing of the flexible piezoelectric thin film before deposition of Pt top electrodes, the ferroelectric measurements showed a leaking ferroelectric *P-E* hysteresis loop for the flexible thin film.

It was also observed that when KNN is deposited directly onto a ZnO thin film, $K_4Nb_6O_{17}$ will nucleate in addition to $K_{0.5}Na_{0.5}NbO_3$. Nucleation of $K_4Nb_6O_{17}$ was not affected by changing the atmosphere from pure O_2 to an 80/20 mixture of N_2 and O_2, however, increasing the annealing temperature from 700 °C to 750 °C resulted in the formation of a new secondary phase; $K_2Nb_4O_{11}$. Introducing an intermediate layer of BT in between the zinc oxide layer and the KNN film was crucial to avoid nucleation of secondary phases of KNN and hence contribute to producing a phase pure KNN thin film. The ZnO induced island growth of BT, but this did not seem to affect the resulting thin film considerably.

The experimental procedure proved successful to prepare dense, phase pure KNN thin films with electrodes on a polymer support.

Sammendrag

I dette masterprosjektet ble fleksible, faserene, piezoelektriske kalium-natrium niobat (KNN) tynnfilmer produsert ved å legge en KNN tynnfilm på et termisk stabilt substrat og deretter overføre filmen til en fleksibel polymer. For å oppnå høy tetthet i keramiske tynnfilmer må de varmebehandles på høy temperatur. Dette betyr at man ikke kan legge oksidfilmer direkte på et fleksibelt polymersubstrat ettersom polymeren vil smelte under varmebehandlingen. For å oppnå keramiske filmer med høy tetthet må man derfor legge filmen på et midlertidig lag på toppen av et termisk stabilt substrat, og deretter fjerne dette midlertidige laget når polymeren har herdet på overflaten til keramfilmen. På denne måten unngår man at polymeren smelter under prosessen og man får en keramfilm på et fleksibelt polymersubstrat.

Sinkoksid (ZnO)-løsning ble spin-coatet på et termisk stabilt platinabelagt silisiumsubstrat og pyrolysert på 550 °C. Etter 10 lag med ZnO, ble filmen sintret på 700 °C, og denne ZnO tynnfilmen utgjorde det midlertidige laget. To lag med barium titanat (BT) ble lagt på ZnO filmen på samme måte som beskrevet over. En uniform tynnfilm med høy tetthet bestående av 10 lag KNN-løsning ble lagt oppå BT laget, etterfulgt av en platina bunnelektrode på toppen av KNN laget. Noen få dråper med polydimetylsiloksan (PDMS) ble spin-coatet på platinalaget og herdet i romtemperatur i syv dager. Da PDMS-laget var ferdig herdet, ble ZnO-laget etset bort ved å putte hele stabelen i 33 % eddiksyre, forvarmet til 60 °C. PDMS-Pt-KNN-BT laget ble frigjort fra silisiumsubstratet og platina toppelektroder ble lagt på BT-KNN-overflaten. På grunn av uforsiktig behandling av den keramiske tynnfilmen ble den knust før toppelektrodene ble lagt på, noe som medførte svake ferroelektriske hystereseløkker med lekkstrøm.

Det ble observert at sinkoksid fremmer vekst av sekundærfasen $K_4Nb_6O_{17}$ når KNN-løsning legges direkte på sinkoksid. Dannelsen av $K_4Nb_6O_{17}$ ble ikke påvirket av å endre atmosfæren i ovnen fra ren O_2 til en 80/20 blanding av N_2 og O_2, men ved å øke sintringstemperaturen fra 700 °C til 750 °C ble det dannet en ny sekundærfase; $K_2Nb_4O_{11}$.

Metoden viste seg å være en suksess for å lage faserene KNN tynnfilmer på en fleksibel polymer.

List of Abbreviations

BT	$BaTiO_3$
CA	Citric acid
CSD	Chemical solution deposition
d	Piezoelectric coefficient
EDTA	Ethylenediaminetetraacetic
GI-XRD	Grazing Incidence X-Ray Diffraction
KNN	$K_{0.5}Na_{0.5}NbO_3$
MA	Malic acid
MBP	Morphotropic phase boundary
NAmOx	Ammonium niobate (V) oxalate hydrate
P	Polarisation
PDMS	Polydimethylsiloxane
PPT	Polymorphic phase transition
P_R	Remnant polarisation
P_S	Saturation polarisation
Pt	Platinum
PZT	$Pb(Zr_{1-x}Ti_x)O3$
SEM	Scanning Electron Microscopy
SiPt	Platinum coated silicon, $Pt/TiO_2/SiO_2/Si$
σ	Stress
T_C	Curie temperature

Table of contents

1 Introduction

1.1 Background

The piezoelectric effect establishes a relation between mechanical stress and polarisation [1]. Since the French brothers Jacques and Pierre Curie discovered the piezoelectric effect in 1880, piezoelectric devices have become ubiquitous [2]. The effect is exploited in a variety of modern applications like transducers, actuators, igniters, sensors and pumps [1, 3, 4].

Today, the dominating piezoelectric materials are the lead zirconate titanates (PZT) [3]. Compared to other piezoelectric materials, the PZTs have superior piezoelectric properties and a wide operating temperature range. The European Union has restricted the amount of lead in electronic devices because of its toxic effects on the environment and on health such as causing severe disorders in the central nervous-, the hepatic- and the hematopoietic system [5, 6]. The severe health risks induce a demand for lead-free replacements as PZT based ceramics contain more than 60 wt % toxic lead [4, 7, 8]. Simultaneously, such lead-free piezoelectric materials initiate a new application for piezoceramics within biomedical applications [9, 10].

One of the most studied classes of the lead-free piezoelectric materials are the potassium sodium niobates (KNN) [3, 8]. KNN-based ceramics do not contain any harmful elements and are thus suitable for biomedical applications [3]. These alkaline niobate ceramics cannot fully replace PZT but can serve as an appropriate alternative for specific applications [4]. A novel and environmentally friendly aqueous-based method to synthesise KNN, avoiding the use of the hazardous solvent 2-Methoxyethanol, has recently been developed by the FACET research group [11]. This procedure was applied to prepare KNN in this work.

Flexible piezoelectric thin films give advantages in energy harvesting, actuating and sensing applications, and can be used in health monitoring on structures with complex geometry [12]. The latter is illustrated in Figure 1.1, where a flexible piezoelectric thin film is used as an energy harvester producing electric energy to a sensor monitoring heartbeats. The main challenge with flexible films with a polymer support is being able to directly synthesise the ceramic thin film on the polymer [12, 13]. Oxides generally require a crystallisation temperature above 400 °C, and most polymers decompose at temperatures exceeding 200 °C [12-16].

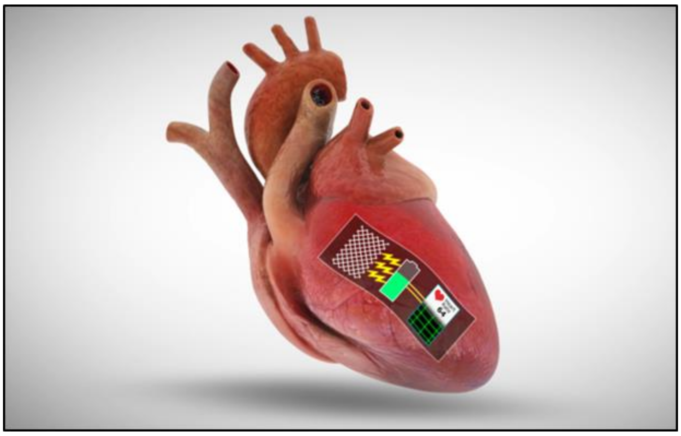

Figure 1.1: Illustration of a flexible piezoelectric thin film for use in biomedical applications. Here, the thin film is used as an energy harvester to supply electricity to a sensor monitoring heart rate.

In 2017, Liu et al. [12] reported on an approach to prepare high-temperature crystallised PZT thin films on a polymer substrate. The approach includes a transfer mechanism where the PZT thin films are first grown on a thermally robust substrate, silicon, with zinc oxide as a release layer in between. A polymer layer was added on top of the PZT thin film, and the sample stack was immersed in 33 % acetic acid, preheated to 60 °C. The zinc oxide layer was etched away by the acetic acid, successfully releasing the ceramic PZT thin film on the polymer support from the silicon substrate. This procedure was applied in this project to prepare flexible KNN thin films.

1.2 Aim of project

The motivation for this project was to achieve a greater understanding of the synthesis of flexible ceramic thin films and how they can be utilised in biomedical applications. The aim was to prepare phase pure KNN thin films on flexible polymer supports for use as energy harvesters in vivo, based on the method established in the specialisation project [17].

The first and most important objective in this project was to deposit phase pure KNN on top of a zinc oxide (ZnO) release layer. The second objective was to deposit noble metal bottom electrodes on the KNN thin film for ferroelectric measurements. The curing conditions for the flexible polymer support layer was established in the third objective, followed by determining the conditions for a successful release process in the fourth objective by immersing the sample stack into acetic acid. After the release process, the final objectives were to deposit top electrodes and conduct ferroelectric measurements on the flexible ceramic thin film. X-Ray diffraction (XRD), scanning electron microscopy (SEM) and infrared (IR) spectroscopy were used to characterise the samples.

2 Literature review

2.1 Piezo- and ferroelectricity

Piezoelectric materials are a group of solids where spontaneous polarisation can occur in response to applied mechanical stress, unlike other dielectrics where the polarisation would be zero at the same conditions [18, 19]. The piezoelectric effect establishes a relation between mechanical stress and polarisation [1]. The direct piezoelectric effect occurs when a piezoelectric material is exposed to mechanical stress such as pressure and an electric charge develops at the surface [1, 18, 19]. The reversible effect is called the inverse or converse piezoelectric effect and occurs when the material is subjected to an electric field, causing a change in the crystal structure. The piezoelectric effect can be observed in crystal structures that lack a centre of symmetry [1, 18]. This applies to 20 of the 32 different crystal symmetry classes that describe the internal symmetry of a crystal. The piezoelectric effect is illustrated in Figure 2.1.

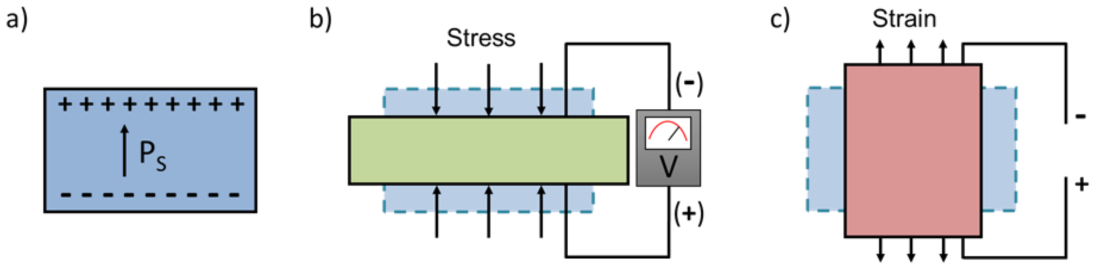

Figure 2.1: Illustration of the piezoelectric effect. a) A material with internal polarisation, P_S. b) The direct piezoelectric effect: generation of an electric charge due to applied mechanical stress. c) The converse piezoelectric effect: generation of strain due to the applied electric field.

The cubic perovskite crystal and a tetragonal perovskite crystal with the chemical formula ABO_3 are illustrated in Figure 2.2. The cubic structure is centrosymmetric, exhibiting no piezoelectric effect (Figure 2.2 a)) and the tetragonal structure is non-centrosymmetric, exhibiting the piezoelectric effect (Figure 2.2 b)) [20]. The polarisation is caused by formation of internal dipoles due to displacement of ions.

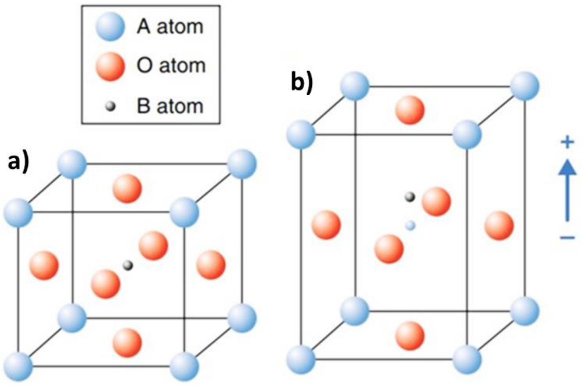

Figure 2.2: The perovskite crystal structure with the chemical formula ABO_3 illustrating the piezoelectric effect. a) The paraelectric, cubic crystal structure exhibiting no piezoelectric polarisation. b) The non-centrosymmetric, tetragonal crystal structure exhibiting the piezoelectric effect. The displacement of ions causes internal dipoles that give rise to piezoelectric polarisation [20, 21]. Reprinted with permission from [20].

Ferroelectric materials are a subset of piezoelectric materials, meaning all ferroelectrics are piezoelectric, but not all piezoelectric materials are ferroelectric [18]. Ferroelectrics are defined as materials with the ability to switch the direction of the spontaneous polarisation when subjected to an electric field and include many oxides with distorted perovskite structures [1, 18, 19]. In these structures, the cations are too small to fit inside the octahedra formed by the surrounding oxygen ions [18, 19]. This causes a displacement of cations to gain stability in the structure, hence giving rise to spontaneous polarisation and a dipole moment. The switching in polarisation in ferroelectric materials gives rise to a ferroelectric hysteresis loop that displays the behaviour of the polarisation, illustrated in Figure 2.3. Ferroelectrics display a saturation polarisation, P_S, at high voltage applied and a remnant polarisation, P_R, when the voltage is reduced to zero, while piezoelectric materials only display a saturation polarisation [18].

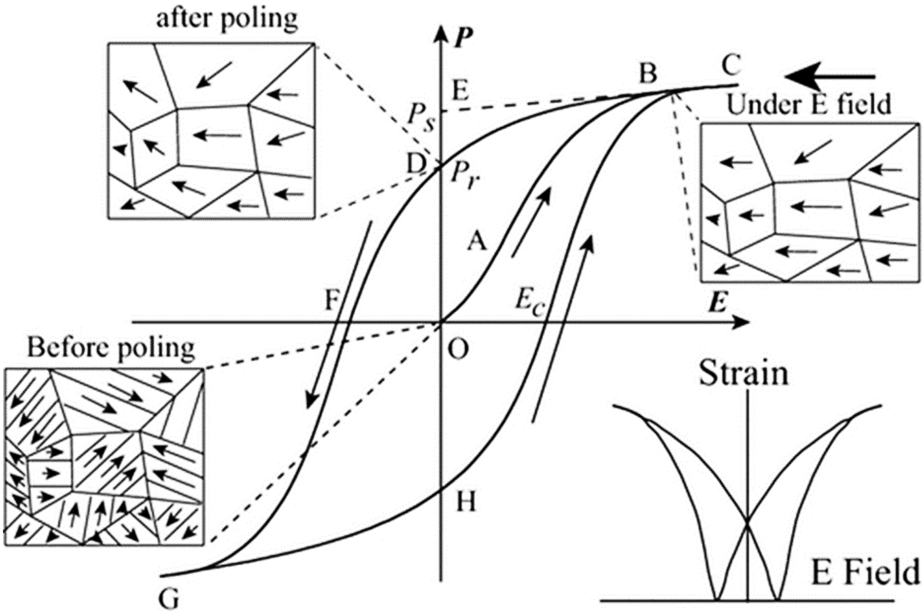

Figure 2.3: A ferroelectric hysteresis loop showing the behaviour of the polarisation, *P*, with the applied electric field, *E*. Reprinted with permission from [22].

The Curie temperature, T_C, and the piezoelectric coefficient, *d*, are important figures of merit for ferroelectric materials [18, 19]. The Curie temperature is the transition temperature where a ferroelectric material becomes paraelectric, and spontaneous polarisation no longer occurs. A high $\mathrm{T_C}$ gives a broader operation temperature range for the ferroelectric material [19]. The cubic structure in Figure 2.2 a) is the ferroelectric material above $\mathrm{T_C}$ and the distorted structure in Figure 2.2 b) is the material below $\mathrm{T_C}$.

The relationship between the polarisation, *P*, and the applied stress σ is described by the piezoelectric coefficient, *d* [3, 18]. The definition of the coefficient is complex because the polarisation depends on both the direction and the magnitude of the stress, however, the simplified definition presented in Equation 2-1 can often be used [18]. The units are $\mathrm{pCN^{-1}}$ for the direct piezoelectric effect and $\mathrm{pmV^{-1}}$ for the inverse effect.

$$d = \frac{P}{\sigma} \qquad 2\text{-}1$$

Lead zirconate titanate (PZT) perovskites with the formula $Pb(Zr_{1-x}Ti_x)O_3$ are the most commonly used ferroelectric materials [3, 18, 19]. PZT is a solid solution of lead titanate ($PbTiO_3$) and lead zirconate ($PbZrO_3$), and due to its flexibility in terms of compositional modifications, it can be utilised in most piezoelectric applications [3, 23]. The binary phase diagram of the $PbZrO_3$-$PbTiO_3$ system is illustrated in Figure 2.4. A vertical phase boundary is observed in the diagram around the composition $x = 0.48$ in $Pb(Zr_{1-x}Ti_x)O_3$ separating the rhombohedral and the tetragonal phases [18, 24]. Such a phase transition determined by the change in chemical composition and independent of temperatures is called a morphotropic phase boundary (MPB) [3, 18]. Dielectric and piezoelectric properties like the piezoelectric coefficient, dielectric permittivity and coupling factor are maximised at the MPB because the boundary allows two phases to coexist.

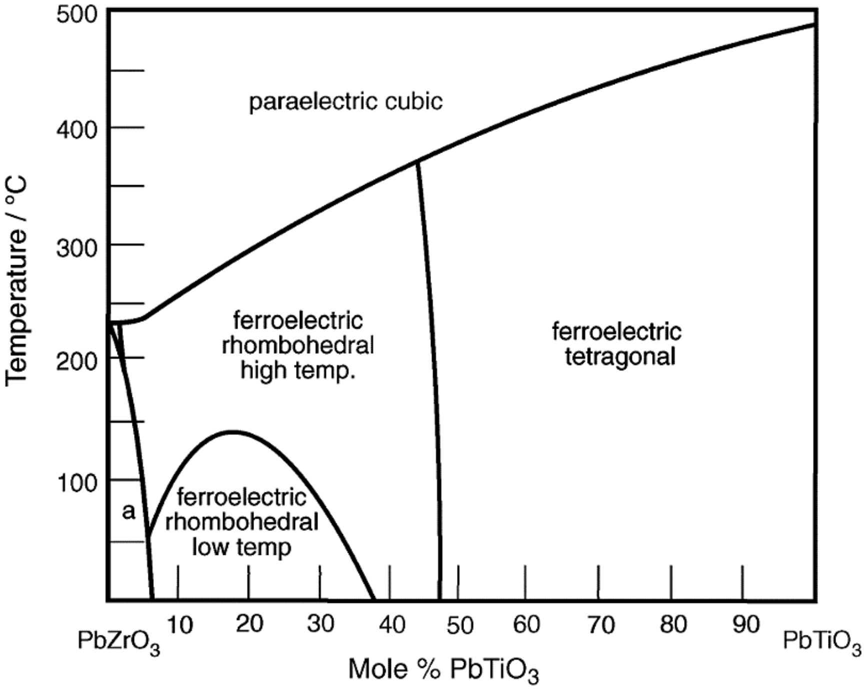

Figure 2.4: The binary phase diagram of the $PbZrO_3$-$PbTiO_3$ system. The antiferroelectric phase is marked with “a”. A morphotropic phase boundary is observed around 48 mole % $PbTiO_3$, separating the tetragonal and the rhombohedral phases. Reprinted with permission from [18].

Because of their ability to convert mechanical energy to electrical energy and vice versa, piezoelectric materials are used as transducers in ultrasound imaging, sensors to detect stresses and in actuators to drive motors and to control fuel injection [3]. Ferroelectric thin films are often utilised in applications like high-frequency electrical components, computer memory (RAM) and microsystems [25]. PZT and $BaTiO_3$ thin films are commonly used in capacitors [19]. A more recent application for piezoelectric thin films is energy harvesting from the human body’s movement to supply implantable sensors with power [26].

2.2 Potassium sodium niobate

Potassium sodium niobate (KNN) was first discovered in the early 1950s and is a solid solution of sodium niobate ($NaNbO_3$) and potassium niobate ($KNbO_3$) [3, 8, 27]. Due to PZTs superior piezoelectric properties, the interest for KNN did not rise until 2004 when Saito et al. reported on textured KNN with piezoelectric properties (d_{33} ~ 416 pCN^{-1}) comparable to those of PZT [3, 8, 28]. After this breakthrough, publications on KNN-based piezoceramics increased, signalling KNN as one of the promising lead-free piezoceramic candidates [23]. KNN has the perovskite structure with potassium and sodium atoms on the A-site, niobium atoms placed on the B-site and oxygen atoms located at the face centred positions [21, 29]. The crystal structure of KNN is illustrated in Figure 2.5.

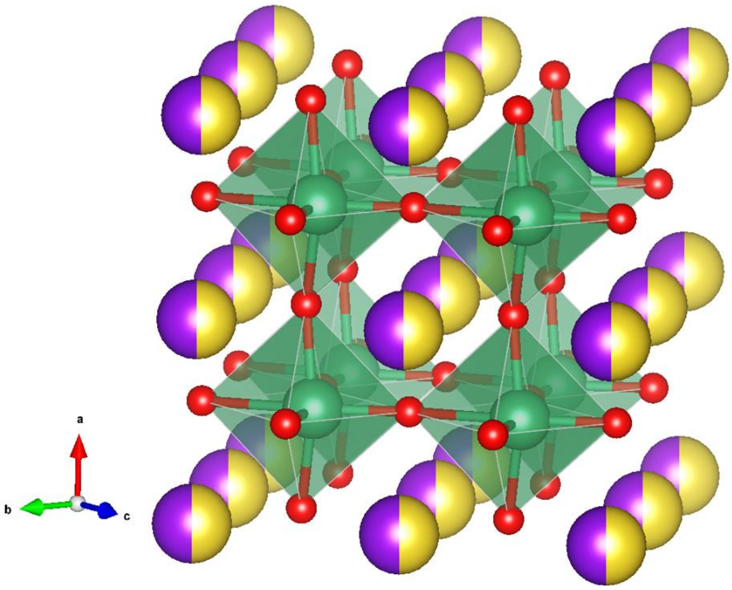

Figure 2.5: The potassium sodium niobate with the perovskite crystal structure. KNN has the potassium and sodium atoms placed on the A-site, represented with the purple and yellow colour respectively, green niobium atoms sit on the B-site, and the red oxygen atoms are located at the face centred positions. The structure is created using the VESTA software [30].

The binary phase diagram of the $KNbO_3$-$NaNbO_3$ system is illustrated in Figure 2.6 and contains a more complex polymorphism than the phase diagram of PZT [3, 23]. KNN appears in the following polymorphs with increasing temperature: rhombohedral (R), orthorhombic (O), tetragonal (T) and cubic (c) [23]. Enhanced piezoelectric properties are observed around the composition $K_{0.5}Na_{0.5}NbO_3$ [27, 31, 32], with T_C = 400 °C and d_{33} = 80-160 pCN^{-1} [3]. Some presume these features are a result of a MPB formed by two orthorhombic phases, while others believe the increased piezoelectric activity is ascribed to modification of the microstructure [28, 33-35]. The piezoelectric properties can further be increased by compositional modifications such as doping with e.g., lithium (Li) and antimony (Sb) on the A and B sites, respectively [28, 36].

The phase diagram also contains polymorphic phase transitions (PPTs) [3, 23, 28]. These phase boundaries depend on both temperature and composition. Together with the questionable MPB, they contribute to enhance piezoelectric and dielectric properties of KNN by allowing two phases to coexist, but MPBs is preferred since it is temperature independent. The MPB of the composition $K_{0.5}Na_{0.5}NbO_3$, is the vertical phase boundary separating the two orthorhombic phases F_{O1} and F_{O2} in the phase diagram in Figure 2.6.

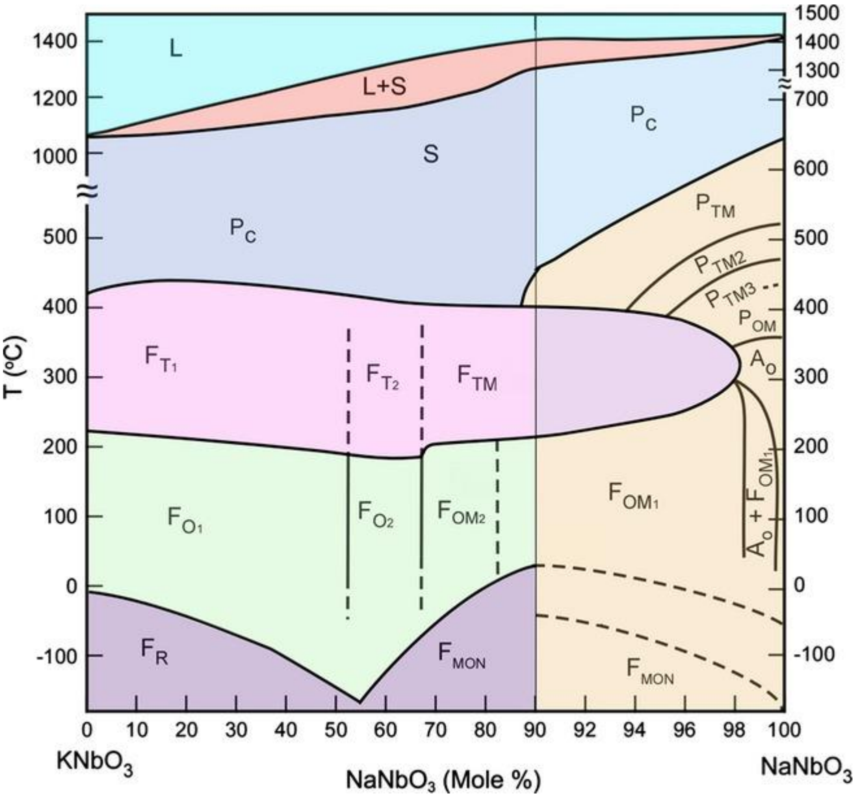

Figure 2.6: The binary phase diagram of the $KNbO_3$-$NaNbO_3$ system. KNN appears in the following polymorphs with increasing temperature: rhombohedral (R), orthorhombic (O), tetragonal (T) and cubic (c) [23]. Enhanced piezoelectric properties are observed around the composition 50 mole % $NaNbO_3$ with $T_C = 400$ °C [27, 31, 32]. Some assign these features to the presence of a MPB formed by two orthorhombic phases (F_{O1} and F_{O2}) [33, 35]. Reprinted with permission from [23].

2.3 Piezoelectric thin films in biomedical applications

Materials in biomedical applications are termed biomaterials [9, 10]. These are synthetic or modified natural materials used in restoration, diagnosis or as implants in the human body and have had a significant impact on multiple scientific fields and human health since the establishment of the field 70 years ago. The materials are required to be biocompatible, meaning they must be compatible with the surrounding body tissue. Additionally, it is desired that the materials are biostable or biodegradable, meaning they should retain their function throughout the lifetime of the patient or dissolve simultaneously as the cells rebuild a tissue without affecting the human body [9].

Piezoelectric materials are commonly used in biomedical applications, for instance, in sensors or transducers for ultrasound imaging [10, 26]. The latest technology in biomedical engineering is piezoelectric materials used in biosensing and bio-energy harvesting *in vivo* [37]. Heart rate monitors, pacemakers, implantable cardioverter defibrillators and neural stimulators are examples of today's implantable biomedical electronics [37-39]. These devices depend on battery power to operate, but the capability of these batteries is limited to a few years. A depleted battery can be replaced, however additional surgeries introduce health risks such as bleeding, infections and in worst-case mortality during the procedure. Thus, studies on more permanent power sources have increased [37-45].

Utilizing natural movements like heartbeat, blood flow, diaphragm activities and respiration movements, a flexible piezoelectric energy harvester can supply electrical energy to a pacemaker or sensor [38, 41, 44, 45]. An energy harvester *in vivo* utilizing the heartbeat to generate electric power and recharge a battery is illustrated in Figure 2.7. Over the past years, the energy requirement for pacemakers have decreased, and for modern pacemakers today the required power is approximately 1 µW [46]. This value corresponds well to the output powers of 1.1 µW and 1.6 µW measured for unimorph KNN/Si cantilevers and indicates KNN thin films are suitable candidates in energy harvesting [47, 48].

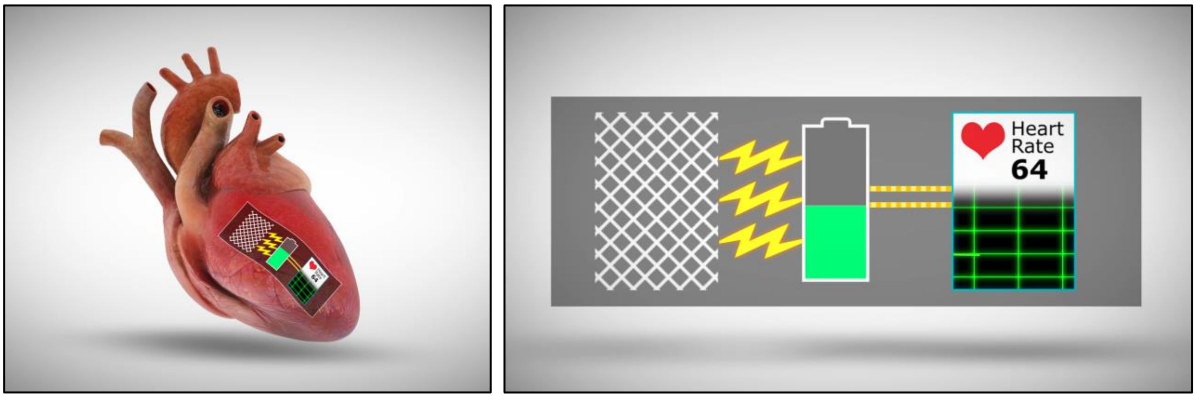

Figure 2.7: Illustration of a flexible piezoelectric thin film used as an energy harvester *in vivo* to convert the mechanical energy of the heart to electrical energy, recharging a battery supplying a sensor with power. The white lattice represents the flexible KNN thin film using heartbeats to generate electric energy, recharging a battery that can supply power to a sensor monitoring the heart rate.

In addition to biocompatibility, cost and toxicity are essential factors when selecting materials for piezoelectric thin films for biomedical applications [3]. A diagram with information on cost and toxicity of the different elements is illustrated in Figure 2.8 and may serve as a guideline when selecting elements. The elements are classified depending on toxicity and cost where green colour represents the non-toxic, yellow are the slightly toxic elements and orange are the acute toxic elements. Same colour division applies for the cost.

All elements in KNN, except potassium, are non-toxic, demonstrating that KNN is suitable for biomedical applications as potassium is only slightly toxic [3, 9]. PZT, on the other hand, consists of both toxic lead and slightly toxic titanium and depends on encapsulation in a biocompatible material before implanted in the body to isolate the toxic elements from the body fluids and tissue [38]. An encapsulation layer can prevent the degradation of the active material when exposed to harsh environments, but it will also reduce the output voltage of the piezoelectric thin film [49].

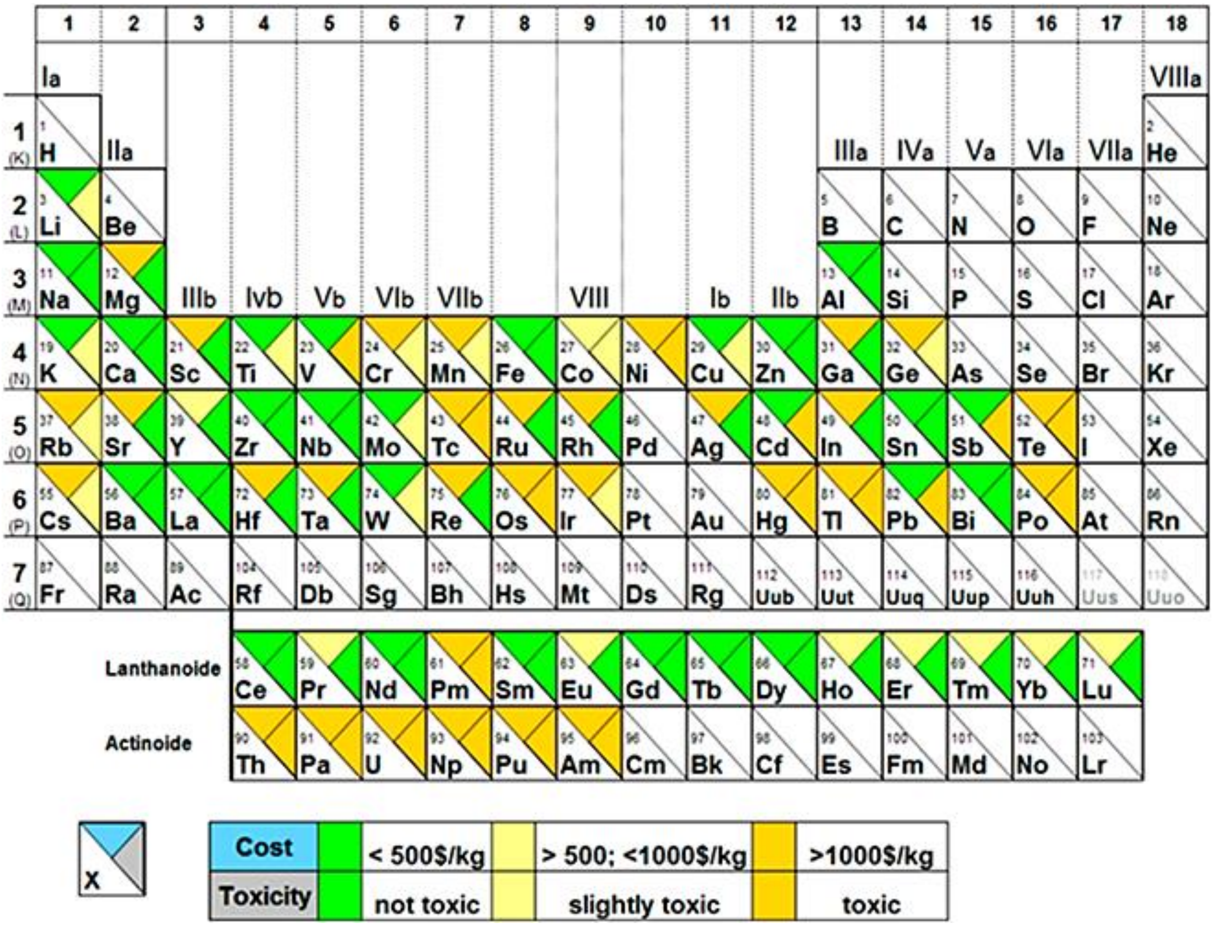

Figure 2.8: Diagram showing the cost and the toxicity of different elements. The elements are classified depending on toxicity and cost, where green colour represents non-toxic and low-cost materials, light yellow represents the slightly toxic and moderate costly materials and orange represents the acute toxic elements and high-cost materials. Reprinted with permission from [3].

2.4 Fabrication of flexible thin films

Flexible ceramic thin films can give advantages in actuating, energy harvesting and sensing applications due to their variety of functions based on dielectric, optical, electrical and chemical properties [13]. Ceramic thin films require crystallisation temperatures above 400 °C [12, 13]. This eliminates direct deposition on a polymer substrate as most polymers decompose at temperatures above 200 °C [12, 15, 16]. Low-temperature processed oxide thin films on plastics were first reported in the 1970s, where sputtering and vacuum evaporation were applied to prepare transparent, electrically conductive oxide (TCO) thin films on polymers [50, 51]. Since then, the rising interest and extensive research on flexible thin films have led to different synthesis routes for fabrication of flexible ceramic thin films such as vapor phase deposition, flame spray pyrolysis and wet processing techniques [13], illustrated in Figure 2.9.

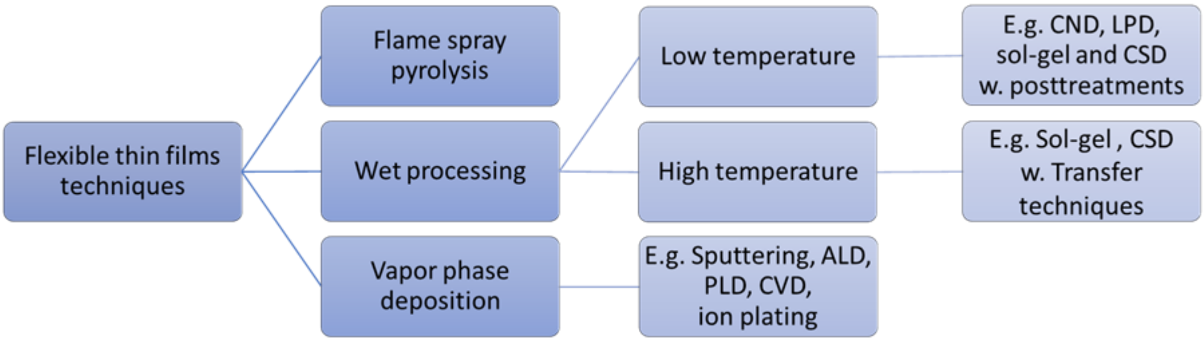

Figure 2.9: Overview of different techniques for preparing flexible ceramic thin films.

Vapour phase deposition (VPD) is deposition of chemical precursor solutions in vapour phase, forming a solid thin film [52]. VPD includes techniques like atomic layer deposition (ALD), sputtering, chemical vapour deposition (CVD), pulsed laser deposition (PLD) and ion plating [13, 52-55]. Thin films prepared by vapour phase deposition often need a posttreatment to improve the crystallinity of the films [13]. An example of such a posttreatment is hydrothermal treatment of an atomic layer deposited titania thin films [55].

Recently, Gockeln et al. [56] prepared flexible thin film electrodes for lithium-ion batteries utilizing flame spray pyrolysis (FSP). Pure and highly crystalline nanoparticles were directly deposited onto flexible substrates by using FSP, forming porous thin films. To increase the adhesion to the flexible substrate and the mechanical stability of the thin film, the porous layers were mechanically compressed after deposition. The result was flexible porous thin films successfully assembled in a lithium-ion battery cell.

Wet processing techniques are often divided into high- and low-temperature processing and include techniques like liquid phase deposition (LPD), sol-gel method, crystalline nanoparticle deposition (CND) and chemical solution deposition (CSD) [13, 57-59]. The advantage of wet processing techniques is that the thin films can be prepared under ambient temperature and atmosphere, and hence thin films with a larger area can be produced.

2.4.1 Low-temperature wet processing techniques

Wet processing enables methods to prepare ceramic thin films directly on plastics at low temperatures, and hence avoid decomposition of the polymer [13-15]. Oxide thin films prepared by low-temperature techniques often require posttreatment due to higher porosity compared to the films made by high-temperature techniques [13].

Liquid phase deposition (LPD) is a novel and simple technique to synthesise metal oxide thin films at low temperatures [58, 60-62]. The method is based on dipping a substrate into a supersaturated chemical solution that contains the desired metal ions. Metal oxides will precipitate and form a thin film on the substrate because of hydrolysis equilibrium reactions of the metal fluoro complexions and the consumption of fluoride ions with boric acid. Shimizu et al. [63] applied LPD to prepare TiO_2 thin films on flexible substrates. An aqueous solution of titanium tetrafluoride (TiF_4) was used as starting material and various flexible substrates like polymethylmethacrylate (PMMA) and polycarbonate (PC) were immersed into the solution and dried at 60 °C. The result was porous anatase thin films with a thickness up to 170 nm. The hydrophobic surface of the flexible substrate caused the thin films to peel off easily, inducing many cracks in the oxide film.

Crystalline nanoparticle deposition (CND) is a technique that avoids heating to crystallise the ceramic films by depositing already crystalline nanoparticles [13, 59]. The metal oxide nanoparticles can be deposited on the plastics by using e.g., spin- or dip coating followed by curing at low temperatures. CND was successfully applied by Königer and Münstedt [59] to prepare coatings of indium tin oxide (ITO) nanoparticles on various flexible polymers. The coated thin films exhibited better electrical properties under oscillatory bending than ITO coatings prepared by sputtering.

In the 1980s, the first oxide thin films were prepared using chemical solution deposition (CSD) [57]. A precursor solution is deposited on a substrate using different deposition techniques such as spray-, dip- or spin coating. The wet film is then converted into a ceramic thin film by drying, pyrolysis and finally heat treatment at high temperatures to increase the films density, initiate crystallisation and to improve the microstructure. The temperature of the thermal treatment is dependent on the thermal properties of the substrate. A schematic illustration of the different processing steps in CSD is shown in Figure 2.10.

The sol-gel method is a subset of CSD and is a versatile technique for preparing ceramic thin films with high purity [57, 64]. The method is based on a precursor solution containing the desired ions, which is converted into a thin ceramic film utilizing chemical reactions, drying, gelation of the precursor solution and curing of the film [57]. Aegerter and Al-Dahoudi [65] applied the sol-gel method and CND to prepare Sn-doped indium tin oxide (ITO) coatings on polymer substrates such as polycarbonate, polyamide and polyethylene [65]. The crystalline nanoparticles were dispersed in an ethanolic sol and deposited on the flexible substrates using spin- or dip coating. The gel films were later densified by a UV light radiation or by a low-temperature heat treatment. The results were ITO thin films successfully deposited on flexible substrates.

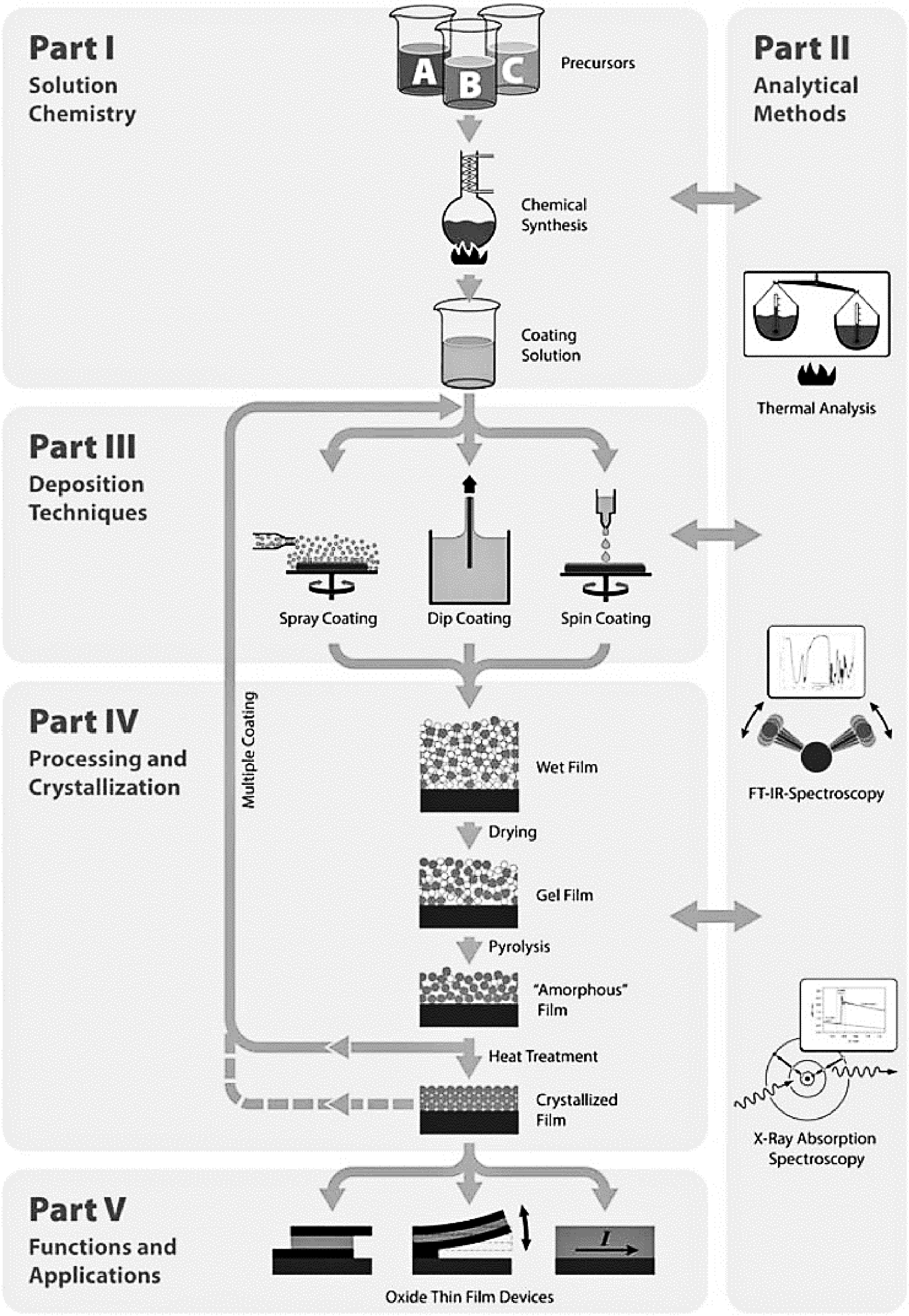

Figure 2.10: Schematic illustration of the five different stages in chemical solution deposition: solution chemistry, analytical methods, deposition techniques, processing and crystallisation and functions and applications. Reprinted with permission from [57].

For thin films prepared by CSD or sol-gel method, posttreatments like humid vapor treatment, UV-laser irradiation, hydrothermal treatment and IR-laser irradiation have successfully been applied to increase the crystallinity and the density of the films [13, 57, 65]. These posttreatments are not required for thin films prepared by CND or LPD techniques because the materials are crystalline before being deposited on the plastic substrate [13]. The different posttreatments are illustrated in Figure 2.11.

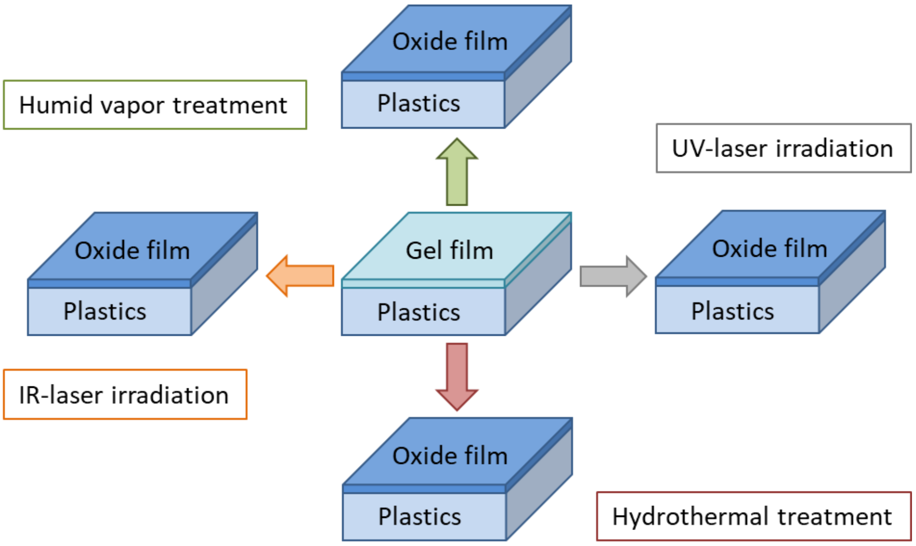

Figure 2.11: Illustration of four different posttreatment techniques for converting a gel film to an oxide thin film on plastics: humid vapor treatment, UV-laser irradiation, hydrothermal treatment and IR-laser irradiation [13].

Crystallisation induced by water vapour is the main feature in humid vapour treatment [13]. Imai et al. [66] reported porous and brittle anatase coating prepared by the sol-gel method followed by humid vapour treatment. Despite mechanical strength, the films were easily peeled off the substrate. In hydrothermal or hot water treatment, oxide thin films are formed by immersing a gel film into hot water [67]. The method has successfully been used to improve the crystallinity of anatase thin films on plastics [67, 68]. Irradiation with IR or UV lasers has also been demonstrated to induce crystallisation of oxide thin films deposited on plastics [69, 70].

2.4.2 High-temperature wet processing techniques

Common for the two methods reviewed in this section is a transfer mechanism that allows high-temperature crystallisation of the ceramic film [12, 13]. The two techniques involve deposition of the oxide film on a thermally robust substrate before transferring the film onto the flexible layer using a release layer.

H. Kozuka et al. [13] reported a lift-off technique in 2013 for high temperature crystallised titania (TiO_2) thin films based on the sol-gel method. Using a release layer, the ceramic thin film could be deposited, and heat treated on a thermally robust substrate such as silicon. The dense and crystalline oxide films were transferred onto plastic substrates using a thermally decomposable thin film as a release layer. Two different approaches were used to attach the ceramic film to the plastic substrate, one with an adhesive layer and one without. The two different procedures are illustrated in Figure 2.12.

Before the lift-off processes, a 2 µm thick polyvinylpyrrolidone (PVP) film was deposited by dip coating onto a silicon substrate and pyrolysed at 300 °C, to serve as a release layer [13]. A titania (TiO_2) film was deposited on the PVP film using spin coating and heat treated at 500 °C in a furnace. A cellophane adhesive tape was used to detach the TiO_2 film from the silicon substrate, illustrated in Figure 2.12 b). This resulted in crack formation across the entire titania film due to tension induced by the bending of the ceramic film during the release process. By using epoxy resin as an adhesive and a thick plastic substrate on top instead of the cellophane tape, the crack formation was prevented. After the separation process, the release layer was removed by a cellophane adhesive tape, leaving a dense, transparent titania film on the plastic substrate.

In the second lift-off process, illustrated in Figure 2.12 c), softened plastics were used as an adhesive layer between the titania thin film and the plastic substrate [13]. To soften the plastic surface, two different techniques were applied, one utilizing IR-light and one utilizing a hotplate. The heat was conducted from the silicon substrate to the plastic surface only softening the surface and not the entire plastic substrate. The soft plastic surface ensured good adherent of the ceramic film to the plastic. After cooling, the plastic layer was peeled off the silicon substrate leaving a crack-free titania thin film on the plastic substrate. H.Kozuka et al. concluded that the two transfer techniques, both using adhesives and softening the plastic layer, were viable methods to successfully prepare large-area and dense ceramic thin films on plastic substrates.

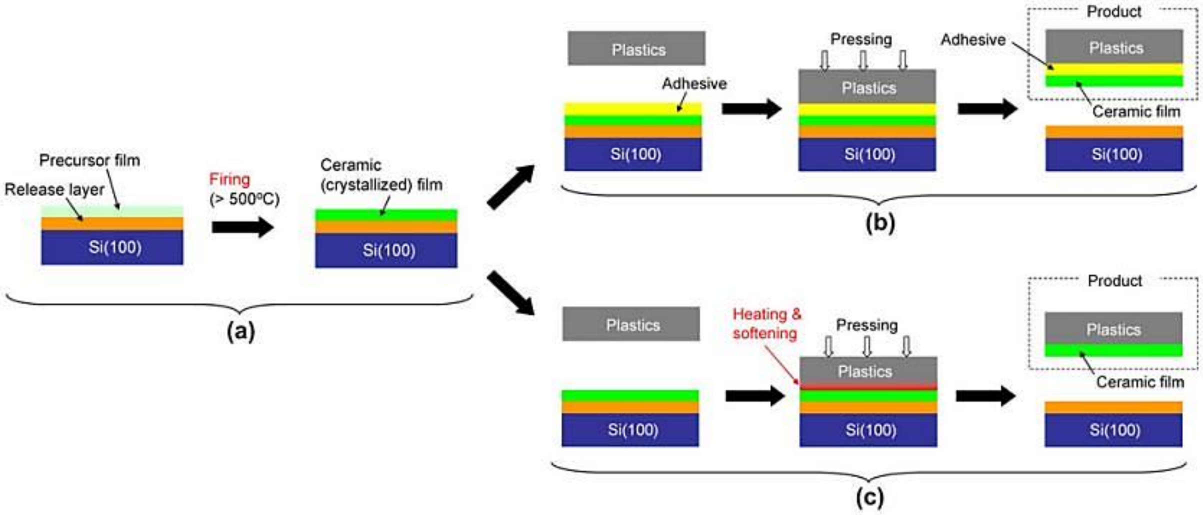

Figure 2.12: Illustration of the lift-off technique used for preparing high temperature crystallised titania thin film. a) Deposition of a release layer and the ceramic thin film on a thermally robust silicon substrate. b) The release process using an adhesive layer between the ceramic thin film and the plastic. c) The release process using heating and softening of the plastics as an adhesive layer. Reprinted with permission from [13].

In 2017, Liu et al. reported a transfer process for high temperature crystallised PZT thin films [12]. The films are first grown on a thermally robust substrate, such as silicon, and then transferred onto a polyimide support utilizing a zinc oxide (ZnO) film as a release layer in between the PZT film and the silicon substrate. Two different samples of PZT thin films were prepared, one released and one clamped thin film. The released film is the PZT-polyimide after separation from the silicon substrate and the clamped film refers to the constrained film before release from the silicon substrate. The latter was used to evaluate the traits of the flexible PZT thin film. The flow chart of the experimental procedure is illustrated in Figure 2.13 a).

In the synthesis, a 4 x 4 cm silicon piece was rinsed by sonicating the piece in acetone followed by isopropanol [12]. To remove any organic residues, the substrate was oxygen plasma cleaned. After cleaning, a 130 nm thick ZnO film was deposited by weak oxidant plasma enhanced atomic layer deposition (PEALD) at 200 °C with diethylzinc as a precursor. To cover the ZnO layer and serve as a diffusion barrier, PEALD was applied to deposit a 10 nm thick Al_2O_3 layer using trimethylaluminium (TMA) as a precursor. Two different platinum (Pt) electrodes were then deposited on top of the Al_2O_3 layer so that the characterisation of the clamped and the released films from the same PZT film could be compared. Patterned platinum top electrodes were deposited on the region for the released film and a blanket Pt electrode on the clamped area, both illustrated in Figure 2.13 b).

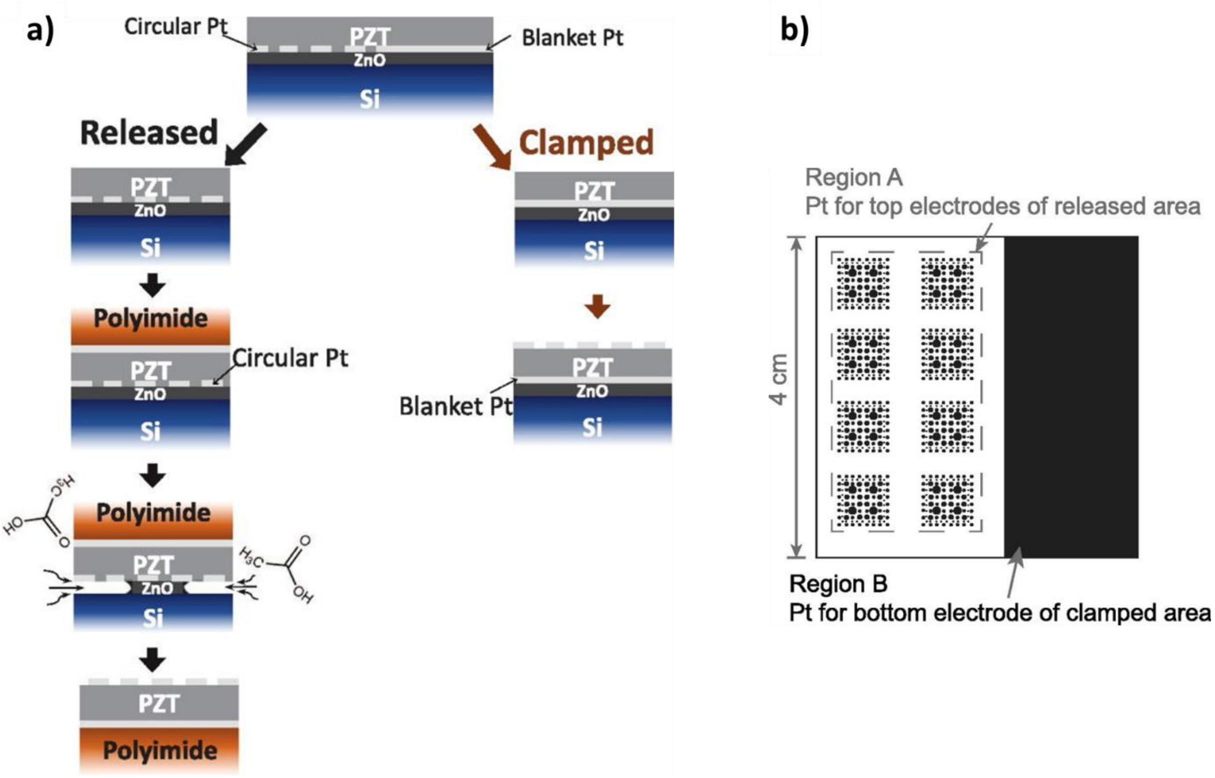

Figure 2.13: a) A flow chart illustrating the procedure for preparing the released and the clamped PZT thin film. The transfer process for the released thin film is shown on the left side, and the clamped thin film is illustrated on the right side used for comparison. b) Region A displays the pattern for the platinum top electrodes of the released area, and region B displays the platinum bottom electrode of the clamped area. Reprinted with permission from [12].

Chemical solution deposition was used to deposit the PZT thin film [12]. The PZT solution was spin-coated onto the substrate at 4000 rpm followed by hotplate baking at 100 °C for 1 min and hotplate pyrolysis at 300 °C for 3 min. Finally, the film was crystallised by rapid thermal annealing at 700 °C for 1 min. To reach the desired final film thickness, these steps were repeated ten to fifteen times until the thickness reached 0.8-1.1 µm. To convert any pyrochlore phases on the surface to the perovskite phase, a PbO chopping layer was added on the top of the PZT film.

After characterisation by X-ray diffraction (XRD) and field emission scanning electron microscopy (FESEM), the clamped and the released film were separated by cleaving the sample in two [12]. Circular Pt top electrodes were sputtered onto the PZT film to complete the clamped sample, while a Pt blanked electrode was deposited on the sample to be released. A 10-20 nm thick Al_2O_3 layer was deposited using PEALD followed by deposition of a 5 µm thick polyimide layer on top. The polyimide precursor was spin-coated on at 3000 rpm for 30 s, hotplate baked at 100 °C for 5 min and finally cured at 330 °C for 6 h. To separate the flexible PZT thin film from the silicon substrate, the ZnO layer was etched away by immersing the sample stack in 30 % acetic acid, preheated to 60 °C. The released PZT thin film was rinsed with deionised (DI) water and placed in a 0.26 M tetramethylammonium hydroxide bath to remove the alumina layer. Finally, the film was rinsed once more with DI water and blown dry.

The measurements revealed superior material properties for the released PZT film compared to the clamped film and confirm the correlation between improved domain wall mobility and reduced substrate clamping [12].

3 Experimental procedure

Two different experiments were conducted in this project. The first experiment sought to repeat the procedure developed by the author in the specialisation project [17] and the second experiment was based on the same procedure but included a few additional steps such as depositing an intermediate layer, as well as electrodes. Both methods are illustrated in Figure 3.1 1a)-1d) and 2a)-2f) respectively.

The initial step is the same for both procedures, a zinc oxide (ZnO) thin film is deposited on a platinum coated silicon (SiPt) substrate to serve as a release layer. Both methods also involve the same techniques and conditions for depositing a KNN thin film, curing of PDMS on top as a flexible support as well as the release process of the final KNN-PDMS stack. The key differences between the two procedures are presented below.

In the first procedure, the next step 1a) after depositing the ZnO release layer is to deposit a potassium sodium niobate (KNN) thin film on top of the ZnO layer. A flexible layer of polydimethylsiloxane (PDMS) is added on top of the KNN thin film and cured in room temperature (1b). The sample stack consisting of PDMS-KNN-ZnO-SiPt is then immersed in 33 % acetic acid, preheated to 60 °C (1c). Finally, the KNN thin film on PDMS support has separated from the rigid silicon substrate (1d).

The second procedure starts by depositing two layers of barium titanate (BT) on top of the ZnO film as an intermediate layer (2a). A KNN thin film is then deposited on top of the BT layer (2b) followed by deposition of a platinum (Pt) bottom electrode on top of the KNN thin film (2c). A flexible layer of PDMS is added on top of the platinum electrode and is left to cure at room temperature (2d). The sample stack consisting of PDMS-Pt-KNN-BT-ZnO-SiPt is then immersed in 33 % acetic acid, preheated to 60 °C (2e). Finally, Pt top electrodes are deposited onto the flexible BT-KNN-Pt sample with PDMS support (2f).

In the following sections, the second procedure, including deposition of an intermediate layer and electrodes, will be described.

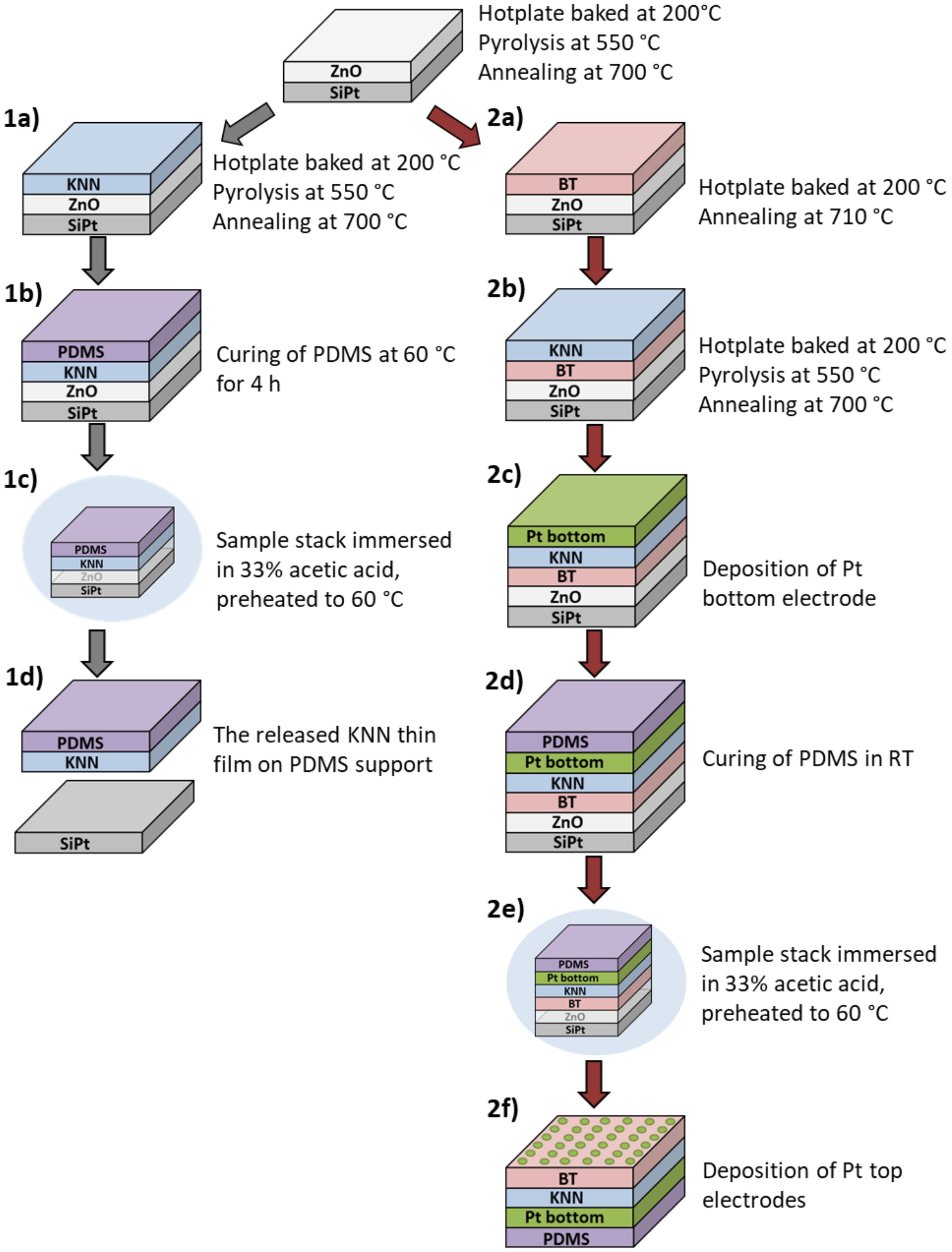

Figure 3.1: Illustration of the two experimental procedures applied in this project. The first step for both procedures is deposition of zinc oxide (ZnO) as a release layer on a platinum coated silicon piece. 1a) Deposition of a KNN thin film. 1b) Deposition of PDMS and curing. 1c) The release process in 33 % acetic acid. 1d) The released thin film. 2a) Deposition of a BT thin film. 2b) Deposition of a KNN thin film. 2c) Deposition of a platinum bottom electrodes on the thin film. 2d) Deposition of PDMS and curing. 2e) The release process in 33 % acetic acid. 2f) Deposition of a platinum top electrodes on the flexible thin film.

3.1 Preparation of solutions

A complete list of all the chemicals used to prepare the different solutions in this study is presented in Table 3-1.

Table 3-1: List of all the chemicals used to prepare the solutions in this study.

Chemical	Molecular formula	Purity	Supplier
Ammonia solution	NH_3	25 %	Merch KGaA
Ammonia solution	NH_3	30 %	Sigma Aldrich
Ammonium niobate (V) oxalate hydrate	$NH_4NbO(C_2O_4)_2 \cdot xH_2O$	99.99 %	Sigma Aldrich
Barium nitrate	$Ba(NO_3)_2$		Sigma Aldrich
Citric acid	$C_6H_8O_7$	$\geq$ 99.5 %	Sigma Aldrich
DL-malic acid	$C_4H_6O_5$	$\geq$ 99.0 %	Sigma Aldrich
Ethylenediaminetetraacetic acid	$C_{10}H_{16}N_2O_8$		Sigma Aldrich
Potassium nitrate	KNO_3	99.999 %	Sigma Aldrich
Sodium nitrate	$NaNO_3$	99.995 %	Sigma Aldrich
Sylgard 184 silicone elastomer	$(C_2H_6OSi)_n$		Dow Europe Gmbh
Ti-4-isopropoxide	$Ti[OCH(CH_3)_2]_4$		Sigma Aldrich
Zinc oxide	ZnO	$\geq$ 99.0 %	Sigma Aldrich

3.1.1 Zinc oxide

The zinc oxide (ZnO) precursor was prepared by dissolving ZnO in an aqueous solution with citric acid (CA) with a 1:1 molar ratio. A Zn^{2+}-precursor solution was achieved by dissolving 5.77 g of CA in 100 mL distilled water. 2.45 g of ZnO was added to the solution during vigorous stirring at 70 °C. The acidity was decreased by adding ammonia solution (25 %) to the point where the solution became transparent, approximately at pH = 9. The exact concentration of the solution was calculated from the final volume of the solution and the amount of ZnO used, and was determined to be ~ 0.28 M.

3.1.2 Barium titanate

The barium titanate (BT) solution was prepared by Kristine Bakken according to the procedure reported by Raeder et al. [71]. Dried barium nitrate ($Ba(NO_3)_2$) was dissolved in a solution with ethylenediaminetetraacetic acid (EDTA), ammonia solution (30 %) and deionised water at 60 °C and pH ~ 7. Citric acid (CA) was added to the solution as a second complexing agent. In the second solution, Ti-4-isopropoxide was added to a solution of CA and deionised water at 80 °C. The pH was adjusted to 7 by adding ammonia solution (30 %). Finally, the two solutions of Ba^{2+} and Ti^{4+} complexes were mixed in stoichiometric ratios to make the $BaTiO_3$ precursor solution. The concentration of the solution was calculated from the final volume of the solution and the amount of $Ba(NO_3)_2$ used and was determined to be ~ 0.13 M.

3.1.3 Potassium sodium niobate

The potassium sodium niobate solution was prepared with 5 % alkali excess according to the procedure reported by Gaukås et al. [72]. Ammonium niobate (V) oxalate hydrate (NAmOx) was mixed with DL-malic acid (MA) to prepare a niobate malic acid precursor. 36.45 g of NAmOx was weighed out and dissolved in 0.6 L distilled water preheated to 70 °C.

After continuous stirring at 70 °C for 3 h, all the powder was dissolved, and the pH was adjusted to 11 by adding ammonia solution (25 %). Niobic acid precipitated, and the solution was stirred at 70 °C for 2 h, before being aged at room temperature for 12 h. The solution was centrifuged at 10 000 rpm for 10 min and the oxalate-containing fluid was decanted. To remove any oxalate ion remains in the niobic acid, it was washed and centrifuged three times at 10 000 rpm for 20 min with ammonia solution (1 %). A 0.5 M DL-malic acid solution was prepared by dissolving 32.49 g of MA in 485.2 mL distilled water preheated to 70 °C. The washed niobic acid was added to the MA solution and stirred at 80 °C for 2 h, followed by stirring at 70 °C for 12 h. The pH was adjusted to 8 by adding ammonia solution (25 %). The concentration of the niobium solution was determined by thermogravimetric analysis by measuring the weight of Nb_2O_5 formed during thermal treatment. Five parallels were evaluated to ensure a reliable result. The temperature program for the analysis is illustrated in Figure 3.2. Finally, 0.9276 g of dried (150 °C, 24 h) potassium nitrate and 0.7799 g of dried (150 °C, 24 h) sodium nitrate was weighed out and dissolved in 200 g of niobium malic acid at 50 °C.

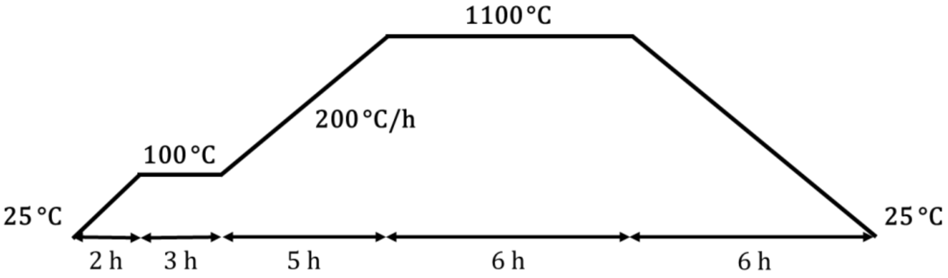

Figure 3.2: Temperature program for the thermogravimetric analysis of the niobium precursor solution. First, the solution is heated from 25 °C to 100 °C with a heating rate of 37.5 °C/h and held at 100 °C for 3 h. Then the precursor is heated from 100 °C to 1100 °C with a heating rate of 200 °C/h and held at 1100 °C for 6 h before cooling to room temperature.

3.1.4 Polydimethylsiloxane

Approximately 10 g of polydimethylsiloxane (PDMS) from Sylgard 184 silicone elastomer kit (Dow Europe Gmbh) was prepared by manually mixing the curing agent and the base in a plastic cup at a ratio 2:10. Using a vacuum desiccator connected to a membrane pump, the solution was degassed for 40 min to remove all the bubbles formed during mixing.

3.2 Deposition of oxide thin films

The oxide thin films were deposited on the platinum coated silicon ($Pt/TiO_2/SiO_2/Si$, SiPt) substrates using chemical solution deposition (CSD). 1 x 1 cm SiPt substrates were cleaned with acetone and isopropanol and blow-dried with air. The substrates were plasma cleaned to remove any organic residues and to increase the wettability of the substrates (Diener electronics, Femto). Directly after cleaning, a few drops of the precursor solutions were deposited on the substrates using a 1 mL syringe with a 0.2 µm filter. The solutions were deposited by spin coating at 3500 rpm for 40 s, using a spin coater (Laurell, WS-400B-6NPP-LITE/AS). The films were then dried on a hotplate at 200 °C for 3 min before pyrolysis in a rapid thermal processing (RTP) oven (Allwin21, AW610). These steps were repeated to the desired thickness was achieved before annealing in the RTP oven. The method is illustrated with KNN in Figure 3.3.

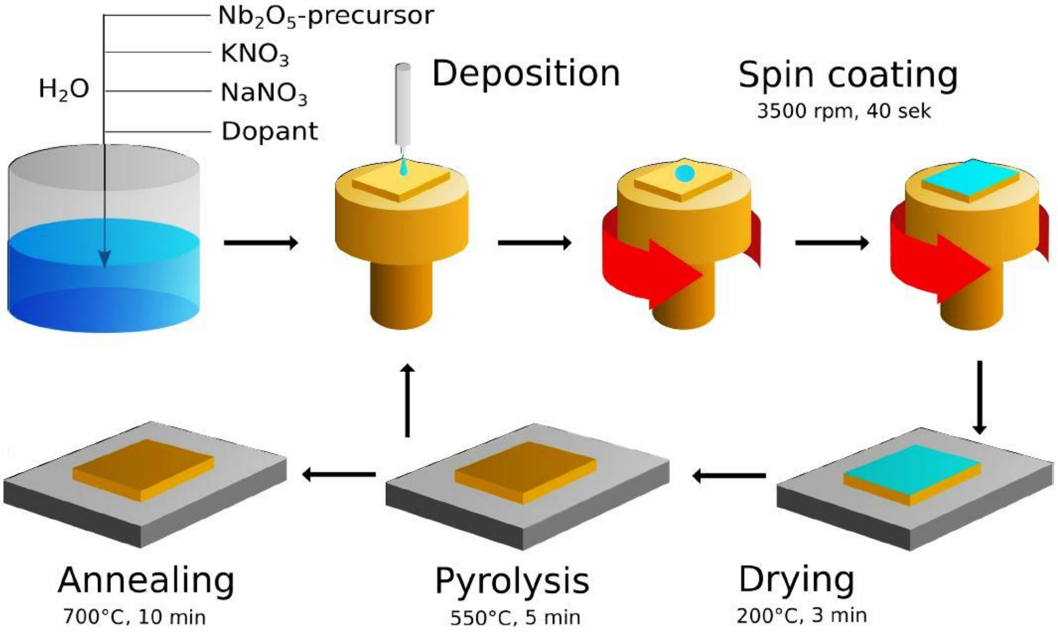

Figure 3.3: The CSD procedure for deposition of oxide thin films, here illustrated with KNN. The precursor solution is deposited on the platinum coated silicon piece and spin-casted. The wet film is then hotplate baked at 200 °C for 3 min and pyrolysed at 550 °C for 5 min. These steps are repeated until the desired thickness is reached and then the film is annealed at 700 °C for 10 min. Reprinted with permission from [73].

Using the procedure described above, a 100 nm thick (10 layers) ZnO thin film was deposited on a SiPt substrate and heat treated in an RTP oven with oxygen atmosphere. The film was pyrolysed at 550 °C for 5 min and annealed at 700 °C for 10 min. The temperature programs for the pyrolysis and the annealing step are illustrated in Figure 3.4 and Figure 3.5 respectively.

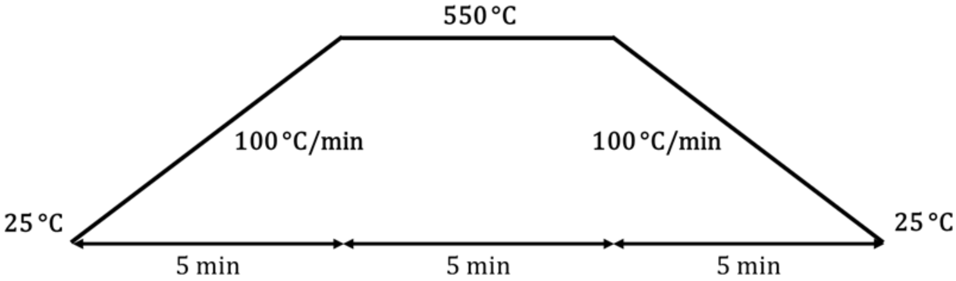

Figure 3.4: Temperature program for the pyrolysis step for the ZnO and KNN thin films in the RTP oven. The films are heated from room temperature to 550 °C with a heating rate of 100 °C/min. The temperature is held at 550 °C for 5 min before cooling to room temperature.

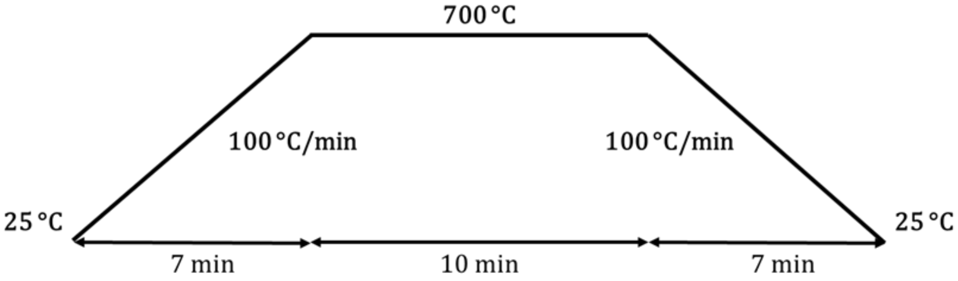

Figure 3.5: Temperature program for the annealing step for the ZnO and KNN thin films in the RTP oven. The films are heated from room temperature to 700 °C with a heating rate of 100 °C/min. The temperature is held at 700 °C for 10 min before cooling to room temperature.

Two layers of 0.13 M barium titanate (BT) solution were deposited on top of the ZnO film after plasma cleaning of the latter. The BT film was annealed in an RTP oven at 710 °C for 5 min with an atmosphere consisting of an 80/20 mixture of nitrogen and oxygen. The temperature program for the annealing of BT thin films is illustrated in Figure 3.6.

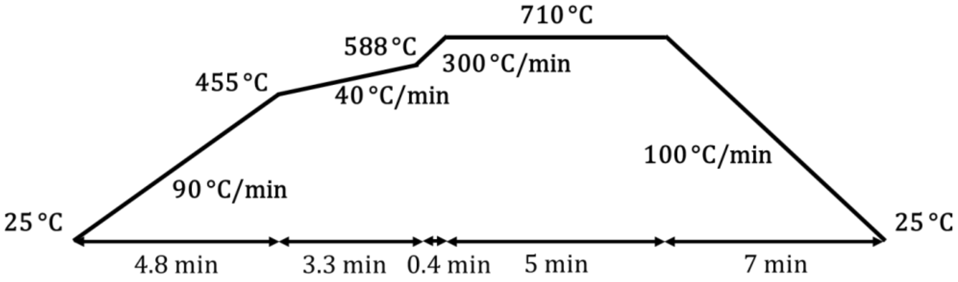

Figure 3.6: Temperature program for the barium titanate thin films in the RTP oven. The first step is heating from room temperature to 455 °C with a heating rate of 90 °C/min followed by slowly heating up to 588 °C with a heating rate of 40 °C/min. Then rapid heating up 710 °C with a heating rate of 300 °C/min. The temperature was held at 710 °C for 10 min before cooling to room temperature.

A 100 nm thick (10 layers) KNN film was deposited on top of the BT-ZnO film after plasma cleaning of the latter. The KNN layers were pyrolysed and annealed in an RTP oven, using the same temperature programs as for the ZnO thin films, with an atmosphere consisting of an 80/20 mixture of nitrogen and oxygen.

3.3 Deposition of electrodes, polymer layer and release process

After plasma cleaning of the KNN-BT-ZnO-SiPt substrate, a 100 nm thick platinum (Pt) bottom electrode was deposited on top of the KNN thin film, using an e-beam machine (AJA International Inc, Custom ATC-2200V), with a deposition rate of 5 Å/s. The surface was then plasma cleaned again before the deposition of a few drops of polydimethylsiloxane (PDMS) on top of the Pt bottom electrode. The viscous PDMS solution was spin coated at 500 rpm for 30 s, before curing at room temperature for seven days.

The PDMS covering the edges was removed with a scalpel before the sample stack (PDMS-Pt-KNN-BT-ZnO-SiPt) was immersed in the 33 % acetic acid, preheated to 60 °C. The ZnO-layer was etched away, and the PDMS-Pt-KNN-BT sample was released from the rigid silicon substrate. After the separation process, the flexible ceramic film was rinsed with distilled water and plasma cleaned before Pt top electrodes were deposited onto the flexible BT-KNN thin film using a shadow mask, illustrated in Figure 3.7. The diameter of the smallest top electrodes is 0.5 mm and the diameter of the larger ones is 1 mm.

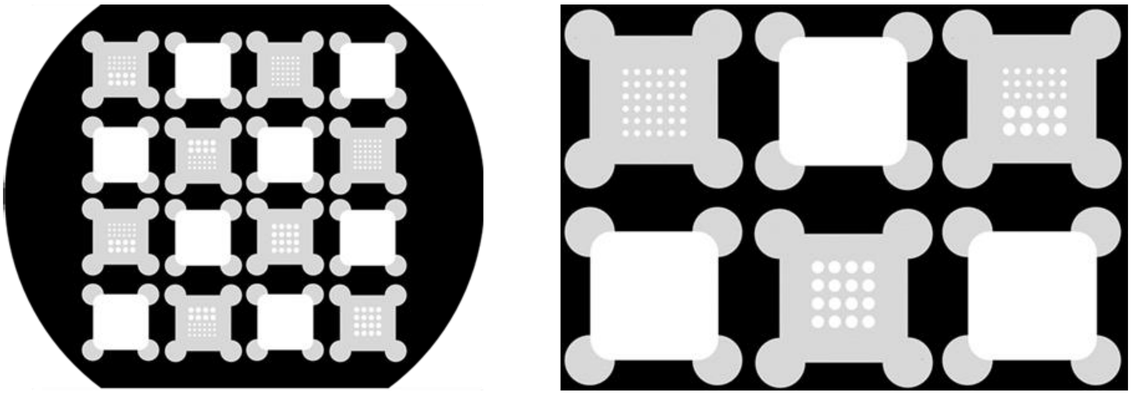

Figure 3.7: The shadow mask used for deposition of platinum top and bottom electrodes on thin films. The white square areas serve as the mask for the bottom electrodes and the patterned areas represent the mask for the top electrodes. To the right is a magnified illustration of the masks. The area of the smallest top electrodes is 0.5 mm and the area of the larger ones is 1 mm.

3.4 Characterisation

Ferroelectric measurements were performed in a TF Analyser 2000 with an aixACCT 200V high voltage amplifier from AixACCT Systems GmbH, Germany. To ensure contact with the platinum bottom electrode, a small area in the corner of the ceramic thin film was removed and covered with silver paint. To perform the measurement, one probe was placed on the silver paint and the other probe was placed on one of the top electrodes. Measurements from top electrode to top electrode were also conducted.

Grazing incidence X-ray diffraction (GI-XRD) was used to classify the crystallographic phases in the thin films. The film was mounted in a deep sample holder using modelling clay and scanned in an X-Ray Diffractometer (D8 A25 DaVinci) in grazing incidence mode. The total scan time was 2.5 h with the scanning detector angle (2θ) going from 20° to 80° and the incidence angle set to 2°.

A field emission scanning electron microscopy (SEM) with in-lens detector (Zeiss Ultra 559) was used to characterise the surface and the cross section of the thin films. The working distance was set to approximately 7 mm and the apparatus was set to 30 µm with an acceleration voltage of 10 mV.

Infrared (IR) spectra were recorded with a Bruker FTIR instrument (VERTEX 80v) and a Praying Mantis Diffuse Reflection cell (Harrick Scientific) from 400 to 4000 cm^{-1}. An aperture of 8 mm was used, and 32 scans were collected and averaged for each spectrum. A clean SiPt substrate was used as the background and a resolution of 4 cm^{-1} was used for all measurements.

4 Results

This section is divided into subsections based on the different steps in the extended synthesis route for preparing phase pure flexible oxide thin films for ferroelectric measurements, illustrated in Figure 3.1 (2a-2f) and Figure 4.1. In addition, the effect atmosphere, temperature and precursor solution had on the formation of KNN thin films was also investigated. These results are presented in Appendix C.2.

In the first section, the results from the characterisation of the ZnO thin film are presented. The next two sections contain the results from characterisation of the $BaTiO_3$ (BT) and the $K_{0.5}Na_{0.5}NbO_3$ (KNN) thin film respectively, followed by observations from the deposition of the platinum electrode and the PDMS layer. Finally, subsections concerning the release process and the ferroelectric measurements are presented.

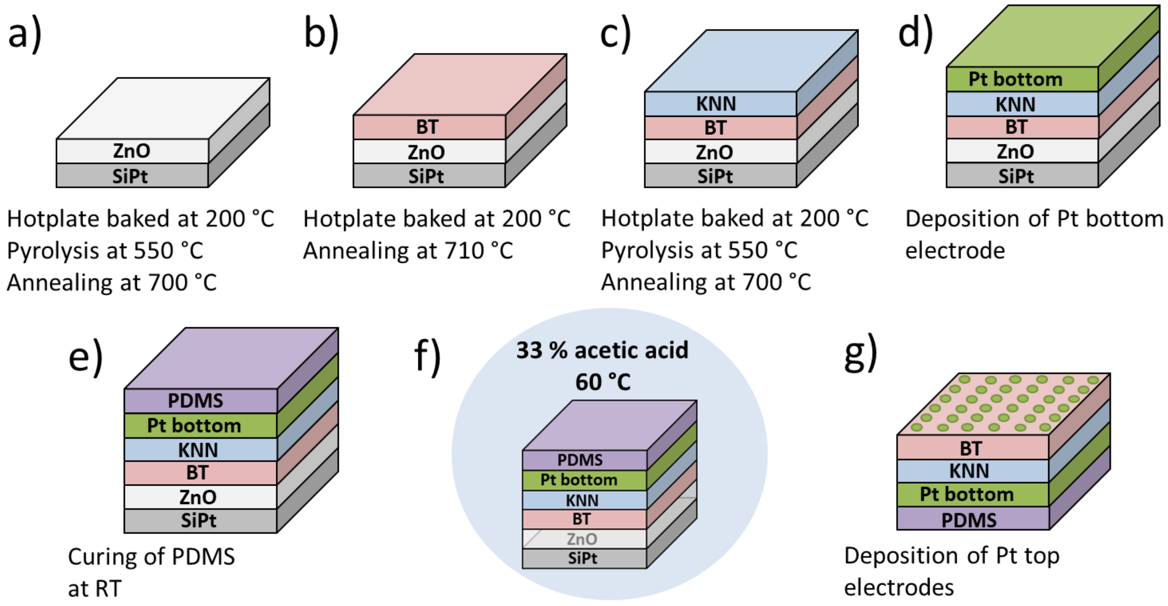

Figure 4.1: The extended synthesis route for preparing phase pure flexible oxide thin films for ferroelectric measurements. a) Deposition of zinc oxide (ZnO) as a release layer on a platinum coated silicon substrate. b) Deposition of barium titanate (BT) on top of the ZnO film. c) Deposition of potassium sodium niobate (KNN) on top of the BT film. d) Deposition of a platinum (Pt) bottom electrode on the KNN film. e) Deposition of polydimethylsiloxane (PDMS) on top of the Pt bottom electrode as the polymer support. f) The release process where the sample stack is immersed in 33 % acetic acid preheated to 60 °C. The ZnO layer is etched away, releasing the BT-KNN-Pt-PDMS sample. g) Deposition of the Pt top electrodes on the BT-KNN-Pt-PDMS sample stack.

4.1 Deposition of the zinc oxide

Spin coating provided homogeneous layers of zinc oxide (ZnO) solution on top of the platinum coated silicon (SiPt) substrate. This was also observed for the subsequent solution deposited on the pyrolysed ZnO layers. After deposition of 10 layers and annealing at 700 °C, the films appeared dense and homogeneous, and they had a light yellow colour with traces of red and white in the corners, displayed in Figure 4.2.

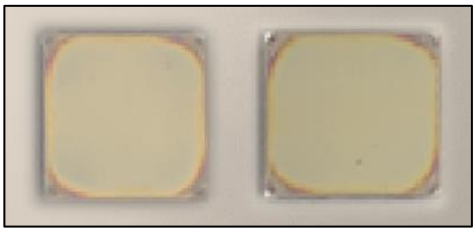

Figure 4.2: Image of ZnO thin films on SiPt substrates. After deposition of 10 layers of ZnO precursor solution, the result was uniform ZnO thin films. The colour is light-yellow in the centre of the films with traces of red and white on the edges.

Surface images of two ZnO thin films from two different batches obtained by SEM show a dense and homogeneous surface, as displayed in Figure 4.3. The first ZnO film, prepared with a 0.27 M ZnO precursor solution, has a more uniform surface and tightly packed grains compared to the second ZnO film, prepared from a 0.29 M solution, displayed in Figure 4.3 a) and b) respectively. Small pores were observed in the second ZnO film, indicated by white arrows in Figure 4.3 b). The grain size varied from ~49 nm to ~230 nm for the first ZnO thin film (Figure 4.3 a)), see Appendix A.1. The grain sizes of the second ZnO thin film were not measured.

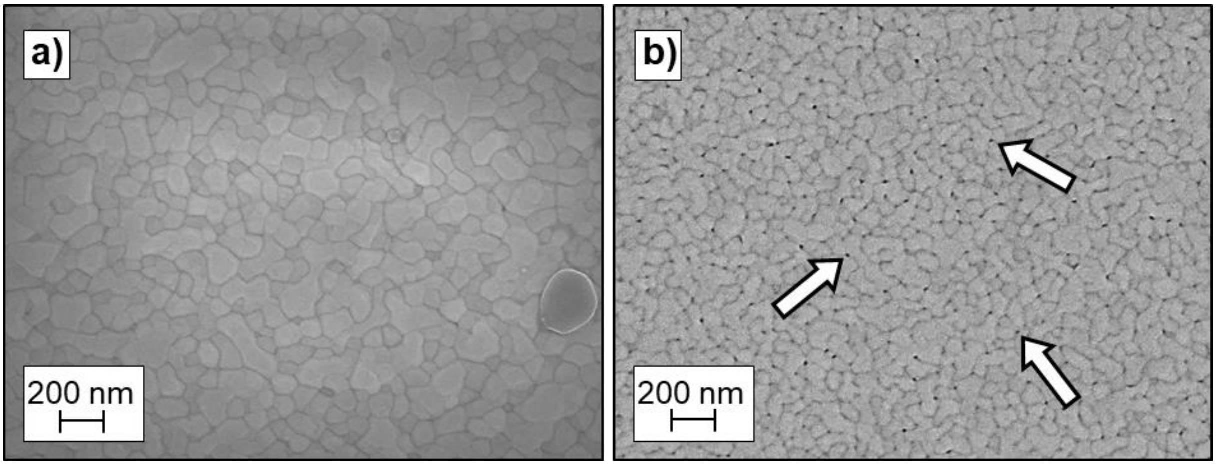

Figure 4.3: SEM images of the surface of two different ZnO thin films after annealing at 700 °C. a) A dense surface from the first ZnO film, prepared with a 0.27 M ZnO precursor solution. The grain size varied from ∼49 nm to ∼230 nm. b) A relatively dense surface from the centre of the second film, prepared with a 0.29 M ZnO precursor solution. Small pores were observed here indicated by the white arrows.

Cross-section images of the ZnO film from the 0.27 M precursor solution obtained by SEM shows an even film with a variety in film thickness from ~104 nm to ~145 nm, shown in Appendix A.1. Two different cross-section images of the sample are displayed in Figure 4.4, one a) without tilting and one b) that is tilted 5°. Both images of the samples display the silicon substrate at the bottom followed by the platinum layer, viewed as a white line, and the ZnO thin film on top.

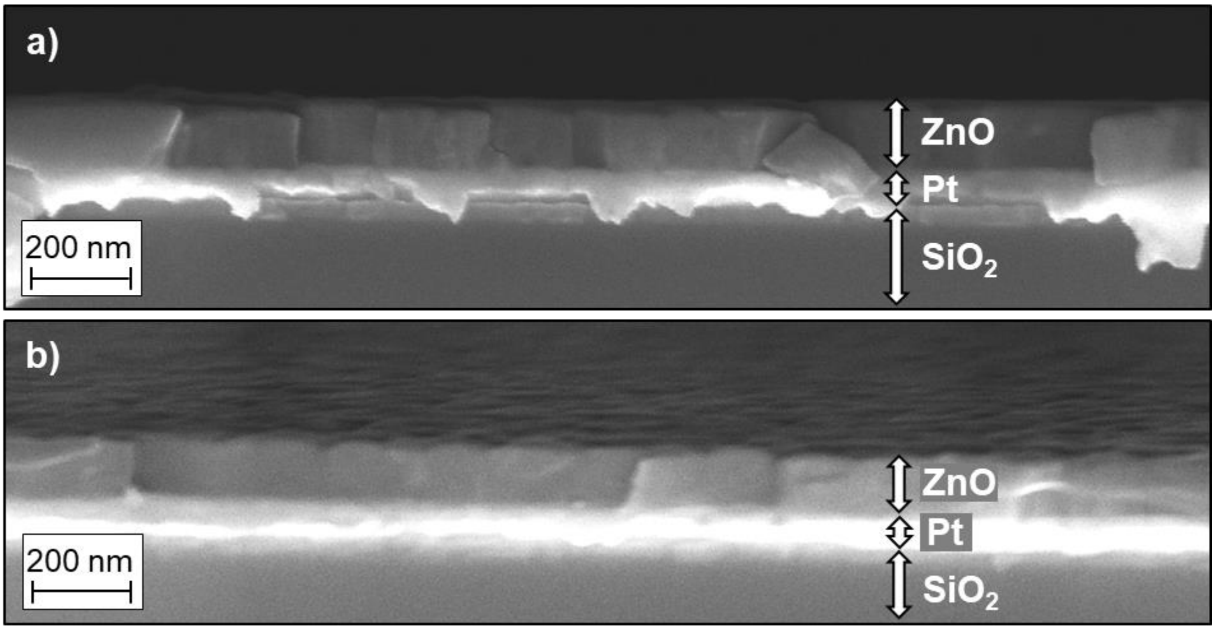

Figure 4.4: SEM images of the cross-section of the ZnO thin film from the 0.27 M precursor solution. a) The sample without tilting. b) The sample tilted 5°. The film is uniform, and the thickness varied from ~104 nm to ~145 nm. The silicon substrate is at the bottom of the image, followed by a white line that represents the platinum layer with the ZnO thin film on top.

The grazing incidence X-ray diffraction (GI-XRD) pattern of the ZnO thin film on the platinum coated silicon (SiPt) substrate is displayed in Figure 4.5, including the Miller indices for ZnO. All the Bragg reflections in the pattern can be assigned to the indexed diffraction lines of ZnO or pure SiPt. The Bragg reflection with the highest intensity is from the ZnO film from the (103)-lattice plane at 2θ = 63°.

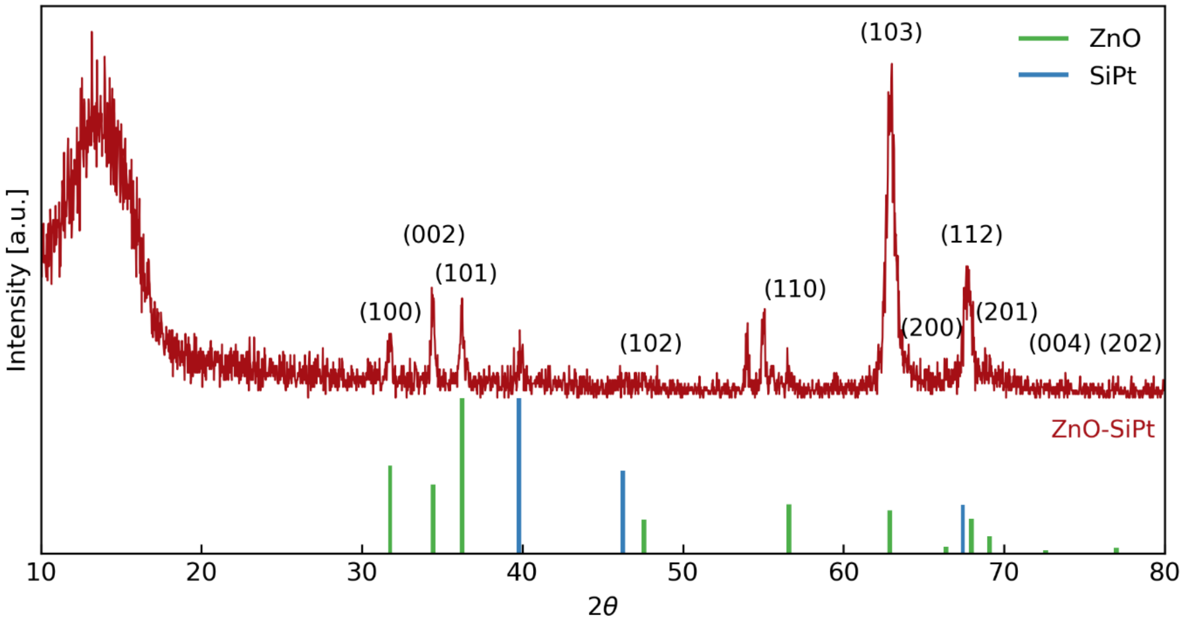

Figure 4.5: GI-XRD pattern of the ZnO thin film on a SiPt substrate with Miller indices for the ZnO lattice planes. The strongest reflection observed is from the (103) lattice plane at 2θ = 63°. All the Bragg reflections from the ZnO film can be assigned to the diffraction lines of ZnO (green lines, PDF card 01-070-8070 [74]) or SiPt (blue lines, PDF card 00-004-0802 [75]). Only the diffraction lines above 20 % for SiPt are included.

The grazing incidence X-ray diffraction (GI-XRD) pattern of the ZnO thin film on SiPt and the corresponding pattern for the pure SiPt substrate are displayed for comparison in Figure 4.6.

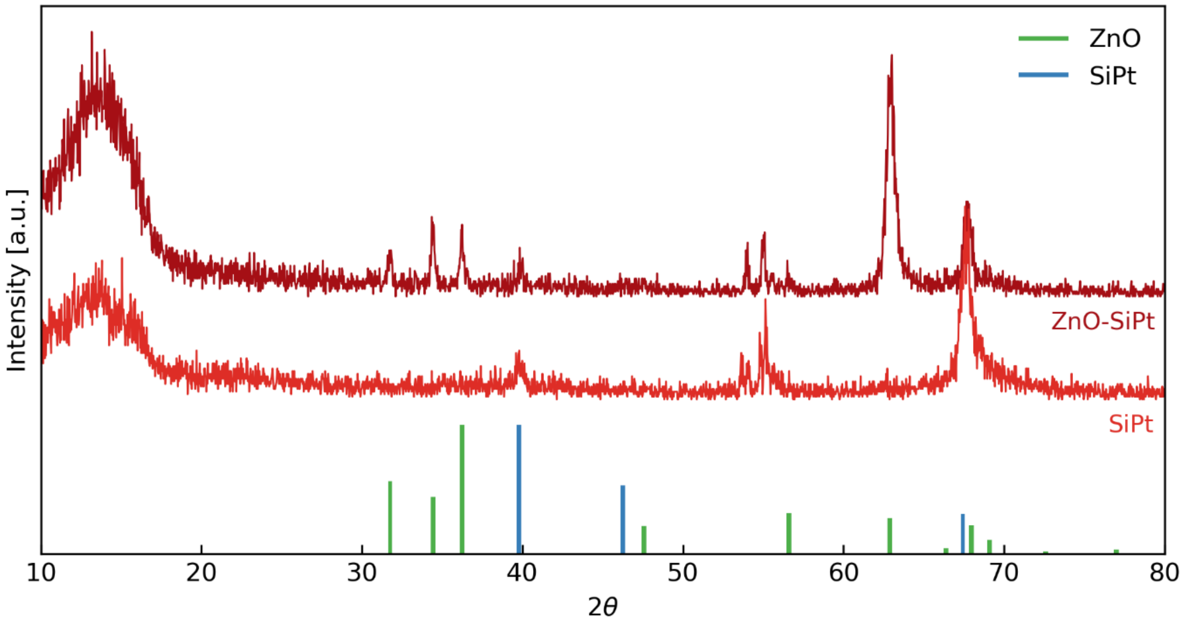

Figure 4.6: GI-XRD pattern of the zinc oxide (ZnO) thin film. The corresponding pattern for the pure SiPt substrate is included for comparison. All the Bragg reflections from the ZnO film can be assigned to the diffraction lines of ZnO (green lines, PDF card 01-070-8070 [74]) or SiPt (blue lines, PDF card 00-004-0802 [75]). Only the diffraction lines above 20 % for SiPt are included.

4.2 Deposition of barium titanate

Spin coating provided homogeneous layers of BT solution on top of the ZnO thin film. This was also observed for the solution deposited on top of the first BT layer. The films seem to be uniform and the centre of the films have a yellow colour with a purple colour on the edges and white in the corners, shown in Figure 4.7.

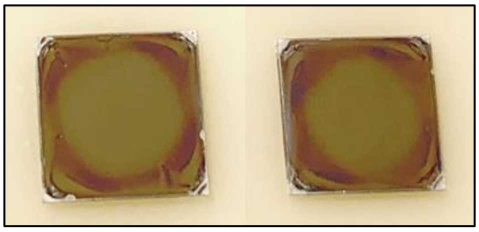

Figure 4.7: Image of samples after deposition of two layers of BT on the ZnO-SiPt samples. The centres of the films have a uniform, yellow colour and the colour on the edges shift between purple and yellow. The corners are white.

Characterisation of the surface of the BT thin film obtained by SEM shows a porous and rough surface, displayed in Figure 4.8 and Figure 4.9. The BT grains are clustered together, indicated with white arrows. Pits were observed between these clusters, indicated with black arrows.

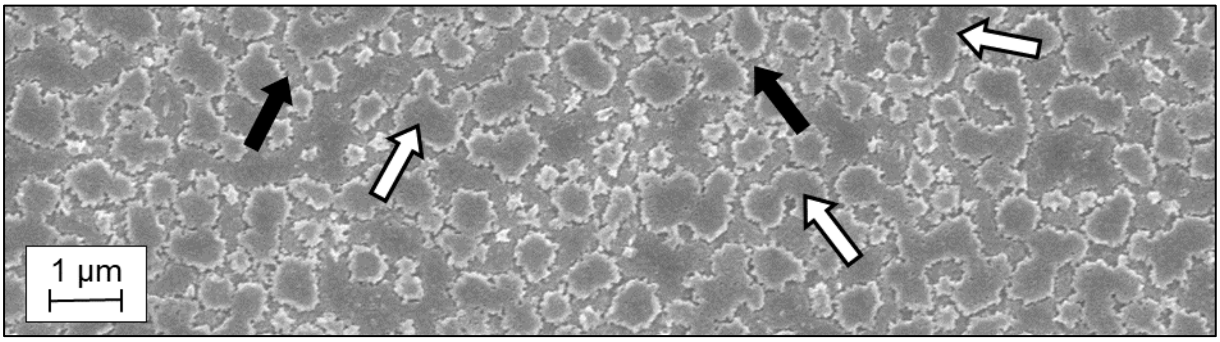

Figure 4.8: SEM image of the surface of the barium titanate (BT) thin film at a low magnitude. After deposition and annealing of two layers, the BT thin film looked porous and it seemed that the grains had clustered together, indicated with white arrows. Pits were observed between these clusters, indicated with black arrows.

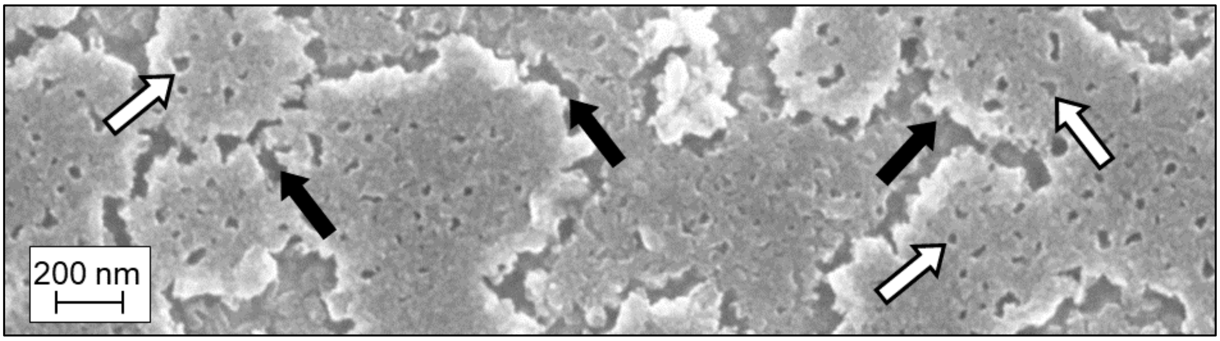

Figure 4.9: SEM image of the surface of the barium titanate (BT) thin film at a high magnitude. Small pores were observed in the clustered BT grains, indicated with white arrows. The pits observed in between the clusters are indicated with black arrows.

Analysis of the cross-section of the BT-ZnO-SiPt sample obtained by SEM indicated a rough BT layer on top of the ZnO thin film, displayed in Figure 4.10. The thickness of the film varied from ~25 nm to ~32 nm, shown in Appendix B.1. Two different cross-section images of the sample are displayed in Figure 4.10, a) one without tilting and b) one that is tilted 5°. Both images of the sample display the silicon substrate at the bottom, followed by the platinum layer, viewed as a white line. The ZnO thin film is on top of the platinum layer and finally the BT thin film on top of the ZnO film.

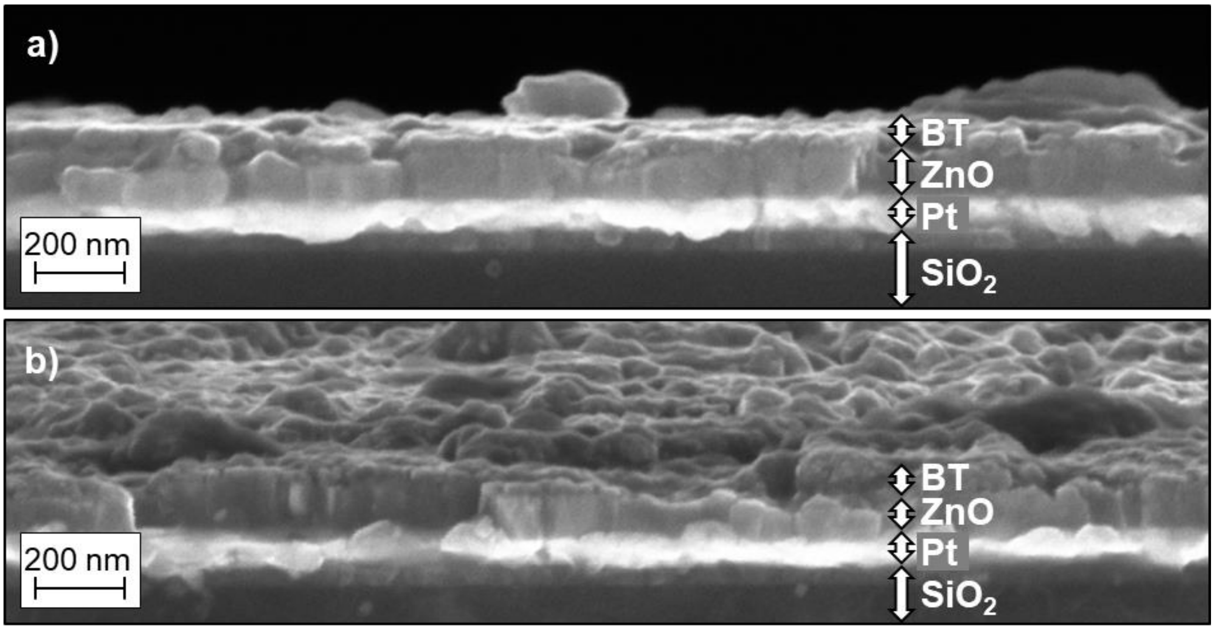

Figure 4.10: SEM images of the cross-section of the BT-ZnO-SiPt sample. a) The sample without tilting. b) The sample tilted 5°. The thickness of the film varied from ∼25 nm to ∼32 nm. The silicon substrate is at the bottom of the image, followed by a white line that represents the platinum layer. The ZnO thin film is on top of the platinum, followed by the BT thin film on top.

The GI-XRD pattern of the BT-ZnO-SiPt sample is displayed in Figure 4.11, including the Miller indices for $BaTiO_3$. The corresponding GI-XRD patterns for the ZnO thin film and the pure SiPt substrate are displayed for comparison in Figure 4.12. All the Bragg reflections from the BT-ZnO-SiPt sample can be assigned to the indexed diffraction lines of $BaTiO_3$, ZnO or SiPt. The strongest diffraction intensity for barium titanate is observed from the (110) lattice plane at $2\theta = 31.4°$. No secondary phases of BT were observed in the GI-XRD or the IR-spectra of BT (see Appendix B.2).

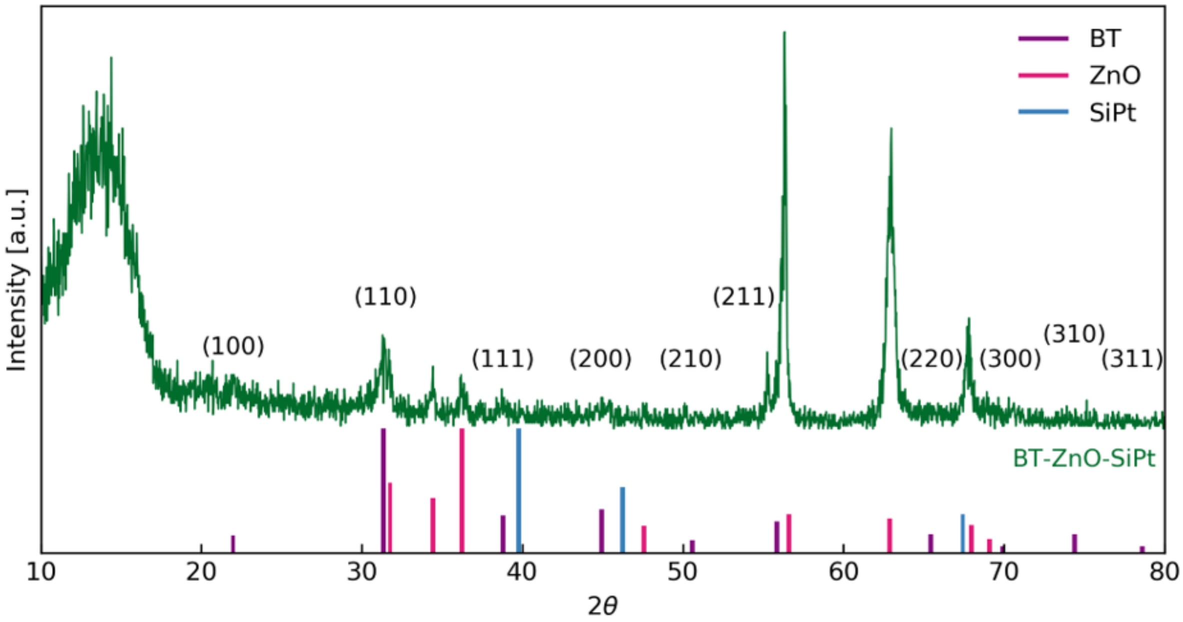

Figure 4.11: GI-XRD pattern of the BT-ZnO-SiPt sample with Miller indices for the BT lattice planes. The strongest diffraction intensity for BT is observed from the (110) lattice plane at 2θ = 31.4°. All the Bragg reflections from the BT-ZnO-SiPt sample can be assigned to the indexed diffraction lines for $BaTiO_3$ (purple lines, PDF card 00-031-0174 [76]), ZnO (pink lines, PDF card 01-070-8070 [74]) or SiPt (blue lines, PDF card 00-004-0802 [75]). Only the diffraction lines above 20 % for SiPt are included.

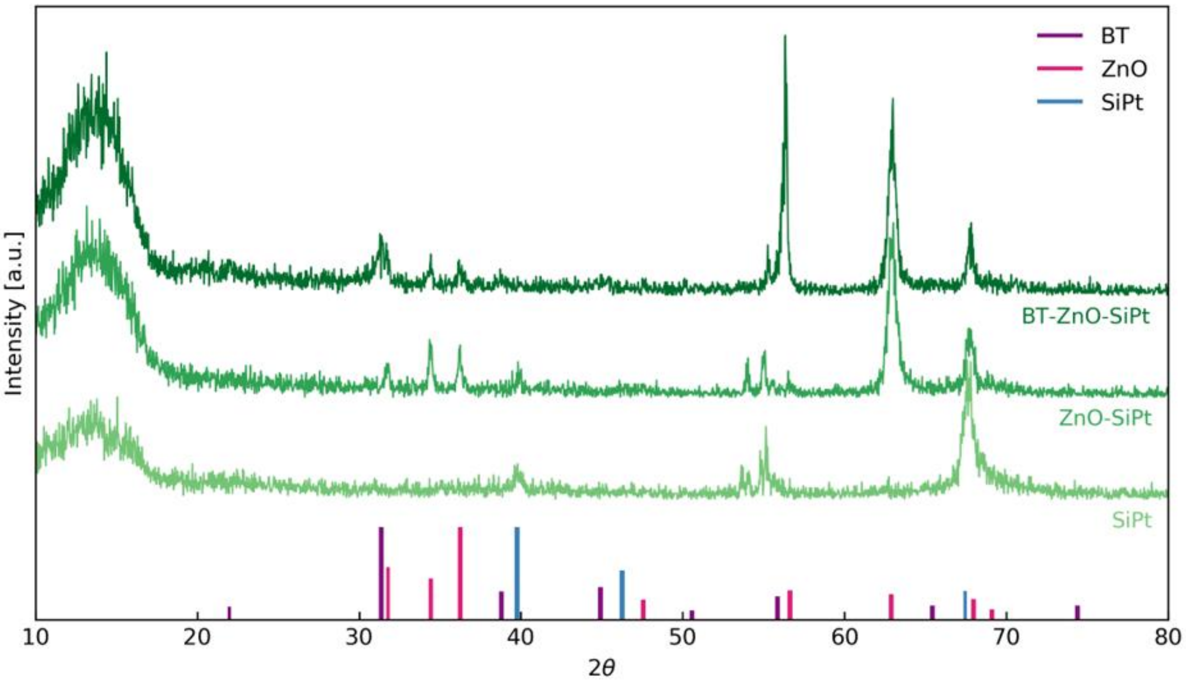

Figure 4.12: GI-XRD pattern of the BT-ZnO-SiPt sample. The corresponding patterns for the ZnO thin film and the pure SiPt substrate are also included for comparison. All the Bragg reflections from the BT-ZnO-SiPt sample can be assigned to the indexed diffraction lines of $BaTiO_3$ (purple lines, PDF card 00-031-0174 [76]), ZnO (pink lines, PDF card 01-070-8070 [74]) or SiPt (blue lines, PDF card 00-004-0802 [75]). Only the diffraction lines above 20 % for SiPt are included.

4.3 Deposition of potassium sodium niobate

Spin coating yielded homogeneous layers of KNN solution on top of the BT-ZnO-SiPt samples. This was also observed for the solution deposited on the pyrolysed KNN layers. The surfaces of the films appear to be uniform and depending on the angle of light reflection the centres of the films are yellow surrounded by a purple and a blue circle, with turquoise edges and white corners, illustrated in Figure 4.13.

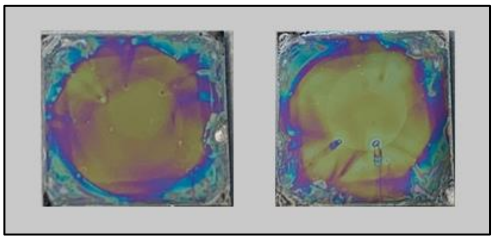

Figure 4.13: Image of the KNN thin films after deposition of 10 layers of KNN solution on the BT-ZnO-SiPt samples. The centres of the films are relatively uniform and have a yellow colour. The centres are surrounded by a purple and a blue circle with turquoise and white in the corners.

Surface images of the KNN thin film obtained by SEM show a dense and relatively uniform surface, displayed in Figure 4.14. The KNN grains appeared to be in the same size range and of the few grains measured, most of them varied from ~30 nm to ~90 nm in diameter, see Appendix C.1. A few larger grains were observed in between with diameters varying from ~180 nm to ~185 nm, indicated with white arrows.

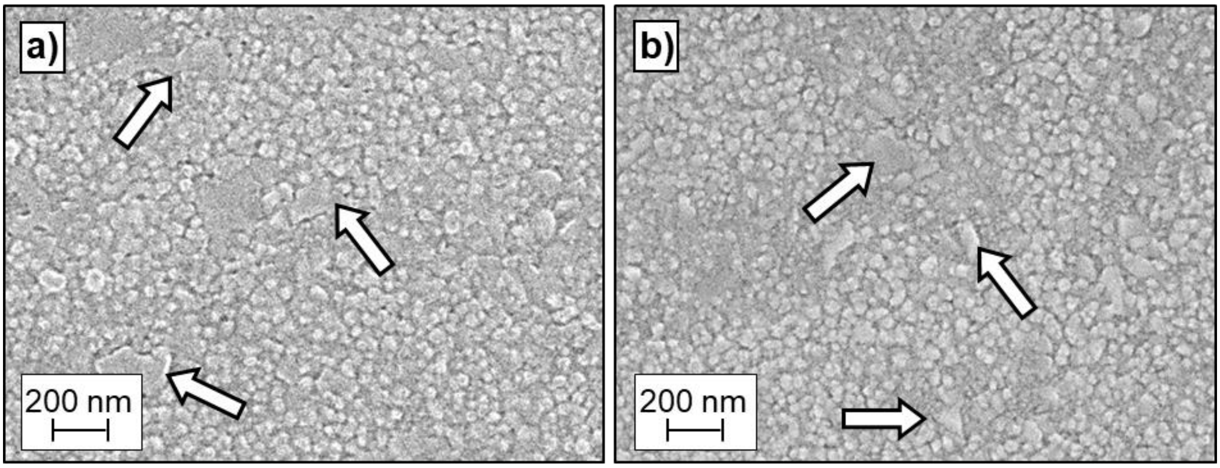

Figure 4.14: SEM images of the surface of the KNN thin film. a) The centre of the film and b) from the edge of the film. In both areas, there are a few larger grains observed, indicated by the white arrows. The diameter of the grains varied from ~30 nm to ~185 nm, see Appendix C.1.

Characterisation of the cross-section of the KNN-BT-ZnO-SiPt sample shows two separate films on top of the platinum coated silicon substrate. The KNN-BT thin film is located on top of the ZnO thin film, followed by the platinum layer (viewed as a white line) and the silicon substrate at the bottom. Two different cross-section images of the sample are displayed in Figure 4.15, a) one without tilting and b) one that is tilted 5°.

Measurements showed that the thickness of the KNN-BT layer varied from ~119 nm to ~124 nm, see Appendix C.1. A few voids were observed in the interface between the dense layers in the cross-section images in Figure 4.15. The surface of the KNN thin film appears to be uniform in the tilted sample (b).

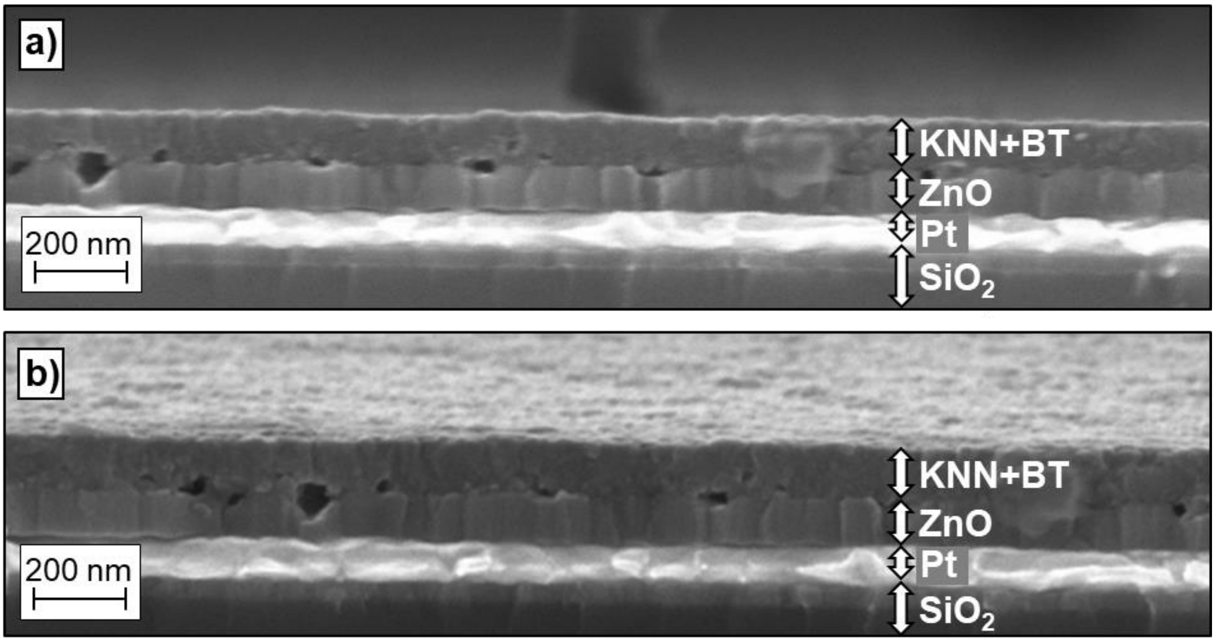

Figure 4.15: SEM images of the cross-section after deposition of 10 layers of KNN solution on top of the BT-ZnO-SiPt sample. a) The sample without tilting. b) The sample tilted 5°. The thickness of the film varied from ~119 nm to ~124 nm, see Appendix C.1. A few voids are observed in the interface between the ZnO layer and the KNN-BT thin film. The surface of the KNN layer is uniform. The silicon substrate is at the bottom of the image, followed by a white line that represents the platinum layer. The ZnO thin film is on top of the platinum layer, followed by the KNN-BT thin film on top.

The GI-XRD pattern of the KNN-BT-ZnO-SiPt sample including the Miller indices for $K_{0.5}Na_{0.5}NbO_3$ lattice planes is displayed in Figure 4.16. The corresponding GI-XRD patterns for the BT-ZnO thin film, the ZnO thin film and the SiPt substrate are included for comparison in Figure 4.17. All the new Bragg reflections from the KNN-BT-ZnO-SiPt sample can be assigned to the indexed diffraction lines of $K_{0.5}Na_{0.5}NbO_3$, $K_4Nb_6O_{17}$, $BaTiO_3$, ZnO or SiPt. The strongest diffraction intensity for KNN was observed from the (100) and the (101) lattice planes at $2\theta = 22°$.

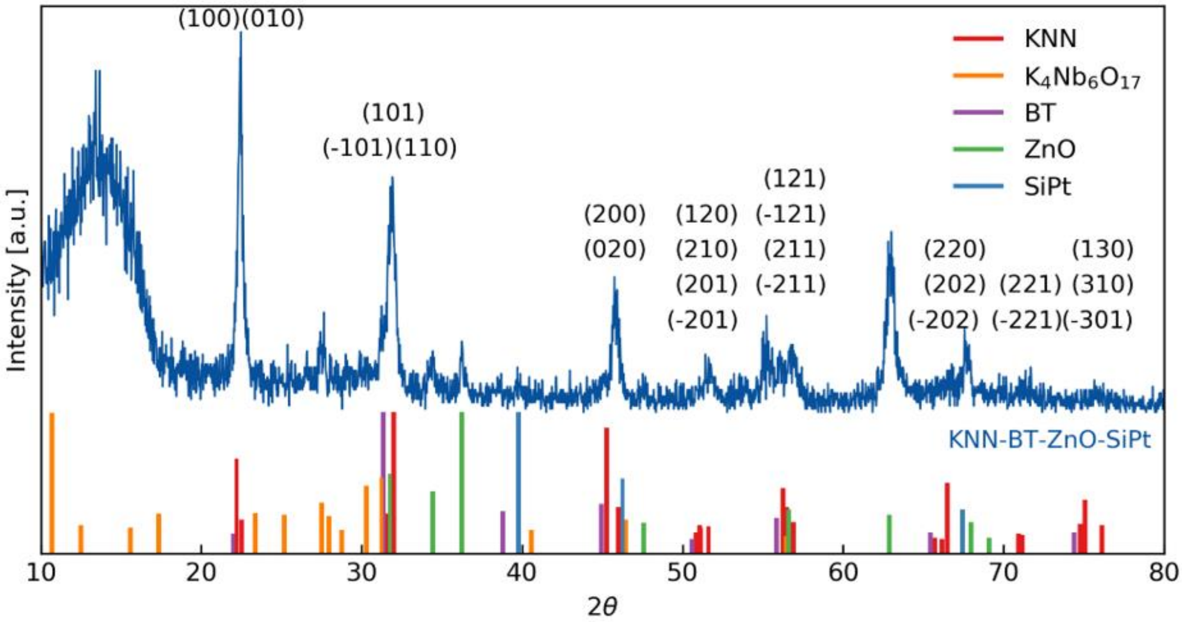

Figure 4.16: GI-XRD pattern of the KNN-BT-ZnO-SiPt sample. The Miller indices for the $K_{0.5}Na_{0.5}NbO_3$ lattice planes are displayed. All the Bragg reflections from the KNN film can be assigned to the indexed diffraction lines of $K_{0.5}Na_{0.5}NbO_3$ (red lines, PDF card 00-061-0315 [34]), $K_4Nb_6O_{17}$ (orange lines [77]), $BaTiO_3$ (purple lines, PDF card 00-031-0174 [76]), ZnO (green lines, PDF card 01-070-8070 [74]) or SiPt (blue lines, PDF card 00-004-0802 [75]). Only the diffraction lines above 20 % for $K_4Nb_6O_{17}$ and SiPt are included.

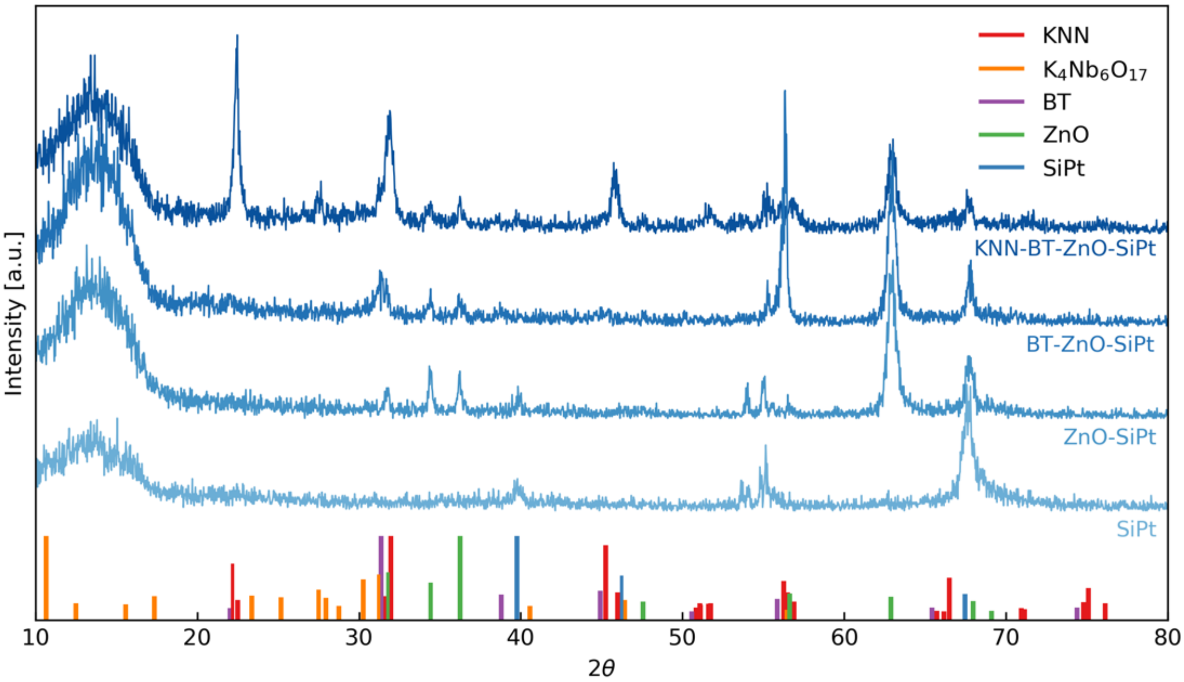

Figure 4.17: GI-XRD pattern of the KNN-BT-ZnO-SiPt sample. The corresponding patterns for the BT-ZnO-SiPt sample, the ZnO-SiPt sample and the pure SiPt substrate are included for comparison. All the Bragg reflections from the KNN film can be assigned to the indexed diffraction lines of $K_{0.5}Na_{0.5}NbO_3$ (red lines, PDF card 00-061-0315 [34]), $K_4Nb_6O_{17}$ (orange lines [77]), $BaTiO_3$ (purple lines, PDF card 00-031-0174 [76]), ZnO (green lines, PDF card 01-070-8070 [74]) or SiPt (blue lines, PDF card 00-004-0802 [75]). Only the diffraction lines above 20 % for $K_4Nb_6O_{17}$ and SiPt are included.

4.4 Deposition of platinum electrodes and PDMS

Uniform 100 nm thick platinum (Pt) bottom electrodes were deposited on top of the KNN-BT-ZnO-SiPt sample, displayed in Figure 4.18. The Pt covered the entire surface of the KNN thin film except for a small area in the corners of the samples.

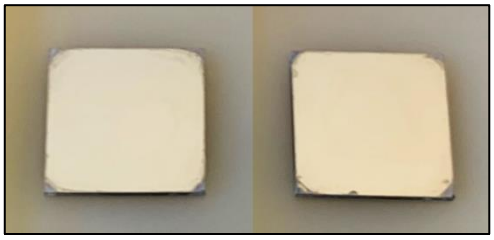

Figure 4.18: Image of the two samples after deposition of a 100 nm thick platinum bottom electrode on top of the KNN-BT-ZnO-SiPt sample. The entire surfaces are covered with platinum, except a small area in the corners of the sample.

Spin coating of the PDMS fluid resulted in a thick and curved layer of PDMS after curing for one week. The height of the PDMS layer was measured to be 0.89 mm with a calliper.

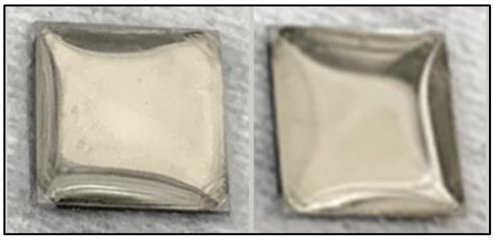

Figure 4.19: Image of two sample stacks consisting of PDMS-Pt-KNN-BT-ZnO-SiPt after one week of curing PDMS. No fractures are observed underneath the curved PDMS layer.

4.5 Release process of the flexible KNN thin film

The first separation process took approximately 2 h and the second 3 h. For both processes, the temperature was stabilised at 58 °C and the pH of the acetic acid solution was determined to be 2 before and after the separations. The ZnO layer was successfully etched away, separating the BT-KNN-Pt-PDMS sample from the SiPt substrate. The procedure is illustrated in Figure 4.20.

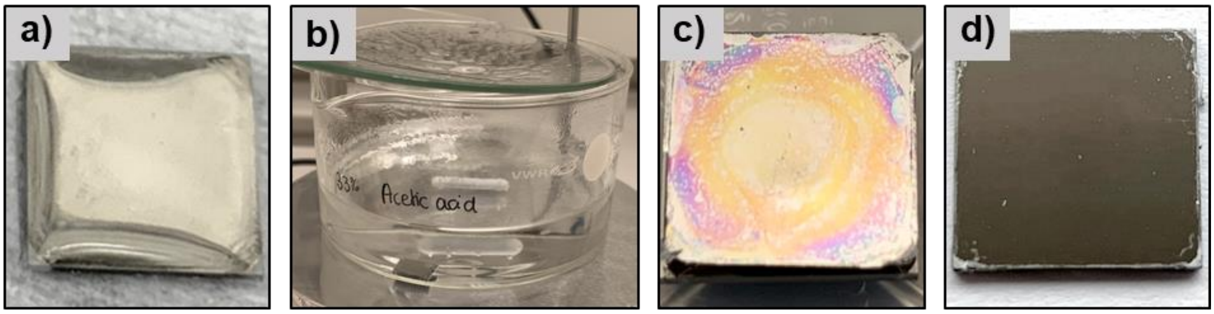

Figure 4.20: Illustration of the release process. a) The sample stack consisting of PDMS-Pt-KNN-BT-ZnO-SiPt. b) The sample stack immersed in 33 % acetic acid with continuous stirring at 58 °C. c) The released BT-KNN-Pt-PDMS sample. d) The empty SiPt substrate after the separation.

In the first separation process nearly all the BT-KNN-Pt, except for a few fragments in the centre of the film, was transferred onto the PDMS support, displayed Figure 4.21.

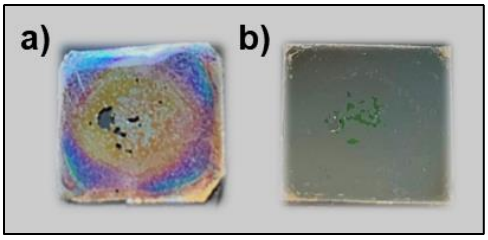

Figure 4.21: a) The first BT-KNN thin film with platinum bottom electrode on a PDMS support. b) The empty SiPt substrate after the release process. Most of the BT-KNN-Pt film was transferred onto the polymer support, except for a few fragments observed in the centre of the SiPt substrate.

Analysis of the surface images of the first released thin film obtained by SEM shows severe fractures and imprints across the entire surface, displayed in Figure 4.22 and Figure 4.23.

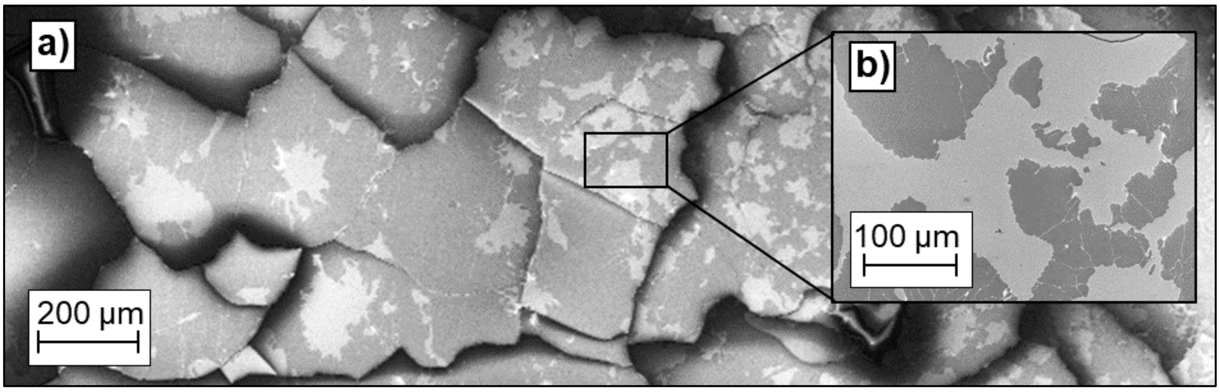

Figure 4.22: SEM image of the surface of the first released BT-KNN thin film on PDMS support with a platinum bottom electrode. a) The fractures across the ceramic thin film with imprints at low magnitude. b) Image of the imprints at high magnitude.

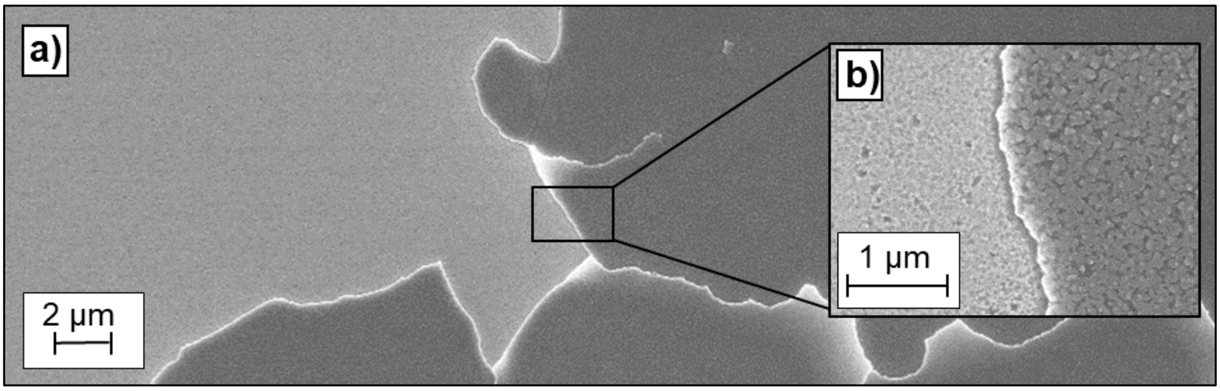

Figure 4.23: SEM image of the first released BT-KNN thin film on PDMS support with a platinum bottom electrode. a) SEM image of the boundaries between the imprints at low magnitude. b) SEM image of the boundary between the imprints at high magnitude.

The GI-XRD pattern of the first BT-KNN thin film on PDMS support with platinum bottom electrode is displayed in Figure 4.24. The corresponding GI-XRD patterns for the KNN-BT-

ZnO-SiPt sample, the BT-ZnO-SiPt sample and the ZnO-SiPt sample are displayed for comparison. All the new Bragg reflections from the flexible BT-KNN film can be assigned to the indexed diffraction lines of $K_{0.5}Na_{0.5}NbO_3$, $BaTiO_3$ or Pt. The strongest diffraction intensity from the sample was observed from the (111)-lattice plane for platinum at 2θ = 40°.

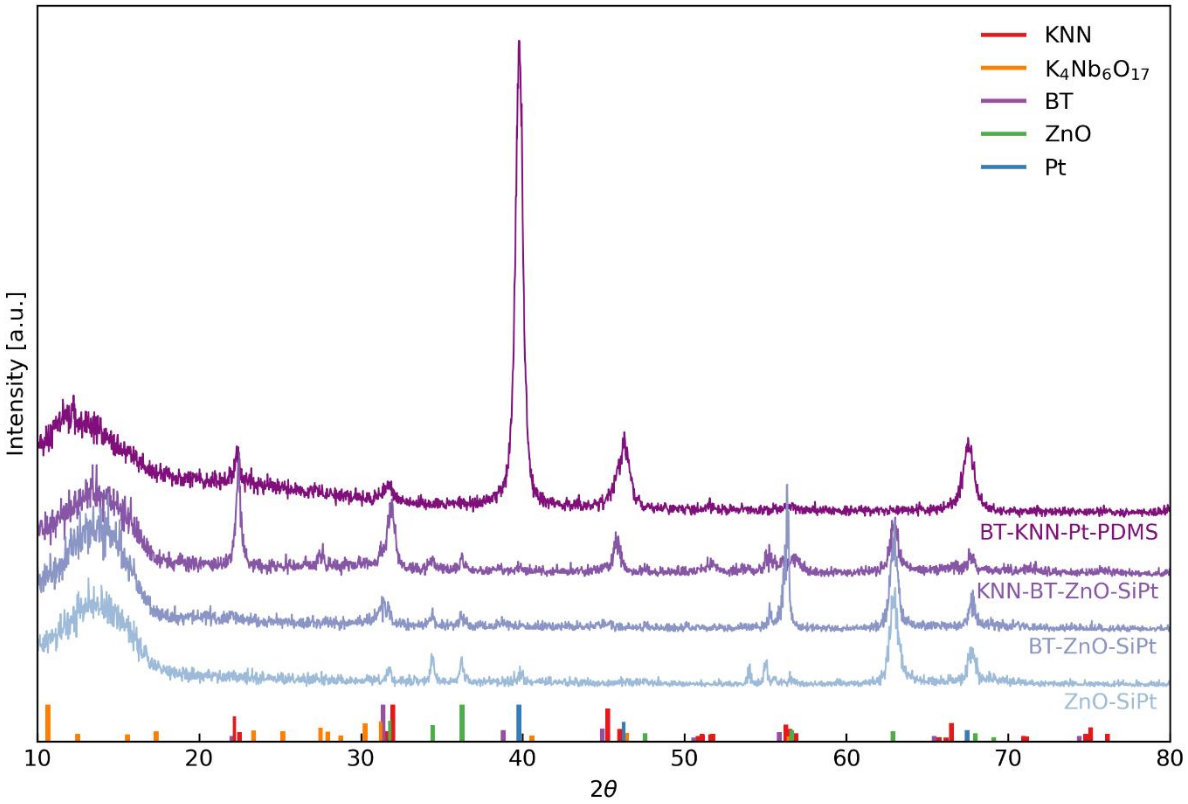

Figure 4.24: GI-XRD pattern of the first BT-KNN thin film on PDMS support with a platinum bottom electrode after the release process. The corresponding patterns for the KNN-BT-ZnO thin film, the BT-ZnO thin film and the ZnO thin film are also displayed for comparison. All the Bragg reflections from the BT-KNN film can be assigned to the diffraction lines of $K_{0.5}Na_{0.5}NbO_3$ (red lines, PDF card 00-061-0315 [34]), $BaTiO_3$ (purple lines, PDF card 00-031-0174 [76]) or Pt (blue lines, PDF card 00-004-0802 [78]). Only the diffraction lines above 20 % for $K_4Nb_6O_{17}$ and SiPt are included.

The GI-XRD pattern of the empty SiPt substrate after the first release process is displayed in Figure 4.25. The corresponding GI-XRD pattern for the pure SiPt substrate is included for comparison. All the Bragg reflections from the empty SiPt film, Figure 4.25, can be assigned to the indexed diffraction lines of for $K_{0.5}Na_{0.5}NbO_3$, $BaTiO_3$ and ZnO or SiPt.

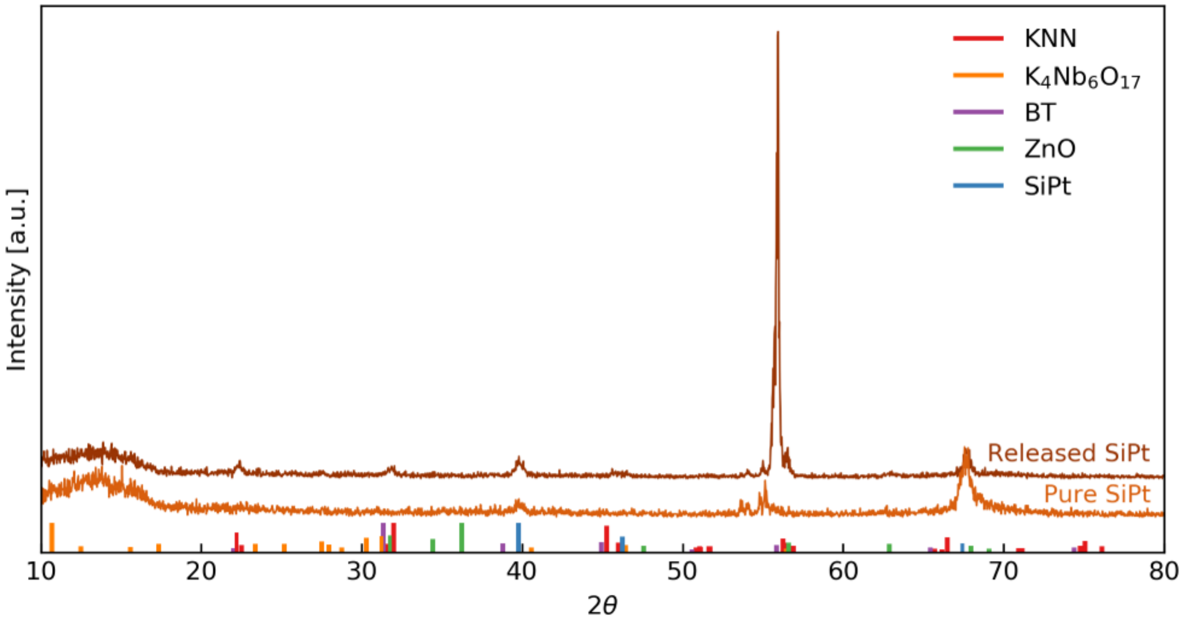

Figure 4.25: GI-XRD pattern of the empty SiPt after the first release process. The corresponding pattern for the pure SiPt substrate is also presented for comparison. All the Bragg reflections from the empty SiPt film can be assigned to the indexed diffraction lines of for $K_{0.5}Na_{0.5}NbO_3$ (red lines, PDF card 00-061-0315 [34]), $K_4Nb_6O_{17}$ (orange lines [77]), $BaTiO_3$ (purple lines, PDF card 00-031-0174 [76]) and ZnO (green lines, PDF card 01-070-8070 [74]) or SiPt (blue lines, PDF card 00-004-0802 [75]). Only the diffraction lines above 20 % for $K_4Nb_6O_{17}$ and SiPt are included.

In the second release process, all of the BT-KNN-Pt sample was successfully transferred onto the PDMS support, displayed in Figure 4.26. Platinum top electrodes were deposited directly after separation without GI-XRD characterisation of the flexible thin film.

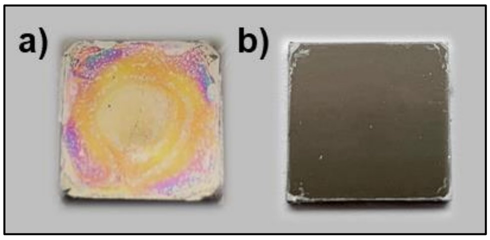

Figure 4.26: a) The second BT-KNN thin film on a PDMS support with a platinum bottom electrode. The thin film appeared to be intact. b) The empty SiPt substrate after the release process. No residues were observed, except for some in the corner of the substrate.

The GI-XRD pattern of the empty SiPt substrate after the second release process is displayed in Figure 4.27. The corresponding GI-XRD pattern for the pure SiPt substrate is included for comparison. All the Bragg reflections from the empty SiPt film can be assigned to the indexed diffraction lines for SiPt.

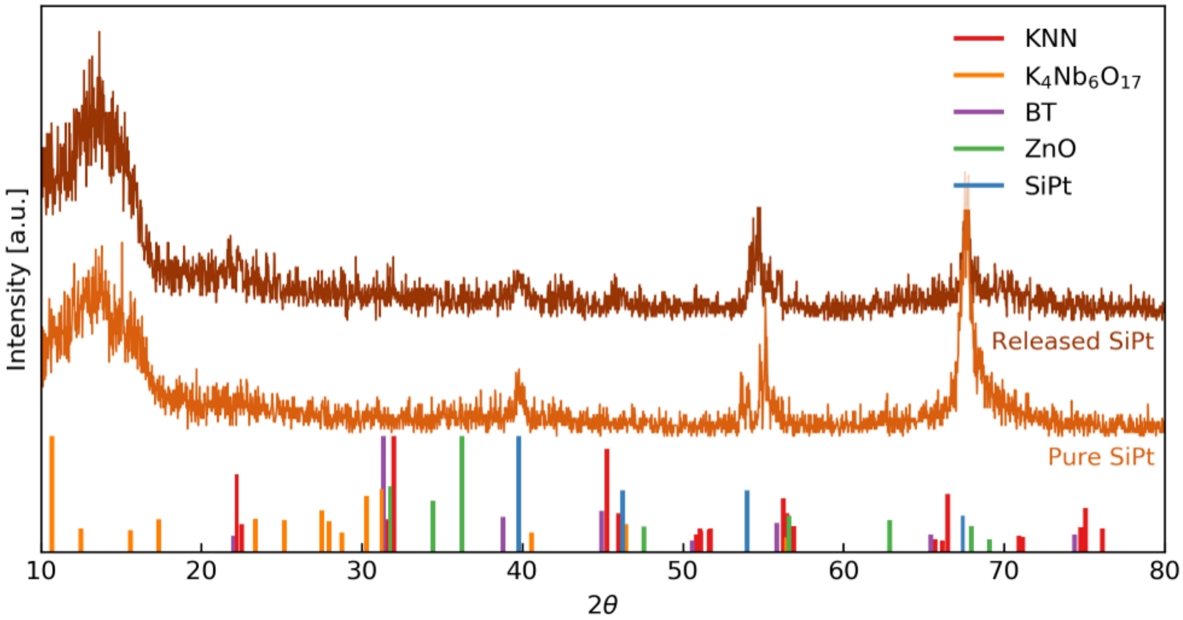

Figure 4.27: GI-XRD pattern of the empty SiPt after the second release process. The corresponding pattern for the pure SiPt substrate is included for comparison. All the Bragg reflections from the empty SiPt film can be assigned to the indexed diffraction lines of SiPt (blue lines, PDF card 00-004-0802 [75]). Only the diffraction lines above 20 % for $K_4Nb_6O_{17}$ and SiPt are included.

Images of the flexible KNN thin film after deposition of 100 nm thick platinum top electrodes are displayed in Figure 4.28. In total, 36 circular electrodes, each with an area of 0.1963 mm^2, were deposited on the ceramic film.

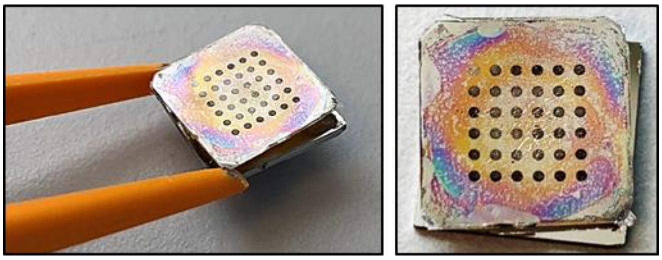

Figure 4.28: Image of the flexible BT-KNN thin film after deposition of 36 small platinum top electrodes with an area of 0.1963 mm^2 each. The flexible thin film is taped to a silicon substrate for mechanical support.

Cross-section images of the flexible BT-KNN-Pt-PDMS sample obtained by SEM show a dense BT-KNN thin film on top of a platinum layer, displayed in Figure 4.29. A freestanding thin film without any PDMS support is displayed in Figure 4.30.

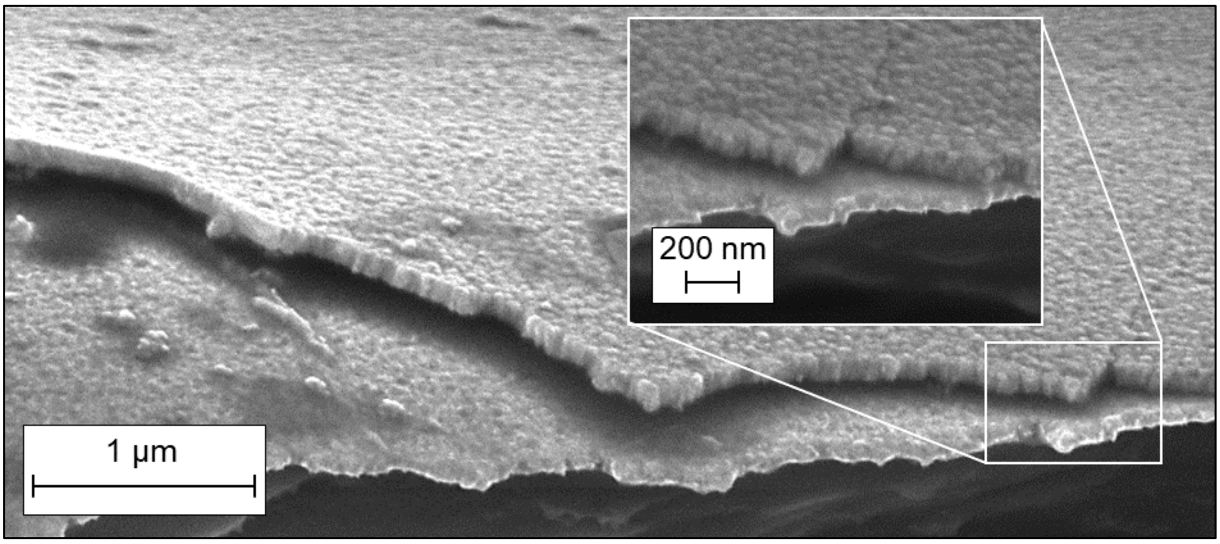

Figure 4.29: SEM image of the cross-section of the flexible BT-KNN thin film on PDMS support with platinum top and bottom electrodes. Two separate layers are observed on top of the PDMS layer; the BT-KNN film and the platinum bottom electrode.

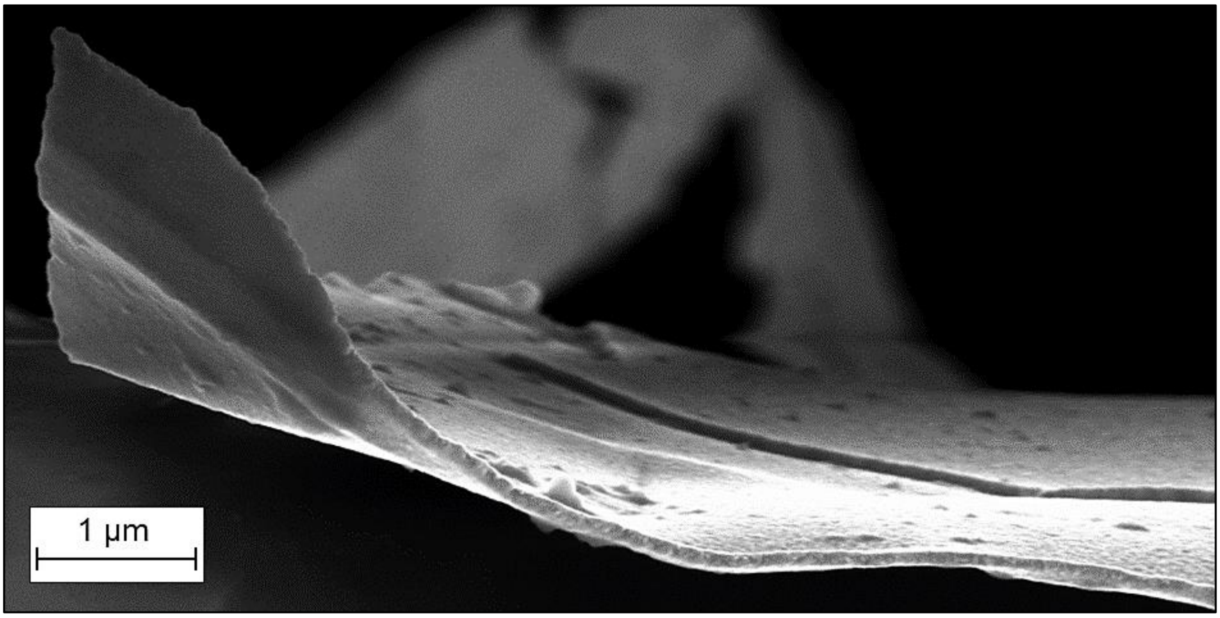

Figure 4.30: SEM image of a freestanding area of the BT-KNN thin film with platinum top and bottom electrodes.

4.6 Ferroelectric measurements

The measured hysteresis curve of polarisation (*P*) vs. electric field (*E*) at 1 kHz frequency of the flexible KNN thin film on PDMS support, illustrated in Figure 4.31. The shape indicates a high leakage current in the sample.

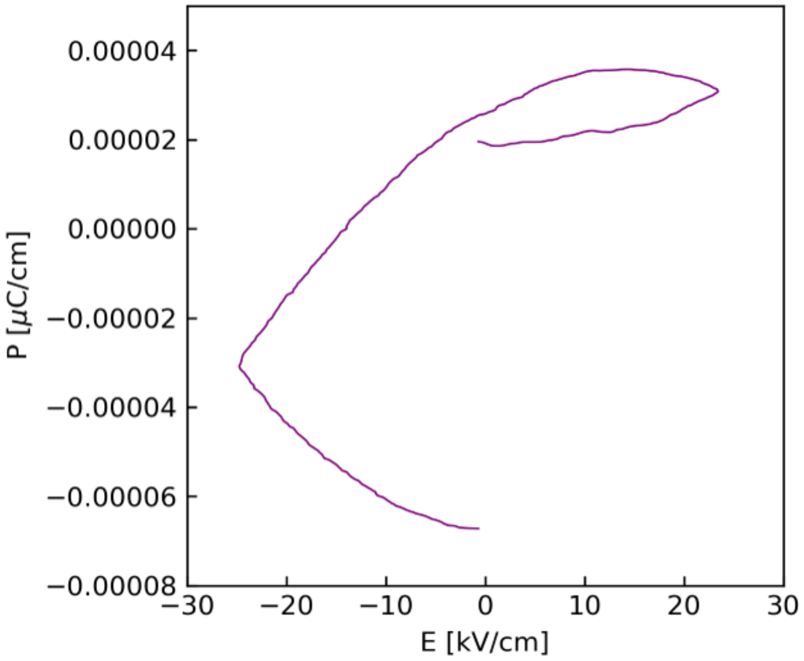

Figure 4.31: The measured hysteresis curve of polarisation (*P*) vs. electric field (*E*) at 1 kHz frequency of the flexible KNN thin film on PDMS support. The shape indicates a high leakage current in the sample.

5 Discussion

This project aimed to prepare flexible, phase pure KNN thin films that can be used in biomedical applications. The first part of this section concerns the phase purity of the ZnO, BT, KNN and released KNN thin film. The surface morphology is conferred in the next section. The third section reviews the release process, and in the final section, the ferroelectric performance is discussed.

5.1 Phase purity

In the GI-XRD patterns for the ZnO, BT and the KNN thin film, it was expected to see the reflections from the other layers and the SiPt substrate as the films are only ~100 nm thick.

The diffraction intensities detected for ZnO confirms that the thin film is phase pure. The Bragg reflections indicate that the crystal structure presumably is wurtzite. The strongest diffraction intensity was expected from the (101)-lattice plane at $2\theta = 36.2^\circ$ according to the table in Figure 5.1, indicated with a red arrow and red circles. However, the ZnO film showed strong diffraction intensities from the (103)-lattice plane at $2\theta = 63^\circ$ and the (112)-lattice plane at $2\theta = 68^\circ$, indicated with blue arrows and circles. This reflection implies that most of the crystals are oriented in the (103)-direction. The textured wurtzite structure of ZnO observed ((103)-texturing) is most likely an effect of the SiPt substrate. Kim et al. [79] reported ZnO thin films grown on Pt(111)-TiO_2-SiO_2-Si (SiPt) substrates exhibiting only the wurtzite structure. Exactly what the preferred orientation for the ZnO crystals are and if a SiPt substrate can be used to modify the orientation, as accomplished for PZT crystals [57], needs further investigation. An illustration of the wurtzite structure, including the (103)-lattice plane, is displayed in Figure 5.2.

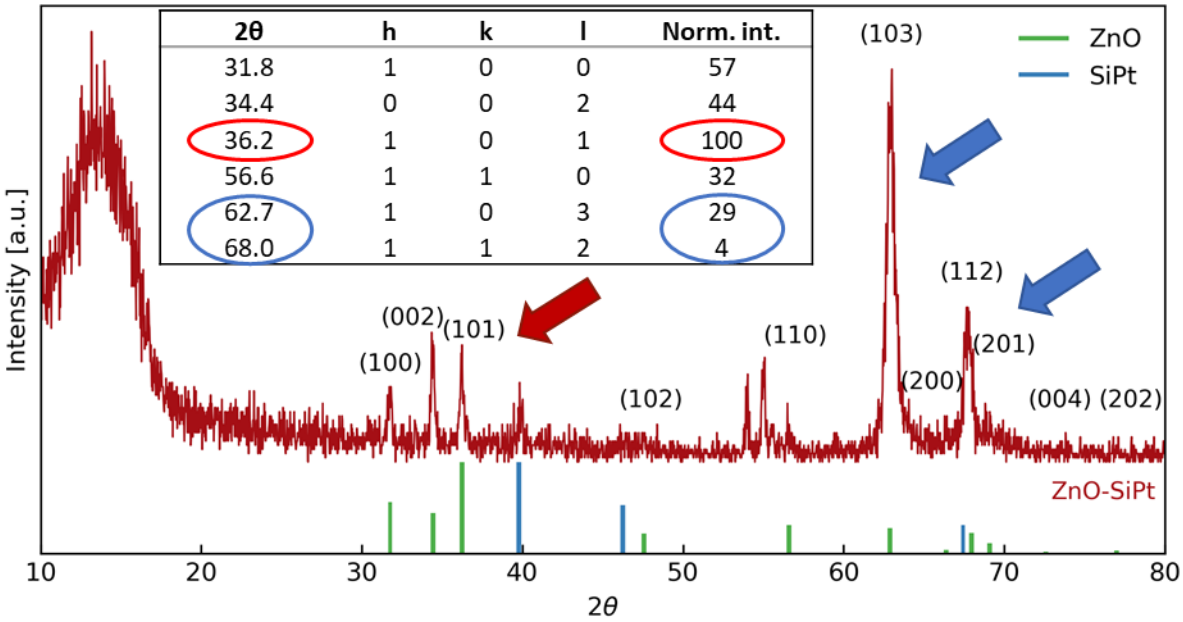

2θ	h	k	l	Norm. int.
31.8	1	0	0	57
34.4	0	0	2	44
36.2	1	0	1	100
56.6	1	1	0	32
62.7	1	0	3	29
68.0	1	1	2	4

Figure 5.1: GI-XRD pattern of the ZnO thin film, including a table with the normalised intensities and Miller indices for ZnO. The green lines are indexed peak positions for ZnO from PDF card 01-070-8070 [74] and the blue lines are indexed peak positions for SiPt from PDF card 00-004-0802 [75]. Only the strongest intensities for ZnO are included in the table.

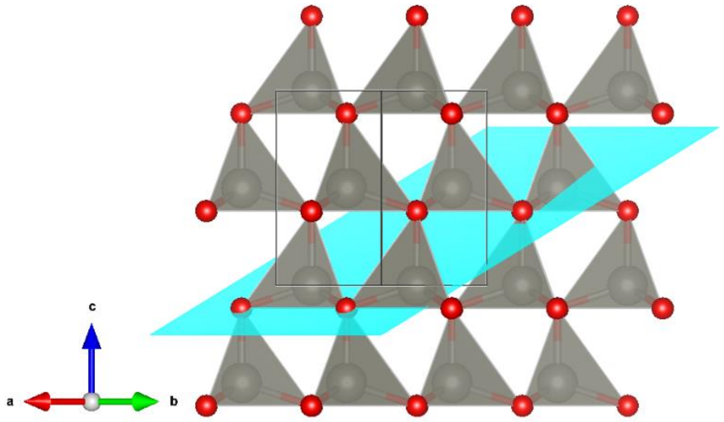

Figure 5.2: The wurtzite structure of ZnO, including the (103)-lattice plane (blue). The unit cell is presented with the black lines. The structure is created with the VESTA software [30].

The formation of the wurtzite structure of ZnO was observed after pyrolysing the ZnO thin film at 550 °C (Figure 5.3). The strong diffraction intensity from the (103) lattice plane at 2θ = 63° was observed in both samples, indicating that the ZnO thin film was oriented in the (103)-direction already at 550 °C. The difference in intensity between the pyrolysed and the annealed ZnO film is probably caused by different aligning of the samples, as stronger intensity was expected from the annealed film and not the pyrolysed film. The strong reflection observed at 2θ = 57° is assigned to the SiPt substrate, indicated with a blue arrow.

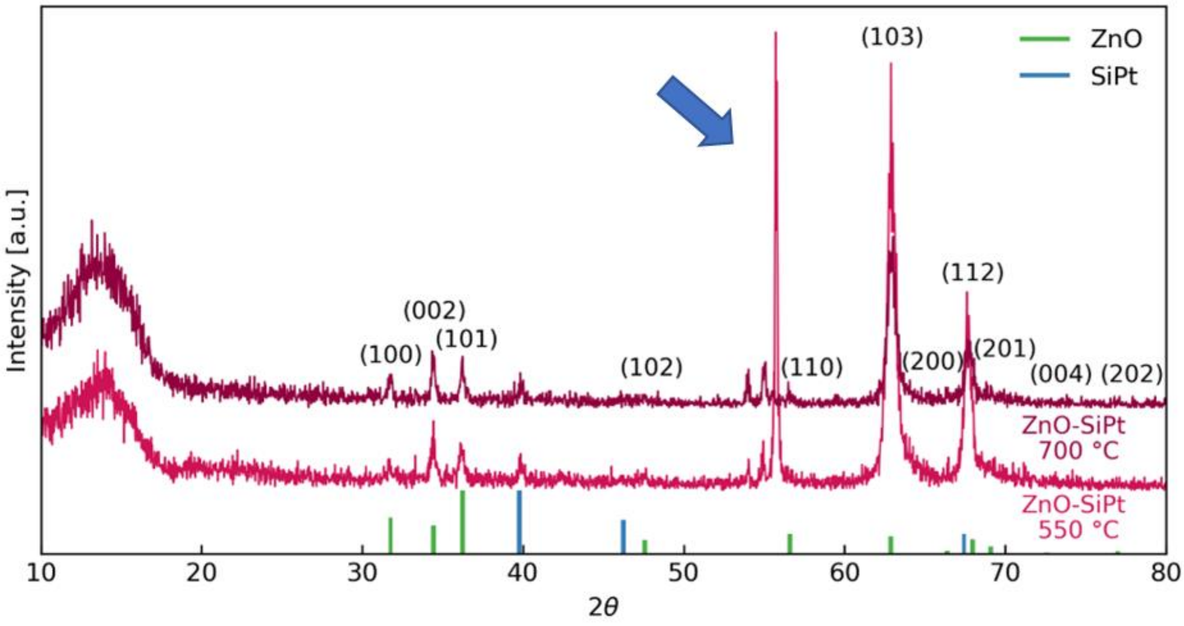

Figure 5.3: GI XRD patterns of the ZnO thin film heat-treated at 550 °C and 700 °C. The strong reflection observed at 2θ = 57° is assigned to the SiPt substrate, indicated with a blue arrow.

The GI-XRD pattern detected for the BT thin film did not contain any reflections from secondary phases of barium (e.g., Ti-rich phases and oxycarbonates like $BaCO_3$), proving that the film was phase pure. The strongest reflection was observed from the (100)-lattice plane at $2\theta = 31.7°$, marked with a blue arrow. The observation is consistent with the data presented in the table in Figure 5.4. The strongest reflection was observed at $2\theta = 56°$, marked by a red arrow, and is most likely from the substrate as seen in the 550 °C ZnO film (Figure 5.3).

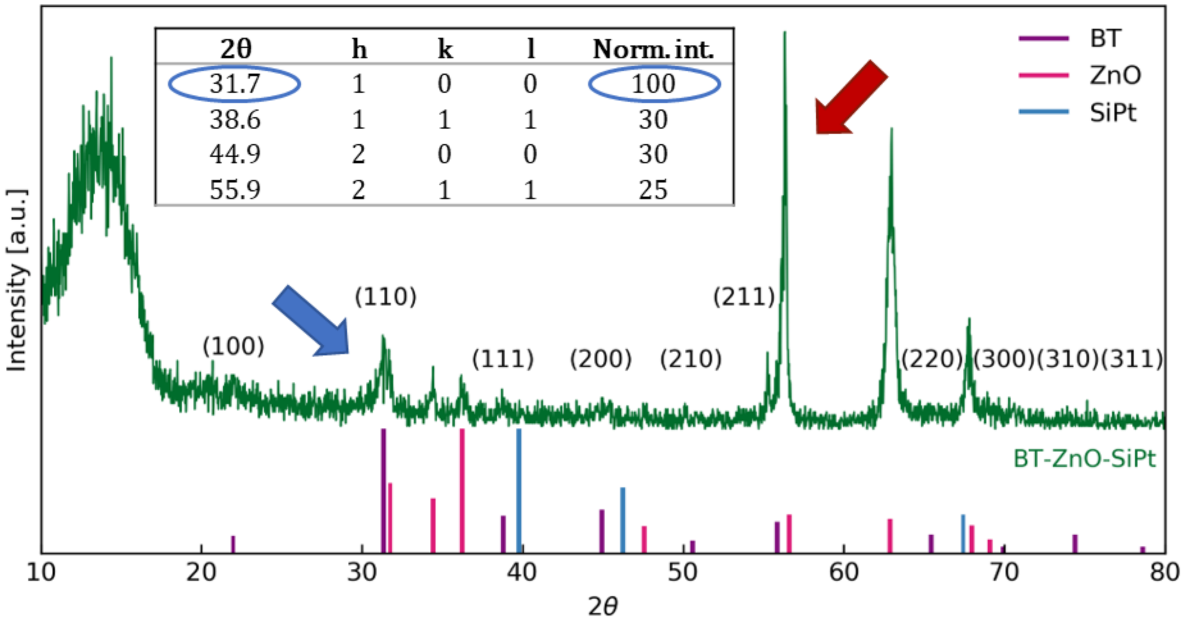

2θ	h	k	l	Norm. int.
31.7	1	0	0	100
38.6	1	1	1	30
44.9	2	0	0	30
55.9	2	1	1	25

Figure 5.4: GI-XRD pattern of the BT-ZnO-SiPt thin film, including a table with the normalised intensities for BT. The strongest intensity was expected from the (100)-plane at $2\theta = 31.7°$, indicated by the blue arrow. The strongest intensity was observed at $2\theta = 56°$ and is most likely from the substrate, indicated by the red arrow.

The infrared (IR) reflection spectra of the BT-ZnO-SiPt sample (Figure 5.5) did not detect any presence of oxycarbonates in the thin film. Oxycarbonates are common, metastable secondary phases in BT that are normally observed around 1400 cm^{-1} in IR spectra for BT powders [71, 80]. As the oxycarbonates are thermodynamically unstable, they were expected to vanish when the thin film was annealed at 710 °C [81]. Vibrational modes from the ZnO layer was observed around 570 cm^{-1} and was distinct in both samples, probably because the BT layer was very thin compared to the ZnO layer. The presence of $BaTiO_3$ was observed around 450 cm^{-1} and 710 cm^{-1}, indicated with red arrows in Figure 5.5. The result is comparable to what Raeder et al. [71] reported for $BaTiO_3$. The small difference in wavenumber might be explained by different incidence angles during the IR measurement. As no bands were observed above 900 cm^{-1} in the IR spectra and no reflections for secondary phases were detected in the GI-XRD patterns, it is safe to assume the BT film was phase pure.

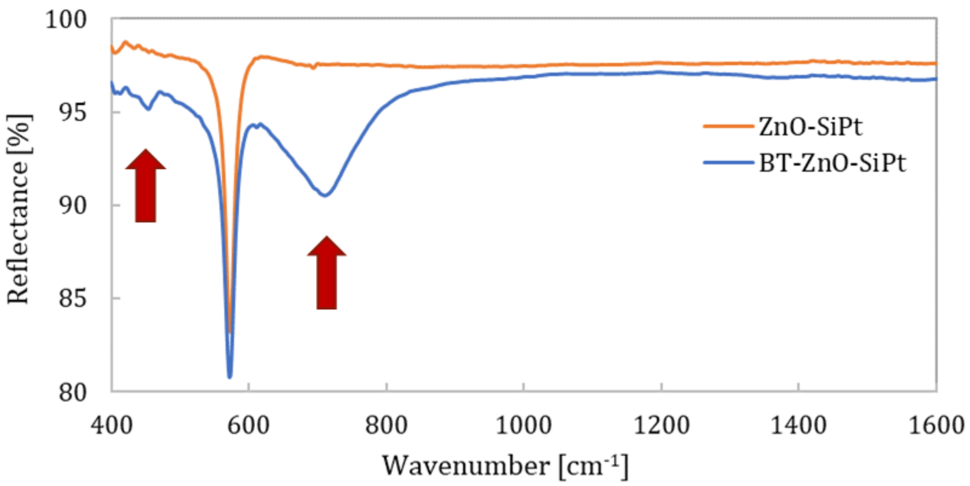

Figure 5.5: The infrared (IR) reflectance spectra of the BT-ZnO-SiPt sample. The IR spectra for ZnO-SiPt is included for comparison. $BaTiO_3$ is observed around 450 cm^{-1} and 710 cm^{-1}, indicated with red arrows. The ZnO layer is observed around 570 cm^{-1}, and the oxycarbonate phases, normally observed around 1400 cm^{-1} were absent in the spectra.

The GI-XRD pattern showed that the KNN thin film was relatively phase pure. The strongest reflection for KNN was observed from the (100)- and the (010)-lattice planes around 2θ = 22° (blue arrow and circles in Figure 5.6), however, it was expected to come from the (110)-lattice plane at 2θ = 31.8° (green arrow and circles), indicating that the KNN film was somewhat textured. The peak observed at 2θ = 27° can be assigned to $K_4Nb_6O_{17}$, indicated with a red circle in Figure 5.6. However, the strongest reflection for this secondary phase was expected at 2θ = 10.7°, but this peak was absent, indicated with a red arrow. Therefore, the reflection observed at 2θ = 27° is most likely from an unidentified phase and not from $K_4Nb_6O_{17}$.

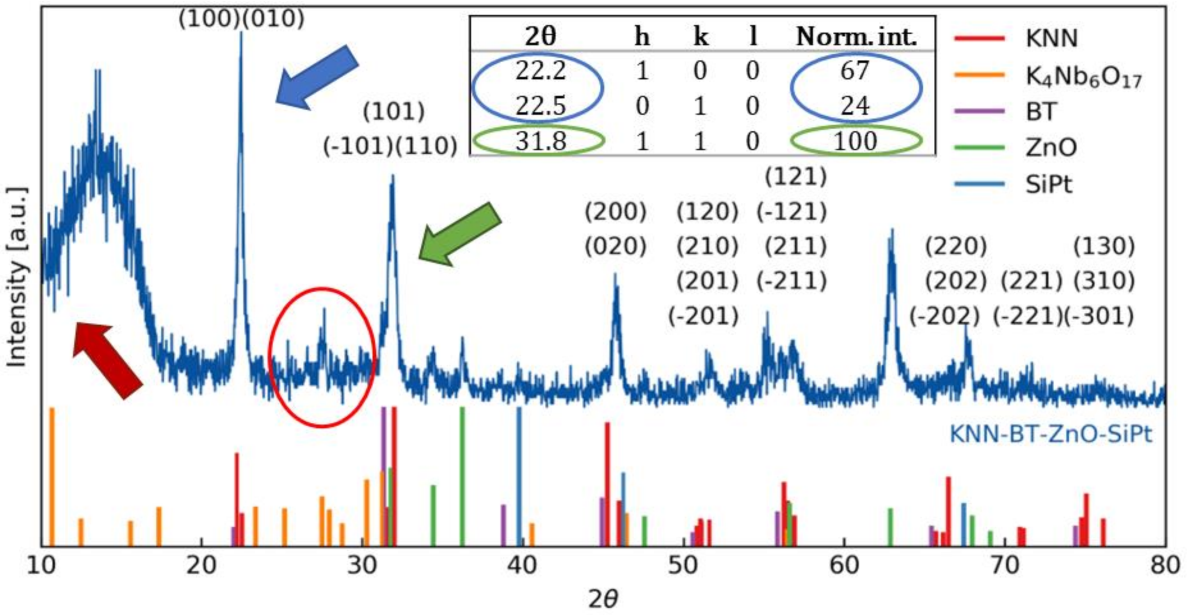

2θ	h	k	l	Norm. int.
22.2	1	0	0	67
22.5	0	1	0	24
31.8	1	1	0	100

Figure 5.6: GI-XRD pattern of the KNN-BT-ZnO-thin film, including a table with normalised intensities for KNN. The strongest peak is observed around 2θ = 22°, indicated with a blue arrow. The strongest reflection was expected from the (110)-plane at 2θ = 31.8°, indicated with a green arrow. The peak that can be assigned to $K_4Nb_6O_{17}$ is marked with a red circle, and the location where it was expected to observe the strongest reflection for $K_4Nb_6O_{17}$ is indicated with the red arrow.

Before achieving the relatively phase pure KNN thin film by introducing the BT intermediate layer between the ZnO and the KNN layers, KNN was deposited directly on the ZnO thin film. Precautions to avoid nucleation of the secondary phase were taken before synthesising the KNN thin films, such as having alkali excess in the precursor solution to counter alkali loss and optimising the synthesis temperature. Despite these attempts, the characterisation of the samples showed presence of the secondary phase $K_4Nb_6O_{17}$.

Different effects that were presumed to promote nucleation of the niobium rich secondary phase $K_4Nb_6O_{17}$ were investigated (see Appendix C.2). In the first experiment, the KNN solution was deposited directly onto the ZnO thin film and heat treated in an oxygen atmosphere. The GI-XRD pattern showed that the secondary phase $K_4Nb_6O_{17}$ was present, indicated with red circles in Figure 5.7. This was confirmed by the elongated grains that were assigned to the $K_4Nb_6O_{17}$ phase in the surface image obtained by SEM [82], indicated by the red arrows in Figure 5.7. The strong reflection at 2θ = 56° is most likely from the substrate.

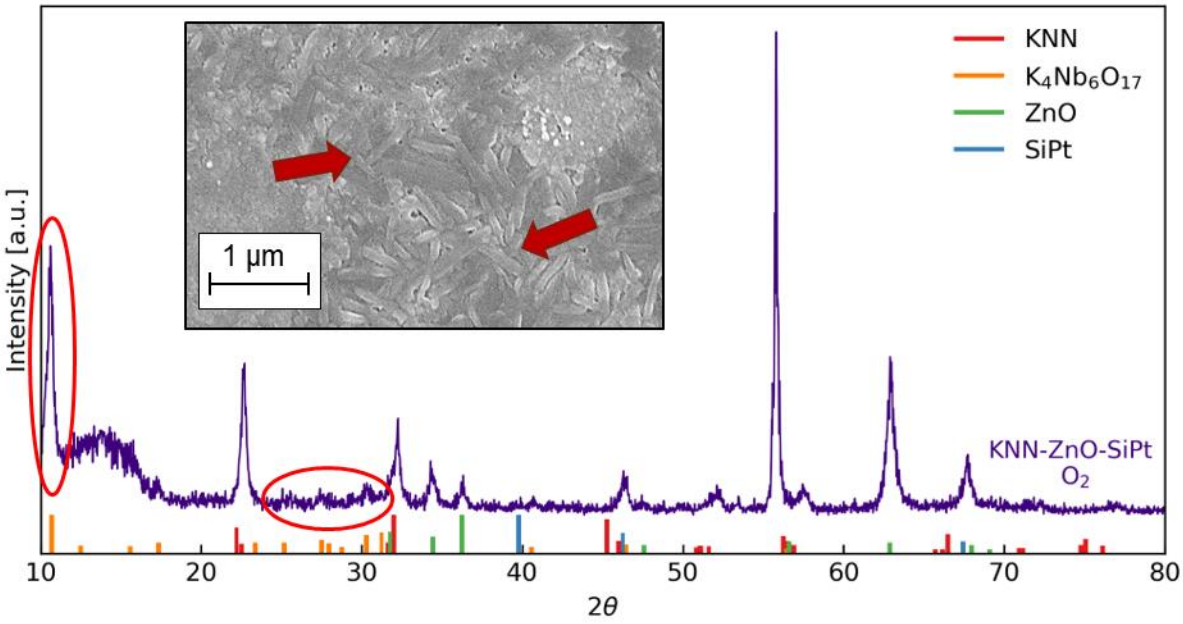

Figure 5.7: GI-XRD pattern of the KNN thin film deposited on the ZnO-SiPt sample and heat treated in an oxygen atmosphere. The diffraction intensities from the $K_4Nb_6O_{17}$ phase are indicated with the red circles. The secondary phase is also observed as elongated grains in the SEM surface image, indicated with the red arrows. The strong reflection at 2θ = 56° is most likely from the substrate.

Based on results reported by Gaukås et al. [72], where increased nucleation of $K_4Nb_6O_{17}$ was observed for KNN thin films heat treated in O_2, it was assumed that the atmosphere caused the formation of the secondary phase. The effect of the atmosphere was therefore assessed by comparing a KNN thin film heat treated in O_2 atmosphere with a KNN film heat treated in an 80/20 mixture of nitrogen and oxygen. It was expected that the KNN thin film heat treated in O_2 would form $K_4Nb_6O_{17}$ and the one heat treated in an 80/20 mixture of N_2 and O_2 would only form $K_{0.5}Na_{0.5}NbO_3$.

The GI-XRD patterns of both films are compared in Figure 5.8 as KNN-ZnO-SiPt O_2 and KNN-ZnO-SiPt O_2+N_2. The GI-XRD patterns disprove the assumption as both samples contained large amounts of the secondary phase, indicated with a red arrow. The strongest diffraction intensity for $K_4Nb_6O_{17}$ was observed at 2θ = 10.7° for both samples, marked with a blue arrow. The diffraction intensity from $K_4Nb_6O_{17}$ was much higher for the KNN thin film heat treated in an 80/20 mixture of N_2 and O_2 than the one in pure O_2. The presence of $K_4Nb_6O_{17}$ phases was also observed in the surface images obtained by SEM, marked with red arrows in Figure 5.8.

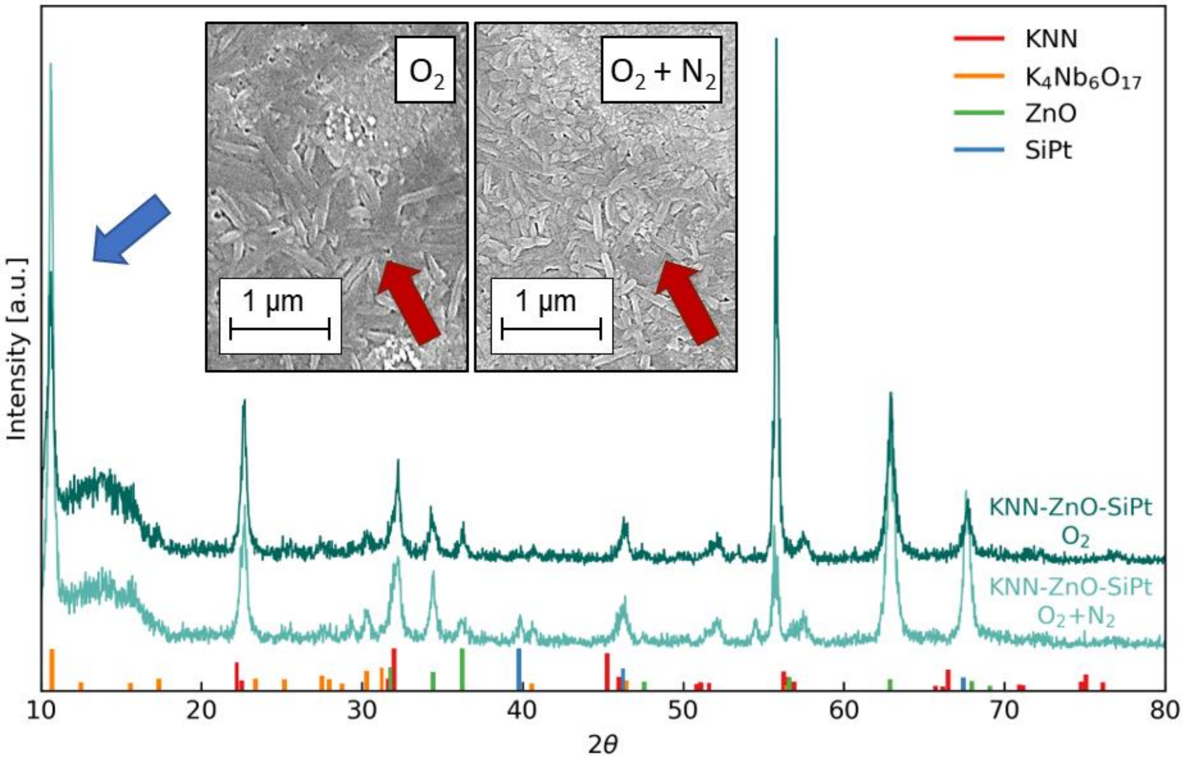

Figure 5.8: GI XRD patterns for KNN-ZnO-SiPt heat treated in O_2 and the KNN-ZnO-SiPt heat treated in an 80/20 mixture of N_2 and O_2. Both samples show a strong diffraction intensity from $K_4Nb_6O_{17}$ around 2θ = 10.7°, marked with a blue arrow. The secondary phase is also observed in the SEM surface images for both thin films, marked with red arrows.

According to the results above, the nucleation of the secondary phase did not seem to be affected by the different atmospheres. The quality of the KNN precursor solution was good (see Appendix C.2); the pH was neutral, and no precipitates were observed in the solution. Also, formation of secondary phases due to alkali loss was unlikely as the KNN precursor solution contained 5 % excess of K and Na. Therefore, it was reasonable to assume that the ZnO layer was causing the nucleation of the secondary phases. To investigate the effect of the ZnO layer, the KNN-ZnO-SiPt sample was compared to a sample of KNN thin film on SiPt with the same precursor solution prepared by Ph.D. candidate Nikolai Helth Gaukås. The GI-XRD patterns of the KNN-SiPt sample and for the KNN-ZnO-SiPt sample are shown in Figure 5.9. The reflections were stronger for the KNN-SiPt sample because the film was 20 layers thicker than the KNN thin film deposited on the ZnO-SiPt sample. The KNN thin film on SiPt was phase pure with strong reflections from the (110)-lattice plane. The red arrows indicate where it was expected to detect $K_4Nb_6O_{17}$ in the KNN-SiPt sample.

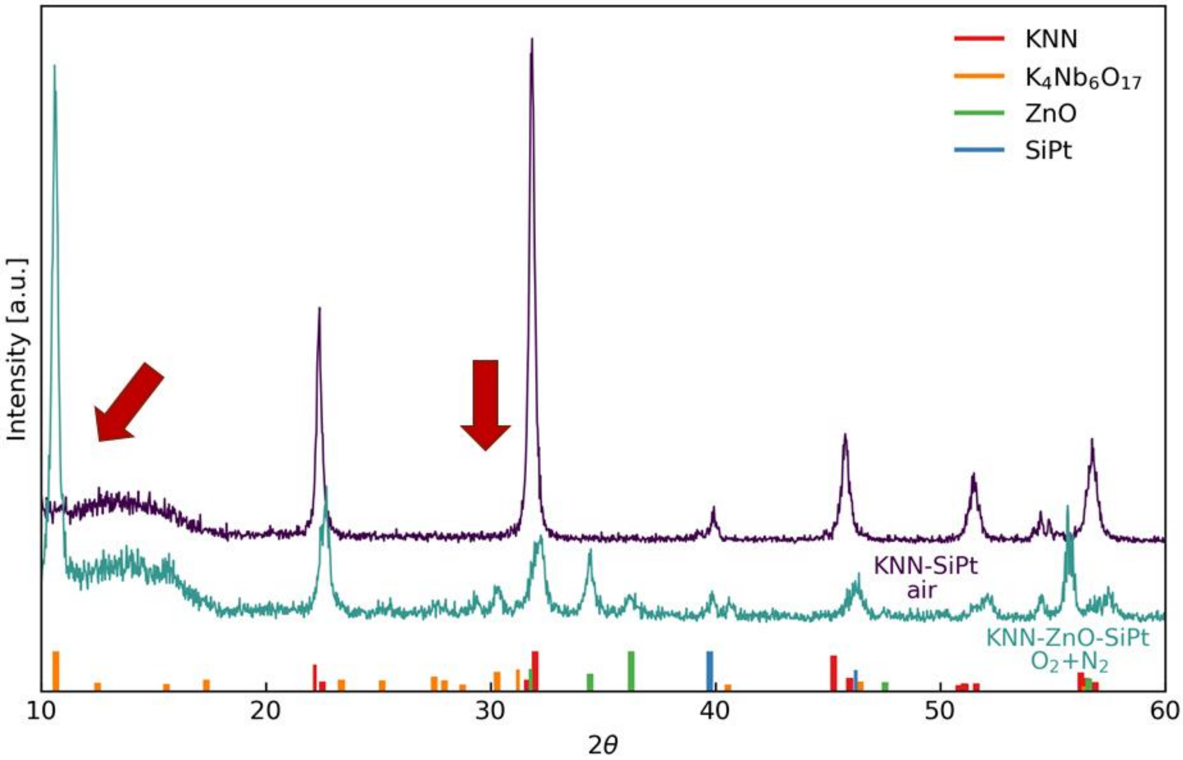

Figure 5.9: GI-XRD pattern for the KNN thin film on SiPt. The corresponding pattern for the KNN-ZnO-SiPt sample is included for comparison. Reflections from the KNN-SiPt sample are stronger because the film is 20 layers thicker than the KNN layer on the ZnO-SiPt substrate. The KNN thin film on SiPt was phase pure and the red arrows indicate where it was expected to detect $K_4Nb_6O_{17}$.

The assumption that ZnO promotes nucleation of $K_4Nb_6O_{17}$ was confirmed as neither the atmosphere or precursor solution affected the formation of $K_4Nb_6O_{17}$ and increasing the temperature to 750 °C only induced a new secondary phase; $K_2Nb_4O_{11}$. To compensate for the nucleation of $K_4Nb_6O_{17}$, barium titanate (BT) was chosen to serve as an intermediate layer between the ZnO and the KNN film to investigate this assumption. BT is also a ferroelectric oxide with a perovskite structure and similar lattice parameters as KNN (cubic BT: a = 4.031 Å, cubic KNN: a = 3.994 Å). The lattice mismatch between cubic KNN and cubic BT was calculated to be – 0.92 %, suggesting that BT is a suitable candidate for testing the ZnO hypothesis (see Appendix C.4).

The GI-XRD patterns for the KNN-BT-ZnO-SiPt sample and the KNN-ZnO-SiPt sample are displayed in Figure 5.10. All the reflections from the KNN-BT-ZnO-SiPt sample were assigned to either KNN, BT, ZnO or SiPt, except a small peak at 2θ = 27°, indicated by the blue arrow. This peak might be assigned to $K_4Nb_6O_{17}$, but because of the absence of the diffraction peak expected at 2θ = 10°, it could be an unidentified phase or noise from the background as previously discussed.

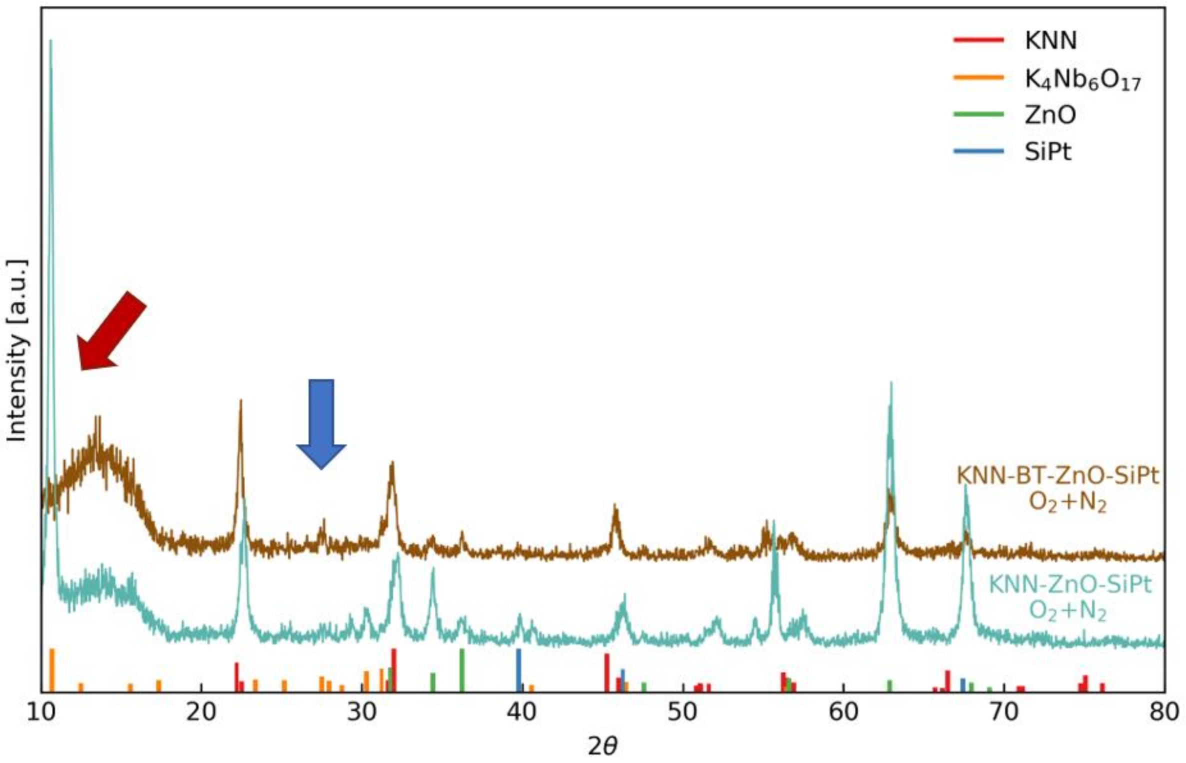

Figure 5.10: GI-XRD pattern for the KNN-BT-ZnO-SiPt sample and the pattern for the KNN-ZnO-SiPt sample. The red arrow indicates where it was expected to detect $K_4Nb_6O_{17}$. All the reflections could be assigned to either KNN, BT, ZnO or SiPt, except a small peak at 2θ = 27°, indicated by the blue arrow. This peak might be assigned to $K_4Nb_6O_{17}$, but because of the absence of the diffraction peak expected at 2θ = 10°, it can be noise from the background or an unidentified phase.

Introducing a BT intermediate layer suppressed the formation of the secondary phase $K_4Nb_6O_{17}$ and resulted in a relative phase pure KNN thin film. Exactly how ZnO can promote the formation of $K_4Nb_6O_{17}$ is not confirmed but studying reactions between ZnO and the different elements in KNN might give an indication. Ji et al. [83, 84] observed no reactions occurring between ZnO and K_2O or ZnO and Na_2O during sintering at 760 °C and 900 °C respectively. Based on these results, a reaction between the ZnO and K or ZnO and Na seemed unlikely, and hence a diffusion layer might not be needed. ZnO can react with Nb_2O_5 and form e.g., $Zn_4Nb_2O_9$, $Zn_2Nb_2O_7$ or $ZnNb_2O_6$ [85]. A few Bragg reflections in the GI-XRD patterns above can be assigned to one of these phases [85]. However, it is more likely that they belong to $K_{0.5}Na_{0.5}NbO_3$, $K_4Nb_6O_{17}$ or ZnO. Volatilisation of alkali metals is the main concern in the KNN precursor solution, as this will cause an imbalance in the cation stoichiometry and increase $K_4Nb_6O_{17}$ content [72]. The effect of limited niobium ions in the precursor requires further investigation, but it is reasonable to assume that less niobium leads to a larger excess of alkali metals and phase pure thin films. Further investigations on the effect of the ZnO thin film must be conducted and maybe evaluate if there is another material that is more suitable as a release layer e.g., $BeCeO_3$, that is an alkaline perovskite.

By analysing the GI-XRD pattern of the released BT-KNN-Pt-PDMS sample (Figure 4.24), the film was determined to be phase pure as all reflections could be assigned to either KNN, BT or Pt. The strongest Bragg reflection was observed from the (111)-plane of platinum at 2θ = 40°.

The reflection at 2θ = 67.5° was also assigned to platinum, but the reflection at 2θ = 46° could be assigned to both platinum and KNN. The Bragg reflection at 2θ = 22° was assigned to KNN and the peak at 2θ = 31° could be both BT and KNN, but the highest reflection for BT was expected at 2θ = 56° as this was the dominating diffraction peak in the GI-XRD patterns for the BT-ZnO-SiPt sample. Because the BT top layer was only 25 nm to 32 nm thick, it was reasonable to assume most of the reflections belonged to the KNN- or Pt layer.

The curved surface of the PDMS on top of the thin oxide layers made the alignment of the sample for the GI-XRD characterisation more difficult, illustrated in Figure 5.11. The KNN thin film is only ~100 nm thick and because the incidence angle for the GI-XRD analysis is very low (2°), the alignment of the sample is very important. According to the product data sheet, spin coating of the viscous PDMS solution at 500 rpm for 30 s was supposed to yield a thick, uniform layer of PDMS on top of the Pt-KNN-BT-ZnO-SiPt stack, but after one week of curing, the PDMS layer was curved. Liu et al. [12] obtained a thin layer of polymer by spin coating on the polymer solution at 3000 rpm. Based on those results, increasing the velocity of the spin coater might yield a thinner film that is easier to align further GI-XRD characterisation. Another method to avoid a curved PDMS layer is to place the sample in a petri dish and fill the petri dish with PDMS. After curing, the sample will have a thick and uniform layer of PDMS.

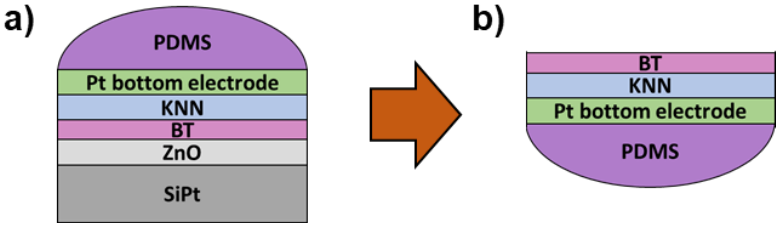

Figure 5.11: a) Illustration of a sample stack after deposition and curing of PDMS (PDMS-Pt-KNN-BT-ZnO-SiPt). b) Illustration of an oxide thin film on the curved PDMS with platinum bottom electrode (BT-KNN-Pt-PDMS). The curved PDMS layer made the alignment of the sample for GI-XRD characterisation difficult. The results are highly dependent on the alignment of the sample as the incidence angle is only 2°.

5.2 Grain morphology and microstructure

The colour difference observed in the ZnO, BT and the KNN thin films (Figure 4.2, Figure 4.7 and Figure 4.13 respectively) is caused by the variation in film thickness. This was confirmed in the SEM cross-section images of the different thin films, where the thickness was determined. The variation in thickness was a result of spin coating the precursor solution onto square shaped substrates; hence, the colour difference was expected. The small difference can be neglected, as the method yielded relatively homogenous thin films and did not seem to influence the final flexible KNN thin film.

The measurements of the grain size in the surface image of the ZnO thin film (0.27 M precursor solution) were taken from a small number of grains, and thus the size is only an estimate. Both surfaces of the two different ZnO thin films were dense and uniform with relatively homogeneous grains. The ideal surface morphology when depositing another solution on top is homogeneous and densely packed grains, illustrated in Figure 5.12 a). If the surface morphology is porous, the top layer will blend in with the layer underneath, illustrated in Figure

5.12 b). The ZnO thin film produced using the 0.27 M solution seemed denser than the ZnO film prepared by the 0.29 M solution. The pores observed in the ZnO thin film from the 0.29 M solution might be caused by diffusion mechanisms or development of gas during heat treatment, but do not seem to be large enough to cause a mixture of BT solution in between the ZnO grains. The difference between the two ZnO thin films might be explained by the different concentrations of the solutions, but as the difference very small, it should not have such a large influence. Another explanation can be a difference in pH, as a too low pH in the precursor solution might cause uneven layers due to etching (dissolving) of the pyrolysed layers during spin coating. Further investigations are required to determine what could cause a difference in the surface morphology.

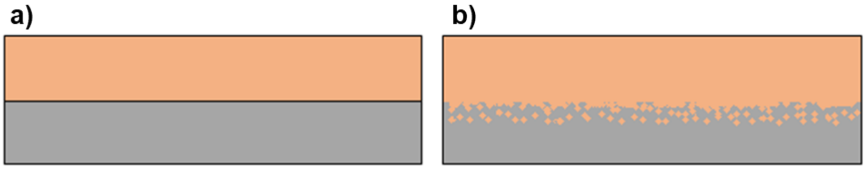

Figure 5.12: Illustration of a) a homogenous, dense cross-section of two separate layers on top of each other and b) a porous thin film, where the top layer has blended with the bottom layer.

The surface morphology of the ZnO thin films was different at 550 °C and at 700 °C, see Figure 5.13 a) and Figure 5.13 b) respectively. At 550 °C, the surface was visibly more porous than at 700 °C and had some elongated grains in between the other seemingly homogeneous grains, indicated with white arrows. These elongated grains and the porous structure have disappeared at 700 °C, and the surface is covered by a layer of homogeneous grains. Some pores are observed on the surface at 700 °C, indicated with white arrows.

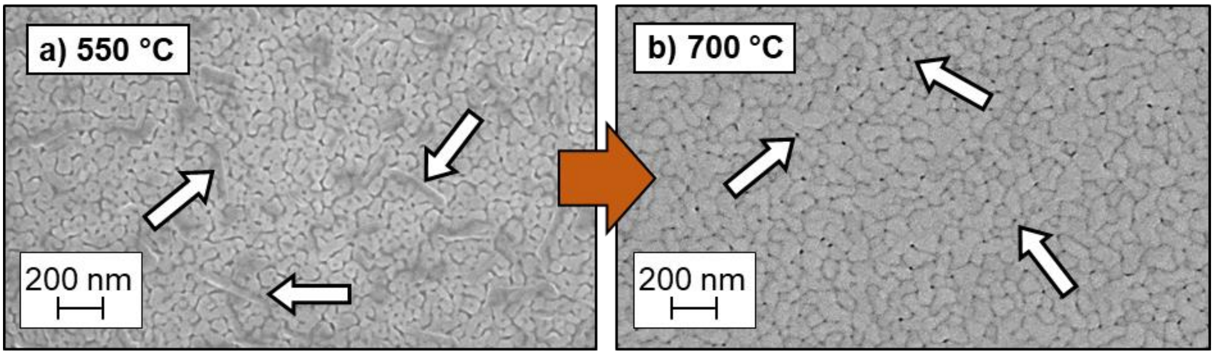

Figure 5.13: SEM images of the surface of the ZnO thin film at a) 550 °C and b) 700 °C. The thin film is visibly more porous at 550 °C than 700 °C. At 550 °C, some elongated grains are observed in between the other grains, indicated with white arrows. At 700 °C, the elongated grains are gone, but there are some small pores indicated with white arrows.

The cross-section images of the ZnO thin film made of the 0.27 M precursor solution showed that the thickness varied from ~134 to ~136 nm. Images of the cross-section of the ZnO thin film made of the 0.29 M precursor solution showed that the thickness varied from ~104 to ~111 nm (see Appendix A.1). Both cross-sections confirmed a dense and uniform film of ZnO that was promising for adding new layers of other materials on top of the ZnO film.

Surface images of the BT thin film imply that the surface is textured and there is island growth of BT across the entire ZnO layer, see Figure 5.14. The formation of these islands is likely due to the Volmer-Weber mechanism, where islands nucleate because of compressive and tensile stresses developed during deposition, making the atoms in the BT solution more coupled to each other than the ZnO thin film [86]. A network will form because of nucleation of multiple islands, and they will eventually cover the substrate as a continuous film as observed in Figure 5.14. The island growth can be related to a lattice mismatch between the ZnO layer and the BT thin film, but because of the different crystal structures (hexagonal and cubic respectively), the difference cannot be calculated straightforward. It is therefore more reasonable to compare the thermal expansion for the two materials to evaluate the mismatch between the layers. The thermal expansion coefficient for BT is larger than the coefficient for ZnO and SiPt, $\alpha_{BT} > \alpha_{ZnO} > \alpha_{Si}$, and therefore, the BT layer experience tensile strain that might induce island growth (see Appendix E) [87-89].

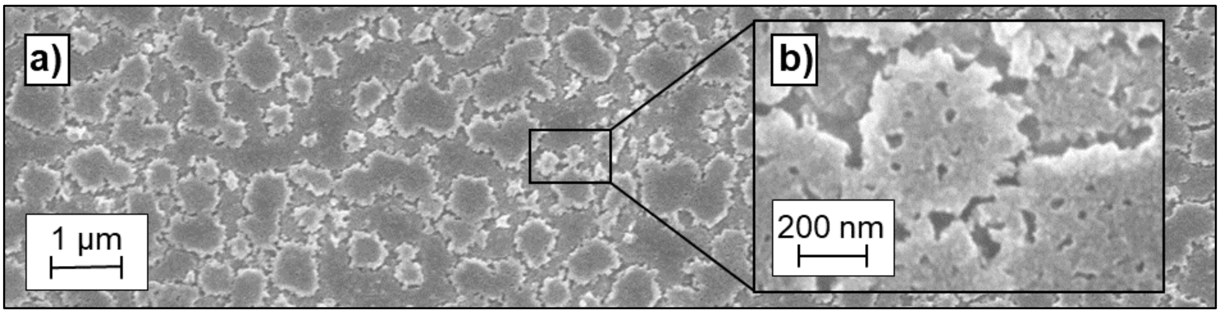

Figure 5.14: SEM image of BT surface with a) low magnitude and b) high magnitude. Both images show the network of BT-islands observed across the entire ZnO layer.

The porous and rough surface of the BT thin film (Figure 5.14) was not optimal for adding a layer of KNN solution as the solution would be distributed in between the islands of BT, as illustrated in Figure 5.12 b). On the other hand, the BT layer was not removed from the KNN thin film after the separation process, and thus the surface morphology might not have affected the result notably. The cross-section images of the BT-ZnO-SiPt sample confirmed a rough layer of BT on top of the ZnO thin film.

The majority of grains observed in the surface images of the KNN thin film have a relatively equal shape with sizes varying from ~30 nm to ~90 nm in diameter. There are a few larger grains in between the small ones varying from ~180 to ~185 nm. The difference in grain size is presumably due to exaggerated grain growth during the annealing of the thin film. The microstructure of a thin film will affect the ferroelectric performance [90], but how much it will influence the mechanical and ferroelectric properties of the KNN thin film must be further investigated.

Due to differences in atomic composition, the ZnO thin film is easy to locate and separate from BT and KNN layers in the SEM images. The KNN-BT layer and the ZnO thin film are observed as two separate layers on top of each other in the cross-section images of the KNN-BT-ZnO-SiPt sample. This might have enhanced the separation process by making the ZnO release layer more accessible for the acid. The voids observed between the two layers might be grains from the ZnO layer torn out when cleaving the sample for the cross-section characterisation. As the lattice mismatch calculation for BT and KNN in the previous section shows, the parameters for the two materials are similar, and therefore, it is more difficult to separate the layers in the SEM. The BT layer is very thin compared to the KNN layer of the sample and the two layers have the same crystal structure, making it difficult to differentiate between the layers in the SEM cross-section images. Except for the BT and the KNN layer, it appears that the layers have not reacted with each other, suggesting that a diffusion barrier between the ZnO film and the BT layer might not be required in future experiments, but this must be further investigated.

The patterned surface of the released BT-KNN-Pt-PDMS sample (Figure 4.8) is most likely a result of depositing KNN precursor solution on top of the rough BT layer caused by island growth. The light and dark areas on the surface might belong to the KNN and the BT phases. It seems like there is a small height difference separating these areas and the light area appears to have smaller grains compared to the darker area. Another assumption is that the two areas belong to the BT thin film and some leftovers from the ZnO thin film, however, all the ZnO film was expected to be etched away by the acetic acid. The patterned surface needs further investigation to conclude what phases the patterned surface consists of and what is causing it. An element mapping with SEM imaging might help to determine what phases are present at the surface.

Establishing the curing conditions for PDMS was crucial as a too high curing temperature would cause shrinkage of the PDMS layer, inducing compressive stress and fractures in the ceramic thin film after the separation process [91]. Multiple fractures were observed across the surface of a KNN thin film on PDMS support that was cured at 60 °C for 4 hours, illustrated in Figure 5.15 a). A patterned, but less fractured surface was observed for the BT-KNN-Pt-PDMS sample where the PDMS was cured in room temperature for seven days, illustrated in Figure 5.15 b). These observations comply with the results reported by Madsen et al. [91] where curing of PDMS at 60 °C caused 1.67 % shrinkage of the PDMS layer while curing in room temperature did not cause any shrinkage. It is important to note that the BT-KNN-Pt sample consists of multiple layers that provide additional mechanical support to the KNN thin film, while the other KNN thin film only consists of a ~100 nm thick film on a polymer. Direct comparison is challenging as one sample can be more fragile than the other, and thus, the effect of shrinkage should be further investigated.

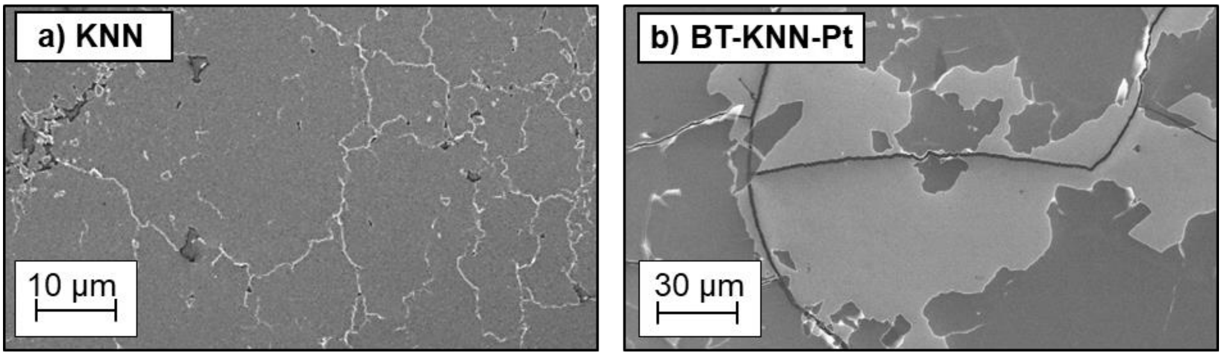

Figure 5.15: SEM images of the ceramic thin films on PDMS support. a) Multiple fractures were observed across the surface of a KNN thin film on PDMS support that was cured at 60 °C for 4 hours. b) A patterned, but less fractured surface was observed for the BT-KNN-Pt-PDMS sample where the PDMS was cured at room temperature for seven days.

The curved PDMS layer discussed in section 5.1 (Figure 5.12) also influenced the preparation of the sample for SEM characterisation. Mounting the flexible thin film onto the sample holder resulted in some bending of the film caused by contact with the carbon tape on top of the ceramic thin film, as well as the sample holder. The mounting of the sample might have contributed to additional fractures of the ceramic thin film. The thermal expansion coefficient for KNN is larger than the coefficient for SiPt, $\alpha_{KNN} > \alpha_{Si}$, and therefore, the KNN layer experience tensile strain that might have induced fractures during the release process (see Appendix E).

The cross-section images of the Pt-BT-KNN-Pt-PDMS sample shows two separate layers on top of each other; the BT-KNN layer on top of the platinum bottom electrodes. The layers appear to have the same height that corresponds to the measured film thickness of the KNN-BT-ZnO-SiPt sample, ~119 nm to ~124 nm, and the 100 nm thick platinum electrode deposited. The cleaving of the sample was not optimal, but the characterisation of the cross-section gives an indication that the thin film can withstand bending to some extent, as seen in Figure 4.30 where a freestanding area without PDMS support was observed.

5.3 Release process

Removing the PDMS on the edges of the sample stack (PDMS-Pt-KNN-BT-ZnO on SiPt) to ensure that the ZnO layer was available for the etchant, most likely enhanced the release processes. The temperature of the acetic acid was kept at 58 °C ± 1 °C throughout both separation processes. The effect of increased temperature has not been further investigated. The first release process (Figure 4.21) and the second release process (Figure 4.26) with PDMS-Pt-KNN-BT-ZnO-SiPt samples took approximately 2 h and 3 h, respectively. Another separation process with a PDMS-KNN-ZnO-SiPt sample took almost 2 h (see Appendix D.1). The processes described above took longer than the 35-40 min reported for the separation in the specialisation project [17], but in return, they were more successful as Figure 5.16 shows. The flexible film from the specialisation project was missing two large pieces of the thin film (Figure 5.16 a)), while the complete thin film was successfully transferred in the other processes, except a few fragments in one film (Figure 5.16 c)).

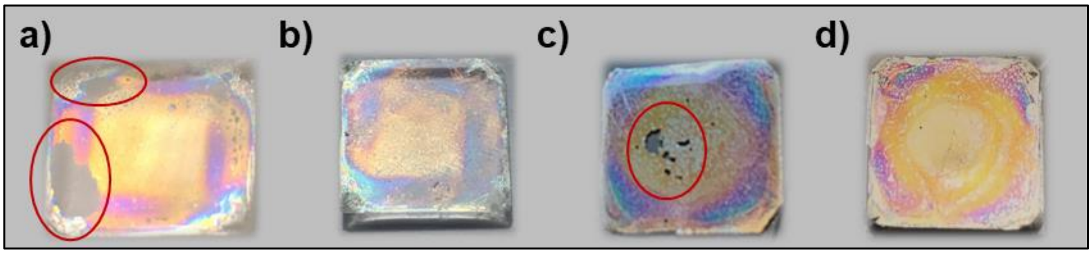

Figure 5.16: Image of four different flexible KNN thin films. a) The flexible thin film that was reported on in the specialisation project [17]. Large pieces of the ceramic film were not transferred onto the polymer, indicated with red circles. b) A successful release process of a KNN-PDMS substrate, although the KNN thin film was not phase pure. c) The first release process with a relative phase pure KNN thin film, where the BT-KNN-Pt sample was transferred onto the PDMS support. A few pieces of the film were not transferred onto the polymer, indicated with a red circle. d) The second, more successful release process with a relatively phase pure KNN thin film. The entire BT-KNN-Pt sample was transferred onto the PDMS support.

The first release process of the PDMS-Pt-KNN-BT-ZnO-SiPt samples was less successful than the second release process because of rough handling during the separation process. The second sample was not touched during the process, except at the end where it was carefully moved on to a silicon substrate for extra support. The results clearly show that a careful release process with no rough handling gives a better transfer process, as illustrated above in Figure 5.16.

The piezoelectric properties of the KNN thin film are most likely affected by the acetic acid as KNN is hygroscopic and sensitive to A-site (potassium and sodium) cation release in acidic mediums [92]. How critical the effect of the acetic acid is, requires further investigation. It is also important to estimate how the flexible KNN thin film will function *in vivo* in direct contact with body fluids.

The GI-XRD patterns of the two empty SiPt substrates after the release processes are compared in Figure 5.17. The GI-XRD pattern for the pure SiPt is also included. The Bragg reflections observed from the empty SiPt from the first release process can be assigned to the missing pieces of the BT-KNN-Pt-PDMS sample, indicated with the green circles. The strong reflection at 2θ = 57° is most likely from the substrate and is the same peak that was observed in the GI-XRD pattern for ZnO film pyrolysed at 550 °C (Figure 5.3) and for the BT film (Figure 5.4). The GI-XRD pattern of the empty SiPt after the second release process confirms that more careful handling during the release process gives a more successful transfer of the ceramic thin film.

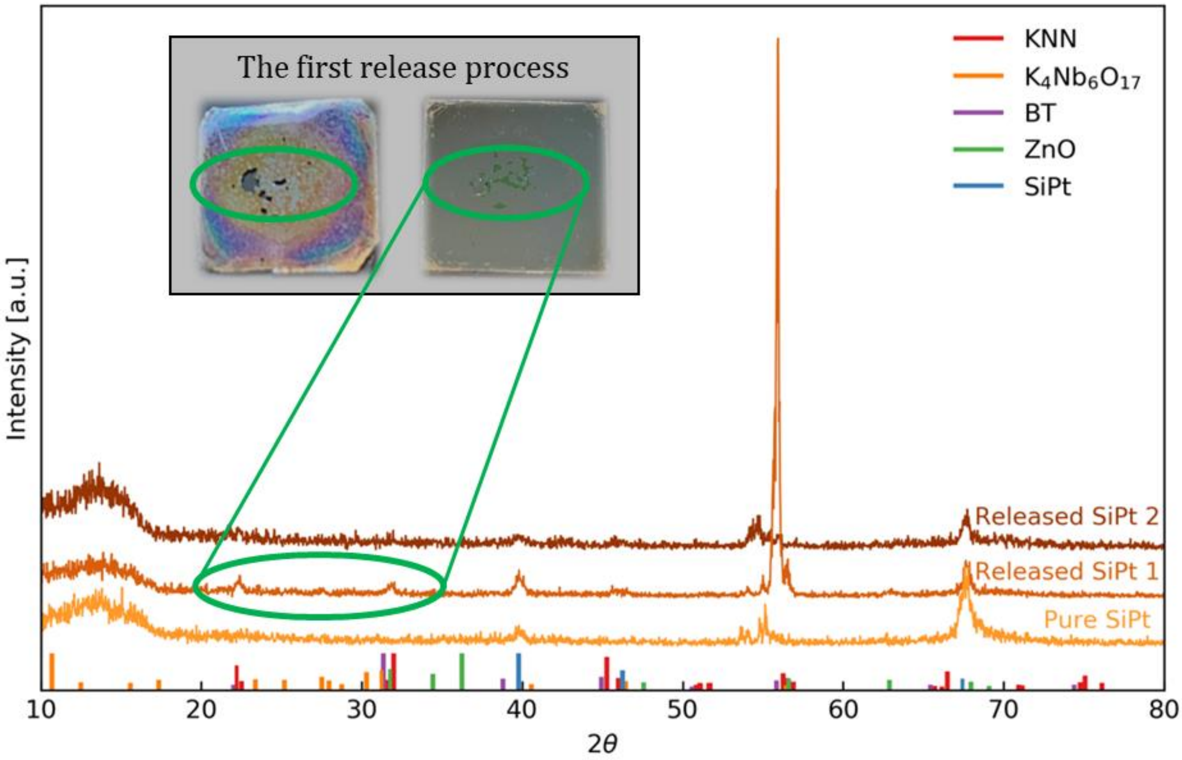

Figure 5.17: GI-XRD patterns of the empty SiPt substrates after the two release processes where two BT-KNN-Pt thin films were transferred onto a PDMS support. The Bragg reflections observed from the first empty SiPt substrate can be assigned to the missing pieces of the BT-KNN-Pt sample, indicated with the green circles. The second empty SiPt seemed to be pure SiPt.

5.4 Ferroelectric measurement

E-beam evaporation gave even platinum electrodes on each side of the ceramic thin film. The bottom electrode did not cover the entire surface of the thin film because the shadow mask covered the corners. This is also seen in the image of the flexible thin films after the release process (Figure 4.26), where the corners are rounded, but overall, it did not seem to affect the result notably. When depositing noble metal electrodes on an oxide, it is recommended to use titanium as an adhesion layer, though the platinum seemed to attach well to the oxide thin film. Titania can be oxidised to TiO_2, which is known to improve adhesion between noble metals like platinum and oxide films [93].

Despite very careful handling during and after the release process, the second BT-KNN-Pt sample was fractured during the mounting of the sample into the shadow mask for deposition of top electrodes. The film was probably bent up to ~45°, that according to calculations on a flexible PZT thin film [41], is too much bending for a thin ceramic film to withstand fractures. The mechanical strength of the KNN thin film should be further investigated, e.g., by nanoindentation.

The top electrodes were deposited on a fractured surface of the ceramic thin film and it was therefore expected to observe leakage during the ferroelectric measurements as the microstructure of a thin film has a significant impact on the ferroelectric performance, discussed at the beginning of section 5.2. This resulted in a leaking ferroelectric *P-E* hysteresis loop for the flexible ceramic thin film, illustrated in Figure 4.31. New ferroelectric measurements must therefore be performed on new flexible ceramic thin films to evaluate the ferroelectric behaviour of BT-KNN on a PDMS support.

6 Further work

Many interesting and promising results on the synthesis of flexible phase pure KNN thin film were achieved in this work. However, new samples must be prepared to conduct better ferroelectric measurements. It will be essential to deposit a uniform layer of PDMS to achieve better alignment for GI-XRD characterisation and avoid fracturing the thin films when mounting the samples for SEM characterisation. A more uniform layer of PDMS may also contribute to easier handling of the flexible film, as it can be taped to a rigid substrate without further bending the film. A uniform PDMS layer will simplify the mounting of the sample in the shadow mask so that the top electrodes can be deposited on a continuous oxide film, that most likely will improve the ferroelectric measurements. More information on the ferroelectric properties would help establish a greater understanding of flexible KNN thin film for use in biomedical applications. It would also be interesting to compare a flexible KNN thin film with a compressed one as Liu et al. [12] did for PZT.

The mechanical strength of the thin film should be measured, and thus provide more information and indication on which applications the film can be utilised in. It would also be interesting to know what kind of thermal, growth and epitaxial strains that are present in the thin film.

Further research on the silicon substrate is important to evaluate the effect it has on the KNN films and could give a greater understanding of how the substrate will affect the thin films regarding lattice mismatch and texturing. Regarding the release layer, it could be useful to explore what is the preferred orientation of the ZnO thin film concerning the BT and the KNN layer. Maybe it is possible to texture the ZnO thin film in a manner that prevents nucleation of the $K_4Nb_6O_{17}$ when depositing a KNN precursor solution directly onto the ZnO film. Further investigation on how the ZnO layer affects the BT layer and the KNN layer will need to be performed as the results from this thesis only can be used as an indication of what kind of impact the ZnO film has. The ZnO can also be replaced with another alkaline material that might not promote nucleation of $K_4Nb_6O_{17}$, and in addition, can withstand temperatures up to 710 °C and will dissolve in weak acid e.g., the $BeCeO_3$ perovskite.

Element analysis by SEM or TEM would be interesting to perform on the surface of the released thin film and on the cross-section of the KNN-BT-ZnO-SiPt sample to determine which elements are present. Such an analysis could indicate if a diffusion layer is required between the layers, even though it seems from the cross-section images that only the BT and the KNN layer have blended.

How the A-site cation release in KNN during the release process affects the piezoelectric properties of the flexible thin film requires further investigation. It is also important to estimate how the flexible KNN thin film will function *in vivo* in direct contact with body fluids.

Finally, the possibility of reuse the empty SiPt substrates after the release process should be investigated as the focus on sustainability is increasing.

7 Conclusion

In this work, a flexible, phase pure and ferroelectric KNN thin film was prepared using chemical solution deposition. The ceramic thin film was first deposited on top of a zinc oxide (ZnO) release layer on a thermally robust platinum coated silicon (SiPt) substrate and transferred onto a flexible polymer support by etching away the ZnO layer.

Spin coating yielded uniform layers of precursor solutions on top of the SiPt substrate, for all layers of the thin film stack. The SiPt substrate favours the wurtzite structure of ZnO and induces texturing of the ZnO crystals in (103)-lattice plane direction.

Nucleation of $K_4Nb_6O_{17}$ was promoted by the ZnO layer and was not visibly affected by atmosphere. Increasing the temperature from 700 °C to 750 °C formed a new secondary phase; $K_2Nb_4O_{11}$. Introducing barium titanate as an intermediate layer between the ZnO thin film and the KNN thin film resulted in phase pure KNN thin films.

The curing of PDMS in room temperature prevented fractures in the ceramic thin film induced by shrinkage of the PDMS layer. However, careless handling of the thin film before deposition of the top electrodes resulted in a leaking ferroelectric *P-E* hysteresis loop for the flexible ceramic thin film. This result indicates that careful handling of the thin film is important in every processing step as the film is easily fractured and the ferroelectric behaviour depends on the microstructure. New ferroelectric measurements are recommended on new flexible ceramic thin films to evaluate the ferroelectric behaviour of BT-KNN on a PDMS support.

Future work should focus on careful handling of the thin film in each step of the synthesis. It was easier to handle the thin film and prevent fractures when it was taped to a rigid substrate, which can improve the measurements during characterisation. One issue is the PDMS layer that cannot be curved as this will bend the ceramic film. The curvature of the PDMS layer might cause issues, as bending it might damage the ceramic film.

This work focused on developing a method to deposit dense, phase pure piezoelectric ceramic thin films on a polymer substrate. Further research is required to improve the method to be able to perform ferroelectric measurements on the flexible thin film.

References

1. Jaffe, H., *Piezoelectric ceramics.* Journal of the American Ceramic Society, 1958. **41**(11): p. 494-498.
2. Katzir, S., *The Discovery of the piezoelectric effect.* Archive for History of Exact Sciences, 2003. **57**(1): p. 61.
3. Roedel, J., et al., *Perspective on the development of lead-free piezoceramics.* Journal of the American Ceramic Society, 2009. **92**(6): p. 1153-1177.
4. Wolny, W.W., *European approach to development of new environmentally sustainable electroceramics.* Ceramics International, 2004. **30**(7): p. 1079-1083.
5. European Parliament, C.o.t.E.U., *Directive 2011/65/EU of the European Parliament and of the Council of 8.June 2011 on the restriction of the use of certain hazardous substances in electrical and electronic equipment*, C.o.t.E.U. European Parliament, Editor. 2011.
6. Flora, G., D. Gupta, and A. Tiwari, *Toxicity of lead: a review with recent updates.* Interdisciplinary Toxicology, 2012. **5**(2): p. 47.
7. Ringgaard, E. and T. Wurlitzer, *Lead-free piezoceramics based on alkali niobates.* Journal of the European Ceramic Society, 2005. **25**(12): p. 2701-2706.
8. Yasuyoshi, S., et al., *Lead-free piezoceramics.* Nature, 2004. **432**(7013): p. 84.
9. Ratner, B.D., *Biomaterials science: an introduction to materials in medicine*. 2013, Elsevier/Academic Press: Amsterdam, Netherlands.
10. Richerson, D.W., *Modern ceramic engineering: properties, processing, and use in design*. 4th ed. Materials engineering. 2018, Boca Raton, Fla: CRC Press.
11. Pham, K.-N., et al., *Epitaxial* $K_{0.5}Na_{0.5}NbO_3$ *thin films by aqueous chemical solution deposition.* Royal Society Open Science, 2019. **6**: p. 180989.
12. Liu, T., et al., *High-temperature crystallized thin-film PZT on thin polyimide substrates.* Journal of Applied Physics, 2017. **122**(16).
13. Kozuka, H., *Wet processing for the fabrication of ceramic thin films on plastics.* Journal of Materials Research and Technology, 2013. **28**(5): p. 673-688.
14. Beyler, C.L. and M.M. Hirschler, *Thermal decomposition of polymers.* SFPE handbook of fire protection engineering, 2002. **2**.
15. Moretto;, H.H., M. Schulze;, and G. Wagner, *Silicones.* Wiley Online Library, 2000.
16. Liu, M., J. Sun, and Q. Chen, *Influences of heating temperature on mechanical properties of polydimethylsiloxane.* Sensors and Actuators A: Physical, 2009. **151**(1): p. 42-45.
17. Klaussen, R.H., *Flexible, biocompatible lead-free piezoelectric thin films for biomedical applications*. 2017, Norwegian University of Science and Technology.
18. Tilley, R.J.D., *Understanding solids: the science of materials*. 2nd ed. 2013: Wiley. 576 pp.
19. West, A.R., *Solid state chemistry and its applications*. 2nd ed. 2014, Chichester: Wiley.
20. Wang, Z.L. and Y. Liu, *Piezoelectric effect at nanoscale*, in *Encyclopedia of nanotechnology*, B. Bhushan, Editor. 2012, Springer Netherlands: Dordrecht. p. 2085-2099.
21. Sebastian, M.T., *Chapter six -* ABO_3 *type perovskites*, in *Dielectric materials for wireless communication*, M.T. Sebastian, Editor. 2008, Elsevier: Amsterdam. p. 161-203.
22. Jin, L., F. Li, and S. Zhang, *Decoding the fingerprint of ferroelectric loops: comprehension of the material properties and structures.* Journal of the American Ceramic Society, 2014. **97**(1): p. 1-27.
23. Li, J.-F., et al., *(K,Na)*NbO_3*-based lead-free piezoceramics: fundamental aspects, processing technologies, and remaining challenges.* Journal of the American Ceramic Society, 2013. **96**(12): p. 3677-3696.
24. Cambridge, U.o. *PZT.* 2004-2018 [cited 2018 15.10]; Available from: https://www.doitpoms.ac.uk/tlplib/piezoelectrics/pzt.php.
25. Setter, N., et al., *Ferroelectric thin films: Review of materials, properties, and applications.* Journal of applied physics, 2006. **100**(5): p. 051606.
26. Chen-Glasser, M., et al., *Piezoelectric materials for medical applications*, in *Piezoelectricity - organic and inorganic materials and applications*. 2018, IntechOpen.
27. Egerton, L. and D.M. Dillon, *Piezoelectric and dielectric properties of ceramics in the system of potassium-sodium niobate.* Journal of the American Ceramic Society, 1959. **42**: p. 438-42.

28. Wu, J., D. Xiao, and J. Zhu, *Potassium-sodium niobate lead-free piezoelectric materials: past, present, and future of phase boundaries.* American Chemical Society, 2015. **115**(7): p. 2559-2595.
29. Weller, M.T., P.W. Atkins, and D.F. Shriver, *Inorganic chemistry*. 6th ed. 2014, Oxford: Oxford University Press.
30. Momma, K. and F. Izumi, *VESTA: a three-dimensional visualization system for electronic and structural analysis.* Journal of Applied Crystallography, 2008. **41**(3): p. 653-658.
31. Haertling, G., *Properties of hot-pressed ferroelectric alkali niobate ceramics.* Journal of the American Ceramic Society, 1967. **50**(6): p. 329-330.
32. Li, J.F., et al., *Ferroelectric and piezoelectric properties of fine-grained* $Na_{0.5}K_{0.5}NbO_3$ *lead-free piezoelectric ceramics prepared by spark plasma sintering.* Journal of the American Ceramic Society, 2006. **89**(2): p. 706-709.
33. Tennery, V.J. and K.W. Hang, *Thermal and X-Ray diffraction studies of the* $NaNbO_3$–$KNbO_3$ *system.* Journal of Applied Physics, 1968. **39**(10): p. 4749-4753.
34. Tellier, J., et al., *Crystal structure and phase transitions of sodium potassium niobate perovskites.* Solid State Sciences, 2009. **11**(2): p. 320-324.
35. Wu, L., et al., *Influence of compositional ratio K/Na on physical properties in* $(K_xNa_{1-x})NbO_3$ *ceramics.* Journal of Applied Physics, 2008. **103**(8): p. 084116.
36. Lai, F., et al., *Influence of Li content on electrical properties of highly piezoelectric* $(Li,K,Na)NbO_3$ *thin films prepared by sol-gel processing.* Journal of Applied Physics, 2009. **106**(6): p. 064101.
37. Haq, M., *Application of piezo transducers in biomedical science for health monitoring and energy harvesting problems.* Materials Research Express, 2018. **6**(2): p. 022002.
38. Dagdeviren, C., et al., *Conformal piezoelectric energy harvesting and storage from motions of the heart, lung, and diaphragm.* Proceedings of the National Academy of Sciences, 2014. **111**(5): p. 1927-1932.
39. Hwang, G.T., et al., *Flexible piezoelectric thin-film energy harvesters and nanosensors for biomedical applications.* Advanced healthcare materials, 2015. **4**(5): p. 646-658.
40. Zurbuchen, A., et al., *Energy harvesting from the beating heart by a mass imbalance oscillation generator.* Annals of biomedical engineering, 2013. **41**(1): p. 131-141.
41. Park, K.I., et al., *Highly-efficient, flexible piezoelectric PZT thin film nanogenerator on plastic substrates.* Advanced Materials, 2014. **26**(16): p. 2514-2520.
42. Karami, M.A. and D.J. Inman, *Powering pacemakers with heartbeat vibrations*, in *Micro Energy Harvesting*. 2015, John Wiley & Sons. p. 435-458.
43. Park, K.-I., et al., *Piezoelectric* $BaTiO_3$ *thin film nanogenerator on plastic substrates.* Nano letters, 2010. **10**(12): p. 4939-4943.
44. Karami, M.A. and D.J. Inman, *Powering pacemakers from heartbeat vibrations using linear and nonlinear energy harvesters.* Applied Physics Letters, 2012. **100**(4): p. 042901.
45. Bhatia, D., et al., *Pacemakers charging using body energy.* Journal of Pharmacy And Bioallied Sciences, 2010. **2**(1): p. 51.
46. Ohm, O.J. and D. Danilovic, *Improvements in pacemaker energy consumption and functional capability: four decades of progress.* Pacing and clinical electrophysiology, 1997. **20**(1): p. 2-9.
47. Kanno, I., et al., *Power-generation performance of lead-free* $(K,Na)NbO_3$ *piezoelectric thin-film energy harvesters.* Sensors and Actuators A: Physical, 2012. **179**: p. 132-136.
48. Tsujiura, Y., et al., *Lead-free piezoelectric MEMS energy harvesters of* $(K,Na)NbO_3$ *thin films on stainless steel cantilevers.* Japanese Journal of Applied Physics, 2013. **52**(9S1): p. 09KD13.
49. Siddiqui, S., et al., *A durable and stable piezoelectric nanogenerator with nanocomposite nanofibers embedded in an elastomer under high loading for a self-powered sensor system.* Nano Energy, 2016. **30**: p. 434-442.
50. Sobajima, S., et al., *Production and properties of transparent electroconductive coating on polyester film.* Japanese Journal of Applied Physics, 1974. **13**(S1): p. 475-478.
51. Itoyama, K., *Properties of Sn-doped indium oxide coatings deposited on polyester film by high rate reactive sputtering.* Journal of the Electrochemical Society, 1979. **126**(4): p. 691-694.

52. Jones, A.C. and M.L. Hitchman, *Chemical vapour deposition: precursors, processes and applications*, in *Chemical vapor deposition*. 2009, Royal Society of Chemistry: Cambridge, UK.
53. Mansingh, A. and C.V. Kumar, *Rf-sputtered indium tin oxide films on water-cooled substrates.* Thin Solid Films, 1988. **167**(1-2): p. L11-L14.
54. Mukherjee, A., *The deposition of transparent conductive oxide thin films onto large sheets of glass, acrylic and polycarbonate.* Vacuum, 1989. **39**(6): p. 537-540.
55. Mitchell, D.R.G., G. Triani, and Z. Zhang, *Hydrothermal crystallization of amorphous titania films deposited using low temperature atomic layer deposition.* Thin Solid Films, 2008. **516**(23): p. 8414-8423.
56. Gockeln, M., et al., *Flame aerosol deposited $Li_4Ti_5O_{12}$ layers for flexible, thin film all-solid-state Li-ion batteries.* Nano Energy, 2018. **49**: p. 564-573.
57. Schneller, T., et al., *Chemical solution deposition of functional oxide thin films*. 2013, Illinois, USA: Springer.
58. Deki, S. and Y. Aoi, *Synthesis of metal oxide thin films by liquid-phase deposition method.* Journal of materials research, 1998. **13**(4): p. 883-890.
59. Königer, T. and H. Münstedt, *Coatings of indium tin oxide nanoparticles on various flexible polymer substrates: Influence of surface topography and oscillatory bending on electrical properties.* Journal of the Society for Information Display, 2008. **16**(4): p. 559-568.
60. Deki, S., et al., *Preparation and characterization of Au-dispersed TiO_2 thin films by a liquid-phase deposition method.* Journal of Materials Chemistry, 1996. **6**(12): p. 1879-1882.
61. Nagayama, H., H. Honda, and H. Kawahara, *A new process for silica coating*. 1988, Journal of the Electrochemical Society. p. 2013-2016.
62. Niesen, T.P. and M.R. De Guire, *Deposition of ceramic thin films at low temperatures from aqueous solutions.* Solid State Ionics, 2002. **151**(1-4): p. 61-68.
63. Shimizu, K., et al., *Low-temperature synthesis of anatase thin films on glass and organic substrates by direct deposition from aqueous solutions.* Thin Solid Films, 1999. **351**(1-2): p. 220-224.
64. Schwartz, R.W., *Chemical solution deposition of perovskite thin films.* Chemistry of materials, 1997. **9**(11): p. 2325-2340.
65. Aegerter, M.A. and N. Al-Dahoudi, *Wet-chemical processing of transparent and antiglare conducting ITO coating on plastic substrates.* Journal of sol-gel science and technology, 2003. **27**(1): p. 81-89.
66. Imai, H. and H. Hirashima, *Preparation of porous anatase coating from sol-gel-derived titanium dioxide and titanium dioxide-silica by water-vapor exposure.* Journal of the American Ceramic Society, 1999. **82**(9): p. 2301-2304.
67. Kotani, Y., et al., *Formation of anatase nanocrystals in sol-gel derived TiO_2-SiO_2 thin films with hot water treatment.* Journal of Sol-Gel Science and Technology, 2000. **19**(1-3): p. 585-588.
68. Matsuda, A., et al., *Transparent anatase nanocomposite films by the sol–gel process at low temperatures.* Journal of the American Ceramic Society, 2000. **83**(1): p. 229-231.
69. Imai, H., et al., *Ultraviolet-laser-induced crystallization of sol-gel derived indium oxide films.* Journal of sol-gel science and technology, 1998. **13**(1-3): p. 991-994.
70. Asakuma, N., et al., *Ultraviolet-laser-induced crystallization of sol-gel derived inorganic oxide films.* Journal of Sol-Gel Science and Technology, 2000. **19**(1-3): p. 333-336.
71. Raeder, T.M., et al., *Enhanced in-plane ferroelectricity in $BaTiO_3$ thin films fabricated by aqueous chemical solution deposition.* AIP Advances, 2018. **8**(10): p. 105228.
72. Gaukås, N.H., et al., *Controlling phase purity and texture of $K_{0.5}Na_{0.5}NbO_3$ thin films by aqueous chemical solution deposition.* Materials, 2019. **Accepted: june 2019**.
73. Dale, S.M., *Lead-free piezoelectric materials for medical application*. 2018, Norwegian University of Science and Technology.
74. Yoshio, K., et al., *Crystal structure of ZnO:Li at 293K and 19K by X-ray diffraction.* Ferroelectrics, 2001. **264**: p. 133.
75. Ellner, M., *Zusammenhang zwischen structurellen und thermo-dymamishen eigenschaften bei phasen der kupfer-familie in T10-B4-systemen.* Journal of the Less Common Metals, 1981(78): p. P21.

76. Naka, S., et al., *Change from metastable cubic to stable tetragonal form of submicron barium titanate.* Bulletin of the Chemical Society of Japan, 1974. **47**(5): p. 1168-1171.
77. Gasperin, M. and M.T.L. Bihan, *Mecanisme d`hydratation des niobates alcalins lamellaires de formule* $A_4Nb_4O_{17}$ *(A = K, Rb, Cs).* Journal of Solid State Chemistry, 1982. **43**: p. 346.
78. Rooksby, H.P. and B. Lewis, *Relations between the structures of phases in the system platinum-molybdenum.* Journal of the Less Common Metals, 1964. **6**: p. 451.
79. Kim, S.-K., S.-Y. Jeong, and C.-R. Cho, *Structural reconstruction of hexagonal to cubic ZnO films on* $Pt/Ti/SiO_2/Si$ *substrate by annealing.* Applied Physics Letters, 2003. **82**(4): p. 562-564.
80. Durán, P., et al., *On the formation of an oxycarbonate intermediate phase in the synthesis of* $BaTiO_3$ *from (Ba,Ti)-polymeric organic precursors.* Journal of the European Ceramic Society, 2002. **22**(6): p. 797-807.
81. Kumar, S., G.L. Messing, and W.B. White, *Metal organic resin derived barium titanate: I, Formation of barium titanium oxycarbonate intermediate.* Journal of the American Ceramic Society, 1993. **76**(3): p. 617-624.
82. Madaro, F., et al., *Molten salt synthesis of* $K_4Nb_6O_{17}$*,* $K_2Nb_4O_{11}$ *and* KNb_3O_8 *crystals with needle- or plate-like morphology.* CrystEngComm, 2011. **13**(5): p. 1304-1313.
83. Ji, L., et al., *Phase relations and flux research for zinc oxide crystal growth in the* $ZnO\text{-}Na_2O\text{-}P_2O_5$ *system.* Journal of Alloys and Compounds, 2008. **465**(1-2): p. 436-441.
84. Ji, L., et al., *Phase relations and flux research for zinc oxide crystal growth in the* $ZnO\text{-}K_2O\text{-}P_2O_5$ *system.* Journal of Alloys and Compounds, 2009. **470**(1-2): p. 336-339.
85. Tarakina, N.V., et al., *High temperature/high pressure synthesis and crystal structure of the new corundum related compound* $Zn_4Nb_2O_9$*.* Solid state sciences, 2003. **5**(3): p. 459-463.
86. Friesen, C. and C. Thompson, *Reversible stress relaxation during precoalescence interruptions of Volmer-Weber thin film growth.* Physical review letters, 2002. **89**(12): p. 126103.
87. He, Y., *Heat capacity, thermal conductivity, and thermal expansion of barium titanate-based ceramics.* Thermochimica Acta, 2004. **419**(1-2): p. 135-141.
88. Touloukian, Y., et al., *Thermophysical properties of matter-the TPRC data series. Thermal expansion metallic elements and alloys.* 1975, Thermophysical and electronic properties infomation analysis center.
89. Seko, A., et al., *Pressure-induced phase transition in ZnO and ZnO−MgO pseudobinary system: A first-principles lattice dynamics study.* Physical Review B, 2005. **72**(2): p. 024107.
90. Ye, Z.-G., *Handbook of advanced dielectric, piezoelectric and ferroelectric materials: Synthesis, properties and applications*. 2008: Elsevier.
91. Madsen, M., et al., *Accounting for PDMS shrinkage when replicating structures.* Journal of Micromechanics and Microengineering, 2014. **24**: p. 127002.
92. Ozmen, O., C. Ozsoy-Keskinbora, and E. Suvaci, *Chemical stability of* $KNbO_3$*,* $NaNbO_3$*, and* $K_{0.5}Na_{0.5}NbO_3$ *in aqueous medium.* Journal of the American Ceramic Society, 2018. **101**(3): p. 1074-1086.
93. Sreenivas, K., et al., *Investigation of Pt/Ti bilayer metallization on silicon for ferroelectric thin film integration.* Journal of Applied Physics, 1994. **75**(1): p. 232-239.
94. Chambers, S.A., *Structure of thin epitaxial oxide films and their surfaces*. Oxide Surfaces. Vol. 9. 2001, Amsterdam. 301-325.
95. Ishizawa, N., et al., *Structural evolution of* $Na_{0.5}K_{0.5}NbO_3$ *at high temperatures.* Journal of Solid State Chemistry, 2010. **183**: p. 2731.
96. Okada, Y. and Y. Tokumaru, *Precise determination of lattice parameter and thermal expansion coefficient of silicon between 300 and 1500 K.* Journal of Applied Physics, 1984. **56**(2): p. 314-320.
97. Malič, B., et al., *Linear thermal expansion of lead-free piezoelectric* $K_{0.5}Na_{0.5}NbO_3$ *ceramics in a wide temperature range.* Journal of the American Ceramic Society, 2011. **94**(8): p. 2273-2275.
98. Irle, E., R. Blachnik, and B. Gather, *The phase diagrams of* Na_2O *and* K_2O *with* Nb_2O_5 *and the ternary system* $Nb_2O_5\text{-}Na_2O\text{-}Yb_2O_3$*.* Thermochimica Acta, 1991. **179**: p. 157-169.

Appendix A Zinc oxide thin films

A.1 Grain size and thickness of the ZnO thin film

SEM image of the surface of the ZnO thin film produced using the 0.27 M precursor solution with size measurement of a few grains is displayed in Figure A.1. The grain size varied from ~49 nm to ~230 nm.

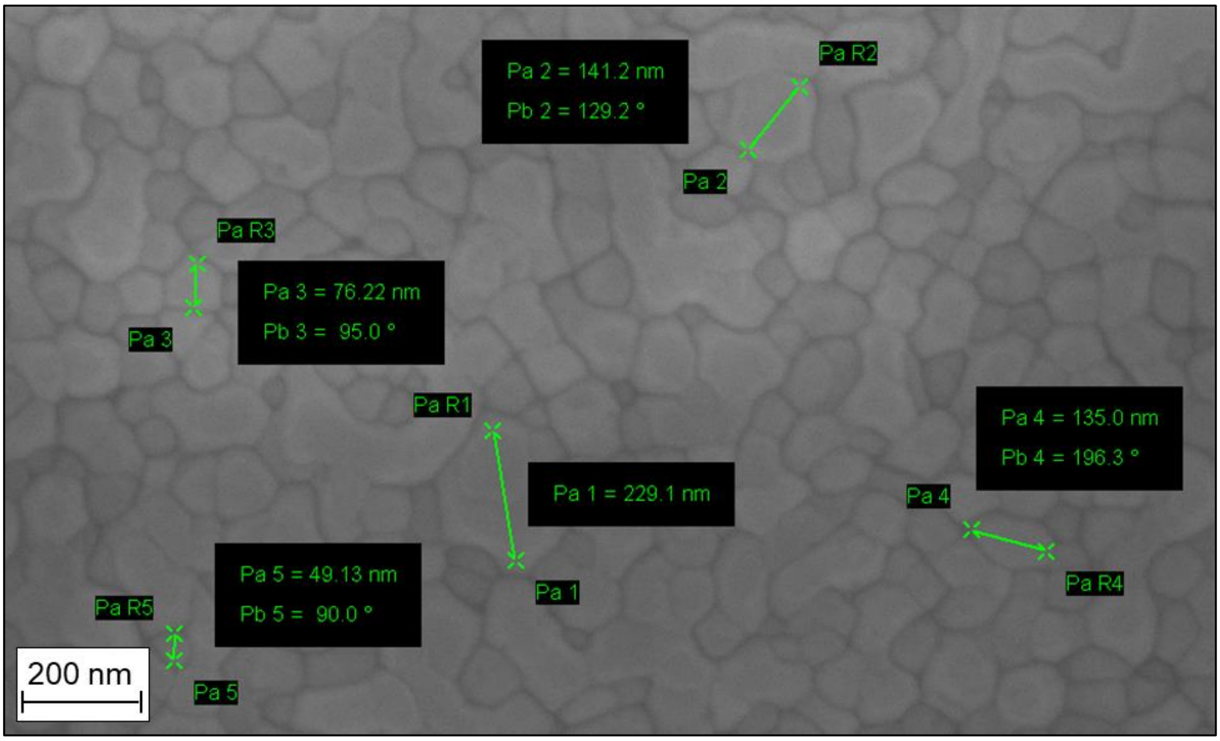

Figure A.1: SEM image of the surface of the ZnO thin film produced using the 0.27 M precursor solution with size measurement of a few grains. The grain size varies from ~49 nm to ~230 nm.

SEM image of the cross section of the ZnO-SiPt samples with measurement of the film thickness are displayed in Figure A.2 and Figure A.3. The thickness of the thin film made by the 0.29 M precursor solution varied from ~104 nm to ~111 nm, while the thickness of the thin film produced using the 0.27 M precursor solution varied from ~134 nm to ~136 nm.

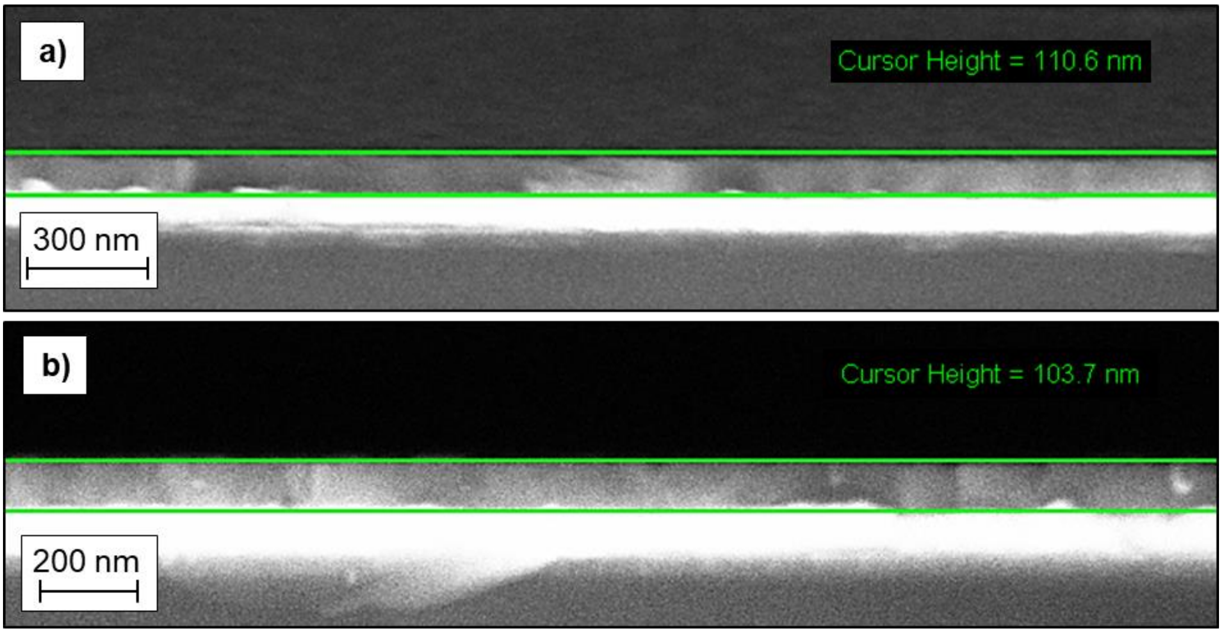

Figure A.2: SEM image of the cross section of the ZnO thin film produced using the 0.29 M precursor solution with measurement of the height of the thin film. The thickness of the thin film varies from ~104 nm to ~111 nm.

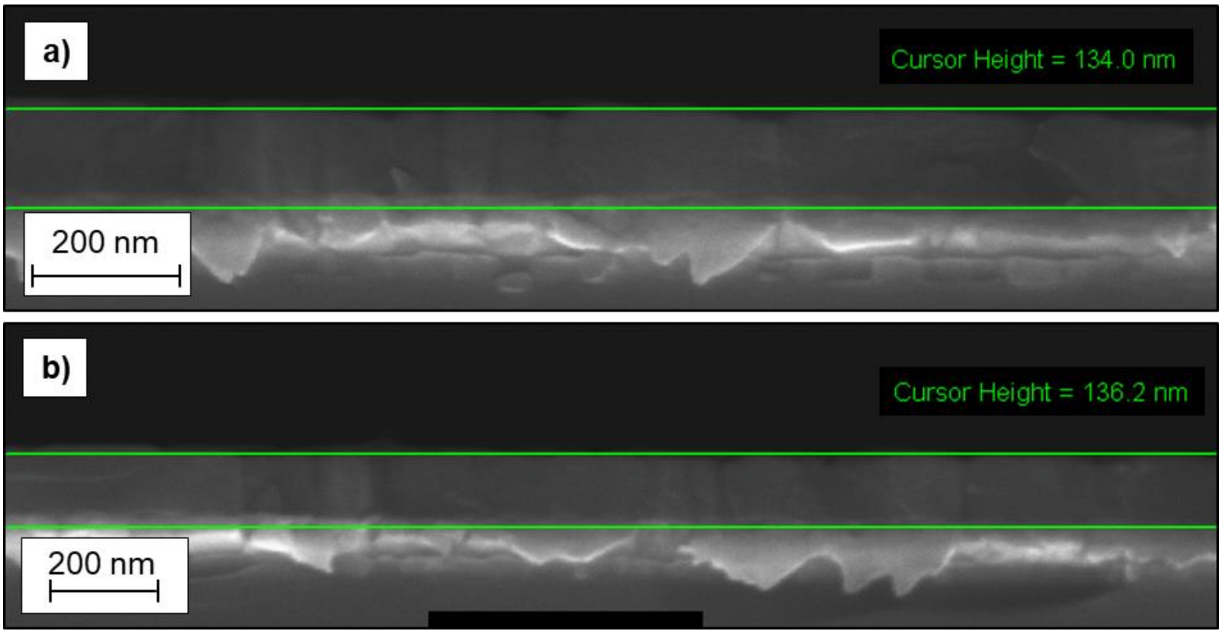

Figure A.3: SEM image of the cross section of the ZnO thin film produced using the 0.27 M precursor solution with measurement of the height of the thin film. The thickness of the thin film varies from ~134 nm to ~136 nm.

A.2 The effect of temperature on the surface morphology

Surface images of the ZnO thin film after pyrolysis at 550 °C and after annealing at 700 °C obtained by SEM, displayed in Figure A.4 a) and Figure A.4 b) respectively. After pyrolysis at 550 °C, the surface is porous with some elongated grains. The surface of ZnO thin film after annealing at 700 °C is displayed for comparison.

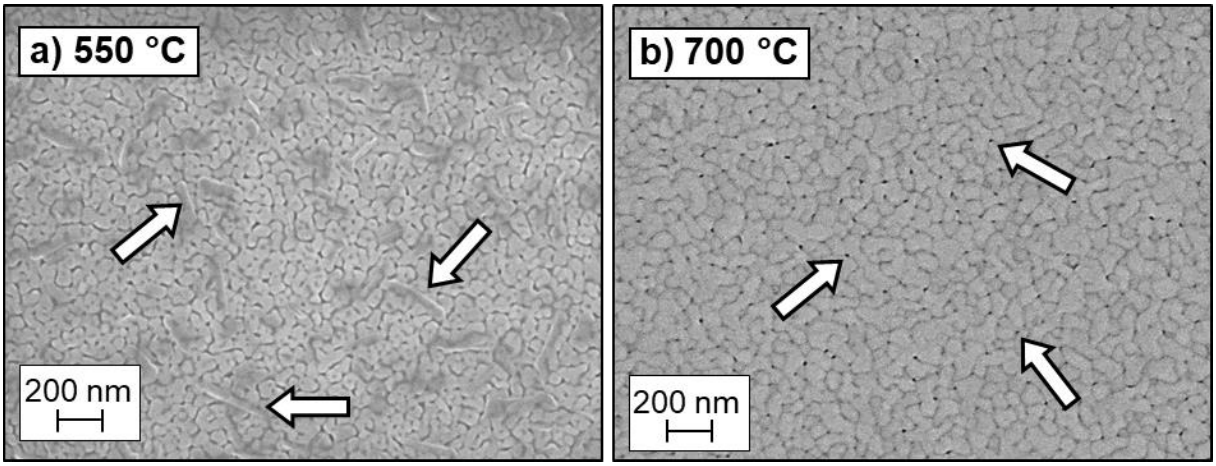

Figure A.4: SEM images of the surface of the ZnO thin film made by the same ZnO precursor solution before and after annealing. a) The film after pyrolysis at 550 °C. Image shows a porous surface with some elongated grains, indicated by white arrows. b) Surface image after annealing at 700 °C displayed for comparison. The surface looks dense with some small pores, indicated by white arrows.

The GI-XRD pattern of the ZnO thin film on a SiPt substrate after pyrolysis at 550 °C are displayed in Figure A.5, including the Miller indices for ZnO from PDF card 01-070-8070. All the new Bragg reflections for the ZnO film can be assigned to the indexed diffraction lines of ZnO or SiPt. The highest diffraction intensities for ZnO are observed at and at 2θ = 63°. The reflection observed at 2θ = 56.5° can be assigned the substrate.

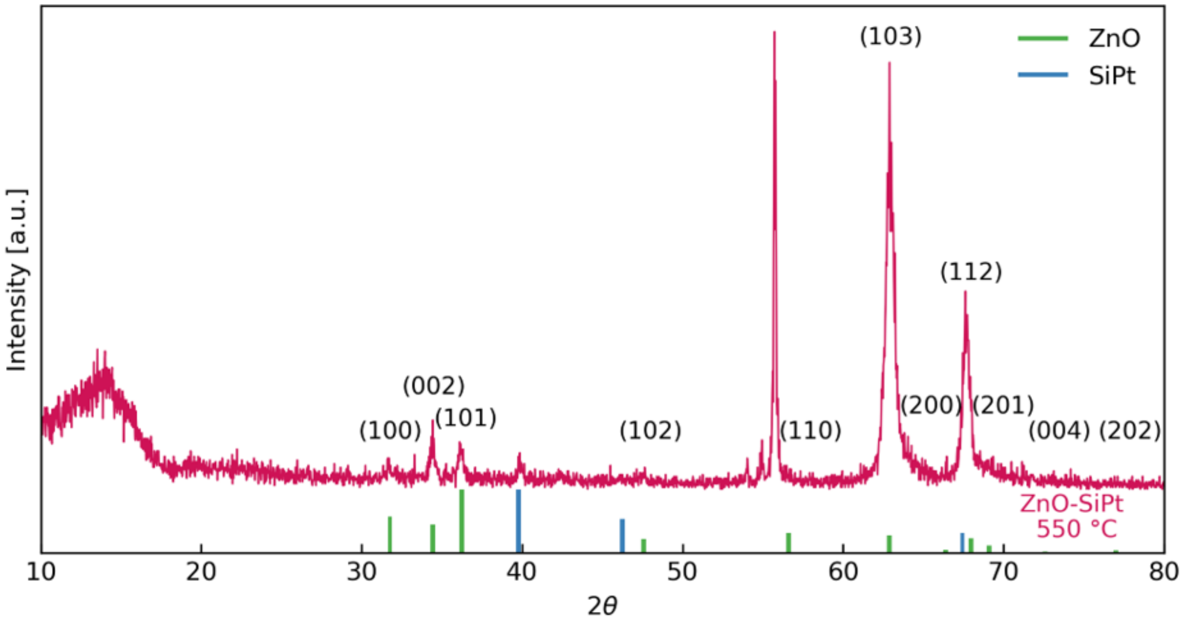

Figure A.5: GI-XRD pattern of the ZnO thin film on SiPt substrate after pyrolysis at 550 °C. The highest diffraction intensities for ZnO are observed at 2θ = 63° and at 2θ = 68°. The reflection observed at 2θ = 56.5° belong to the substrate. All the Bragg reflections from the ZnO film can be assigned to the diffraction lines of ZnO (green lines, PDF card 01-070-8070 [74]) or SiPt (blue lines, PDF card 00-004-0802 [75]). Only the diffraction lines above 20 % for SiPt are included.

Appendix B Barium titanate thin films

B.1 Thickness of the BT thin film

SEM image of the cross section of the BT-ZnO-SiPt sample with measurement of the film thickness are displayed in Figure B.1. The thickness of the BT layer is estimated to vary from ~25 nm to ~32 nm based on the measurement of the entire BT-ZnO layer and the ZnO thin film (0.29 M in Figure A.2).

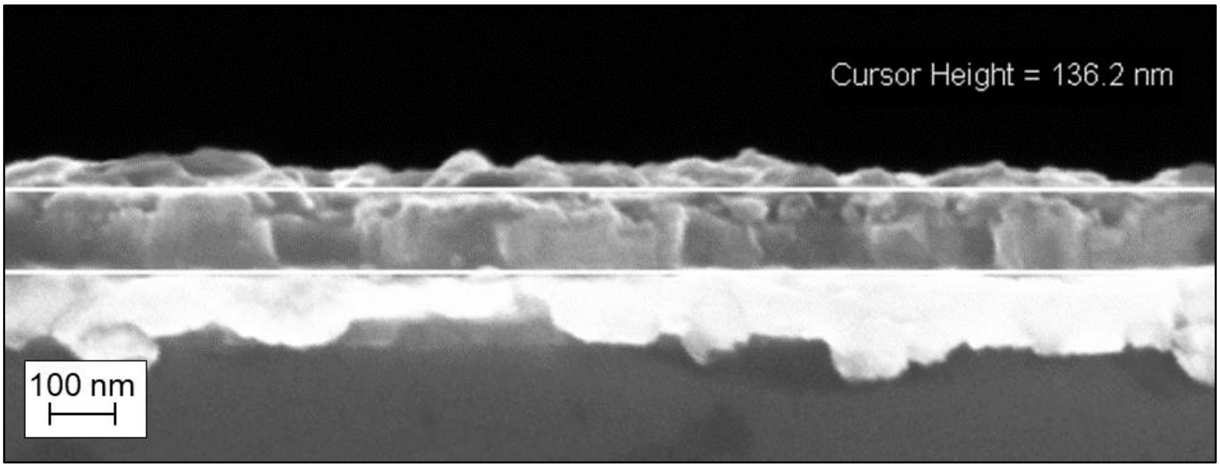

Figure B.1: SEM image of the cross section of the BT-ZnO-SiPt sample. The thickness of the BT layer is estimated to vary from ~25 nm to ~32 nm based on the measurement of the entire BT-ZnO layer and the ZnO thin film (0.29 M in Figure A.2).

B.2 IR spectra

The infrared (IR) reflectance spectra of the BT-ZnO-SiPt sample is displayed in Figure B.2. Presence of $BaTiO_3$ was observed around 500 cm^{-1} and 700 cm^{-1}, indicated with red arrows. The ZnO layer was observed around 570 cm^{-1} and the oxycarbonate phases, normally observed around 1400 cm^{-1} were absent in the spectra.

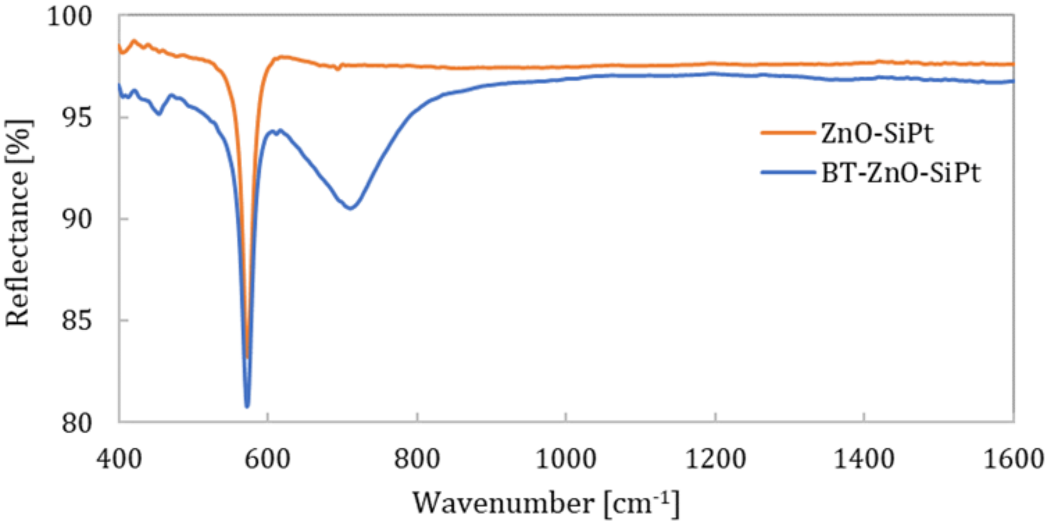

Figure B.2: IR spectra of $BaTiO_3$-ZnO-SiPt thin film. Presence of $BaTiO_3$ was observed around 500 cm^{-1} and 700 cm^{-1}, indicated with red arrows. The ZnO layer was observed around 570 cm^{-1} and the oxycarbonate phases were expected to be observed around 1400 cm^{-1}.

Appendix C Potassium sodium niobate thin films

C.1 Grain size and thickness of the KNN thin film

Size measurement of a few grains on the KNN surface obtained by SEM is displayed in Figure C.1 and Figure C.2. The diameter of the grains varied from ~30 nm to ~185 nm.

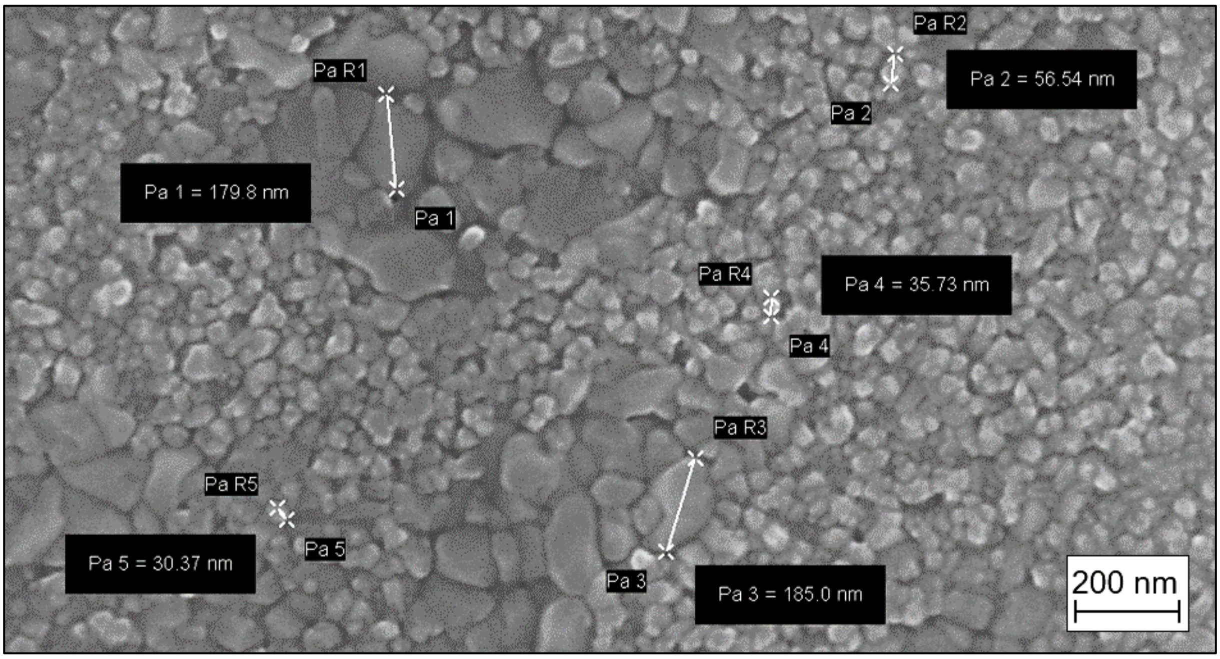

Figure C.1: SEM image of the surface of the KNN thin film with size measurements of a few grains. The diameter varies from ~30 nm to ~185 nm.

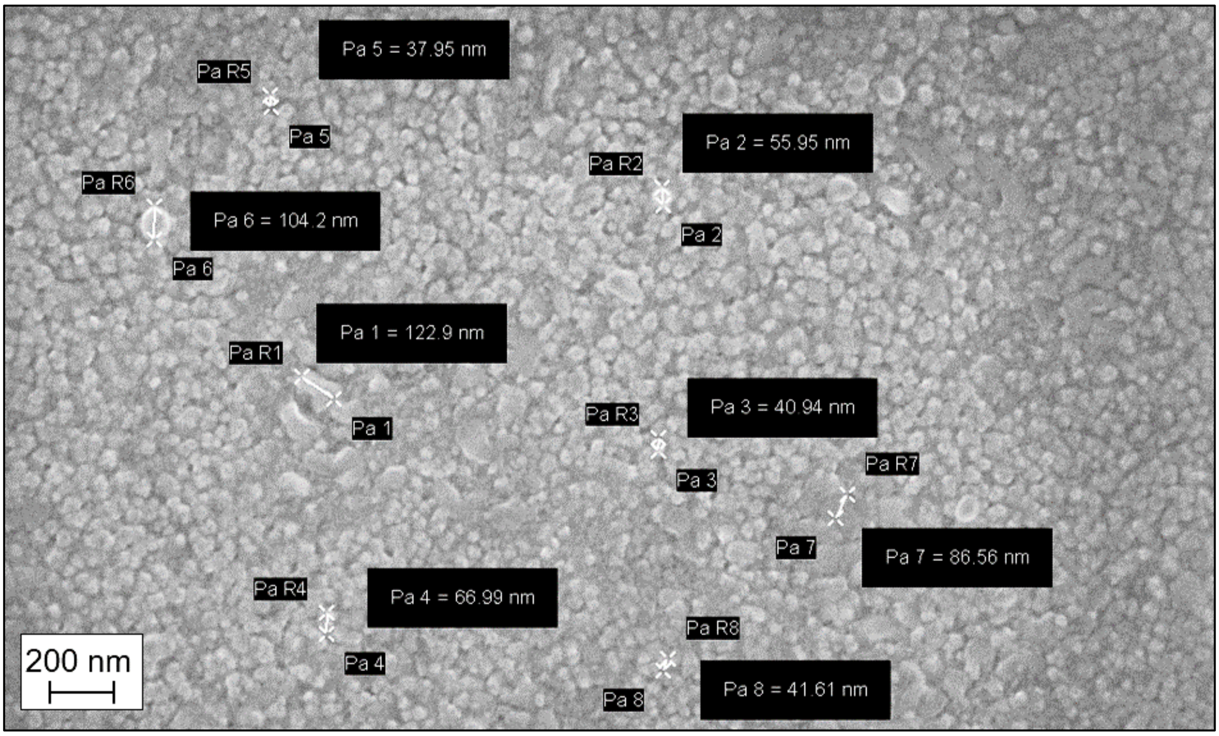

Figure C.2: SEM image of the surface of the KNN thin film with size measurements of a few grains. The diameter varies from ~38 nm to ~123 nm.

SEM images of the cross section of the KNN-BT-ZnO-SiPt sample with measurement of the film thickness are displayed in Figure C.3. The thickness of the KNN-BT layer varied from ~119 to ~124 nm.

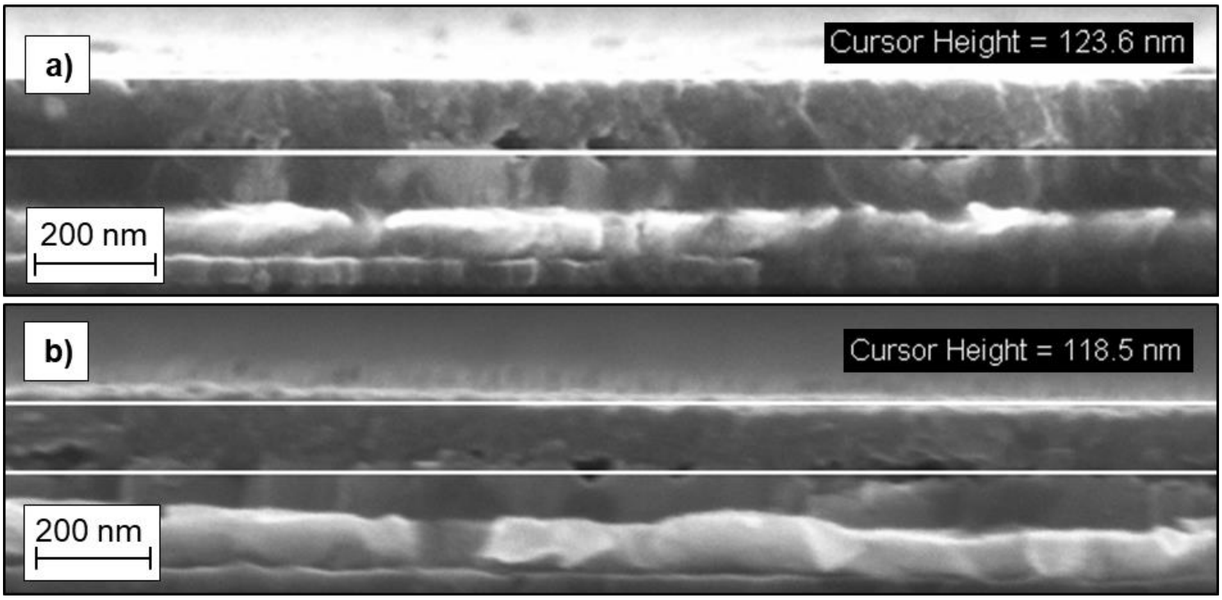

Figure C.3: SEM image of the cross section of the KNN-BT-ZnO-SiPt sample. The thickness of the KNN-BT layer varies from ~119 nm to ~124 nm.

C.2 KNN precursor solution

The XRD patterns of the powder from the KNN precursor solution. All the new Bragg reflections from the KNN film can be assigned to the indexed diffraction lines of $K_{0.5}Na_{0.5}NbO_3$.

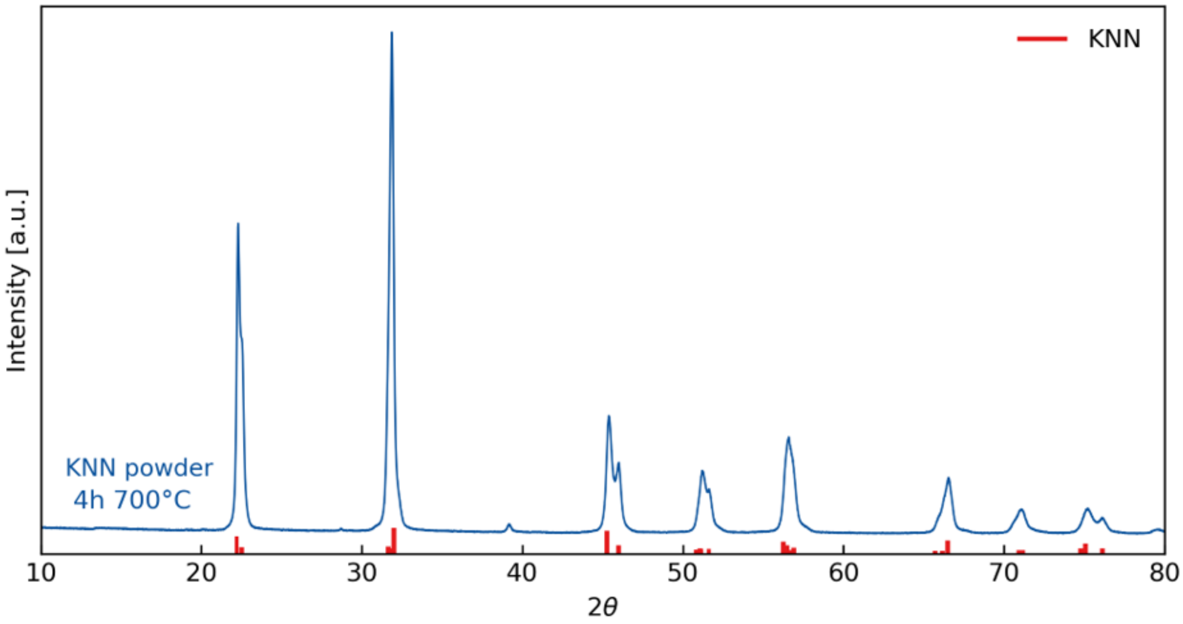

Figure C.4: The XRD patterns of the powder from the KNN precursor solution. All the new Bragg reflections from the KNN film can be assigned to the indexed diffraction lines of $K_{0.5}Na_{0.5}NbO_3$.

C.3 Effect of atmosphere and temperature on heat treatment of KNN thin films

The GI-XRD pattern of the KNN thin film on ZnO-SiPt after heat treatment in oxygen atmosphere is displayed in Figure C.5. All the new Bragg reflections from the KNN film can be assigned to the indexed diffraction lines of $K_{0.5}Na_{0.5}NbO_3$, $K_4Nb_6O_{17}$, ZnO or SiPt.

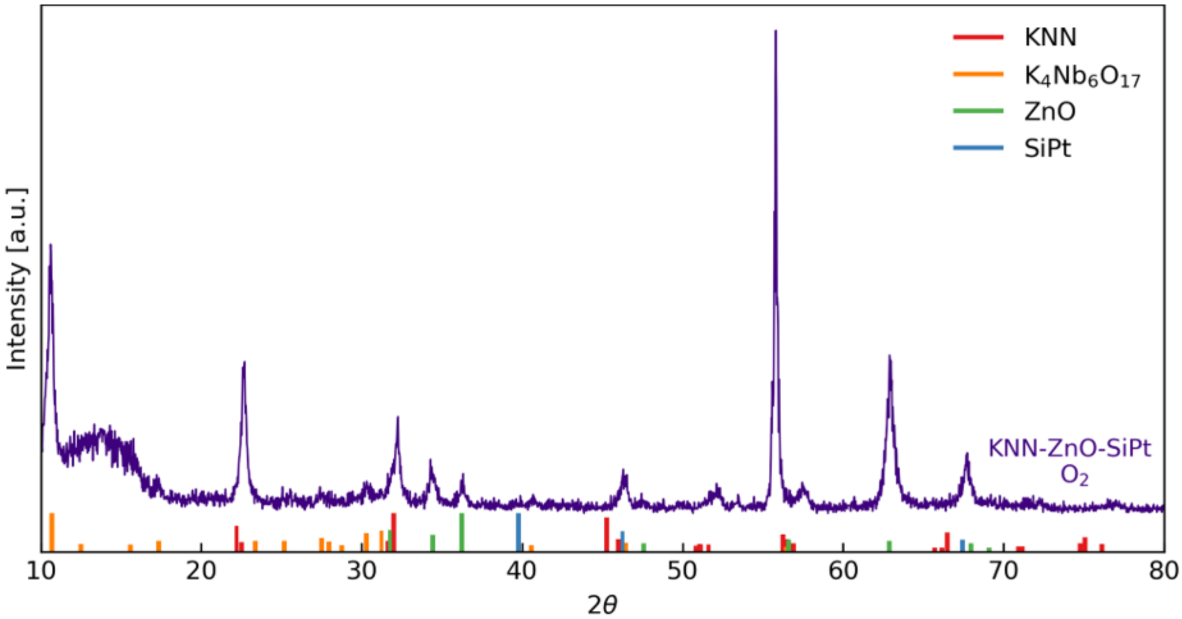

Figure C.5: GI-XRD pattern for the KNN-ZnO-SiPt sample heat treated in oxygen atmosphere. All the new Bragg reflections from the KNN film can be assigned to the indexed diffraction lines of $K_{0.5}Na_{0.5}NbO_3$ (red lines, PDF card 00-061-0315 [34]), $K_4Nb_6O_{17}$ (orange lines [77]), ZnO (green lines, PDF card 01-070-8070 [74]) or SiPt (blue lines, PDF card 00-004-0802 [75]). Only the diffraction lines above 20 % for $K_4Nb_6O_{17}$ and SiPt are included.

Surface images of the KNN thin film heat treated in O_2 obtained by SEM are displayed in Figure C.6. Elongated grains assigned to $K_4Nb_6O_{17}$ are observed in between the $K_{0.5}Na_{0.5}NbO_3$ grains, indicated with white arrows.

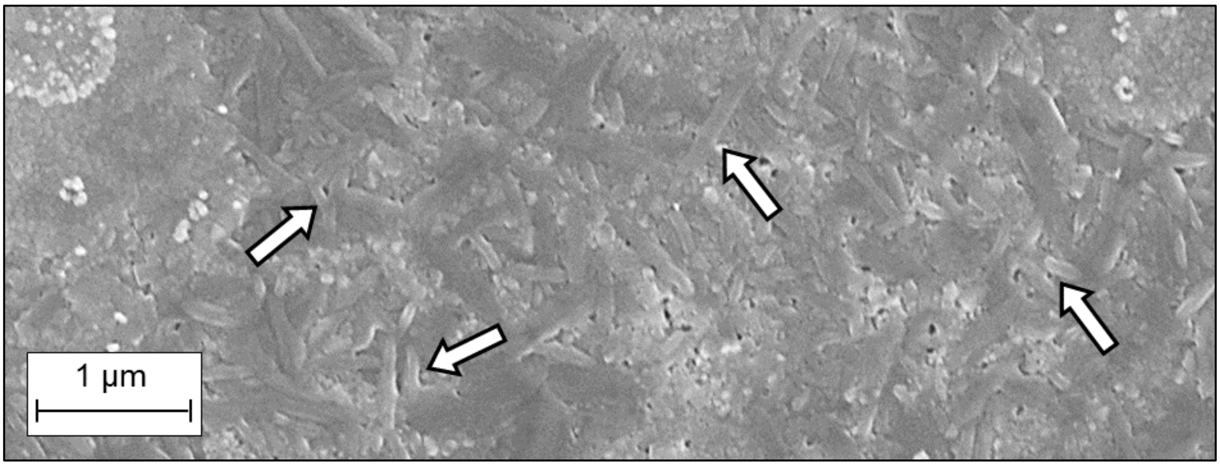

Figure C.6: SEM image of the surface of the KNN thin film heat treated in O_2. Elongated grains assigned to $K_4Nb_6O_{17}$ are observed in between the $K_{0.5}Na_{0.5}NbO_3$ grains, indicated with white arrows.

The GI-XRD pattern of the KNN thin film on ZnO-SiPt after heat treatment in a mixture of oxygen and nitrogen atmosphere is displayed in Figure C.7. All the new Bragg reflections from the KNN film can be assigned to the indexed diffraction lines of $K_{0.5}Na_{0.5}NbO_3$, $K_4Nb_6O_{17}$, ZnO or SiPt.

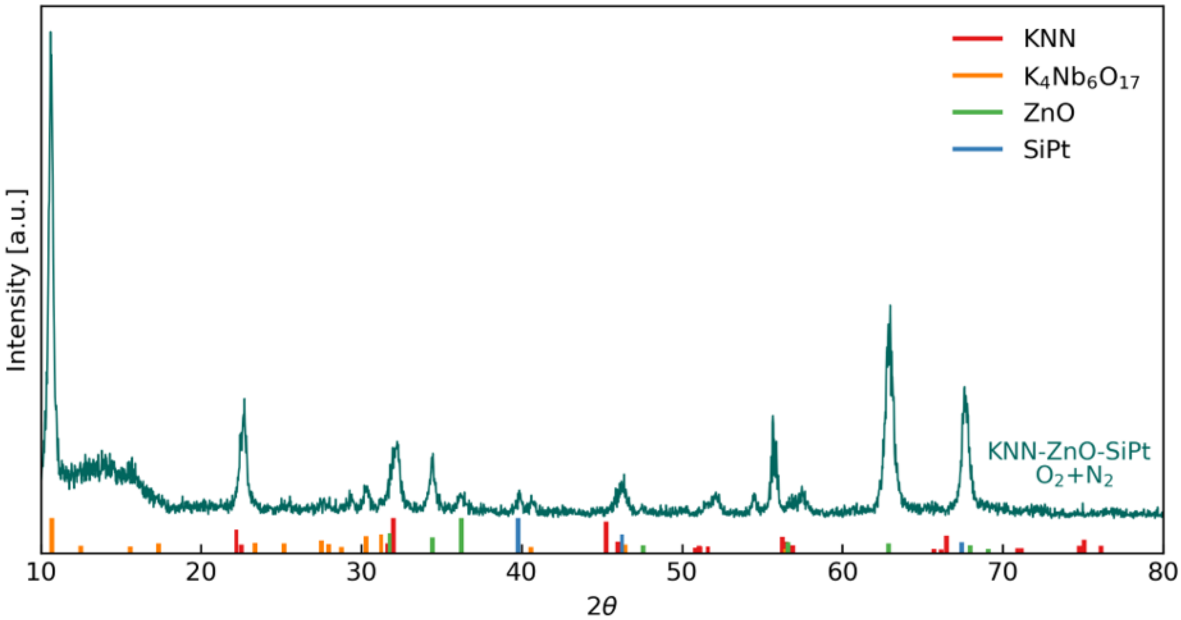

Figure C.7: GI-XRD pattern for the KNN-ZnO-SiPt sample heat treated in an atmosphere consisting of an 80/20 mixture of nitrogen and oxygen. All the new Bragg reflections from the KNN film can be assigned to the indexed diffraction lines of $K_{0.5}Na_{0.5}NbO_3$ (red lines, PDF card 00-061-0315 [34]), $K_4Nb_6O_{17}$ (orange lines [77]), ZnO (green lines, PDF card 01-070-8070 [74]) or SiPt (blue lines, PDF card 00-004-0802 [75]).

Surface images of the KNN thin film heat treated in an 80/20 mixture of N_2 and O_2 obtained by SEM are displayed in Figure C.8. Elongated grains assigned to $K_4Nb_6O_{17}$ are observed in between areas with $K_{0.5}Na_{0.5}NbO_3$ grains, indicated with white arrows.

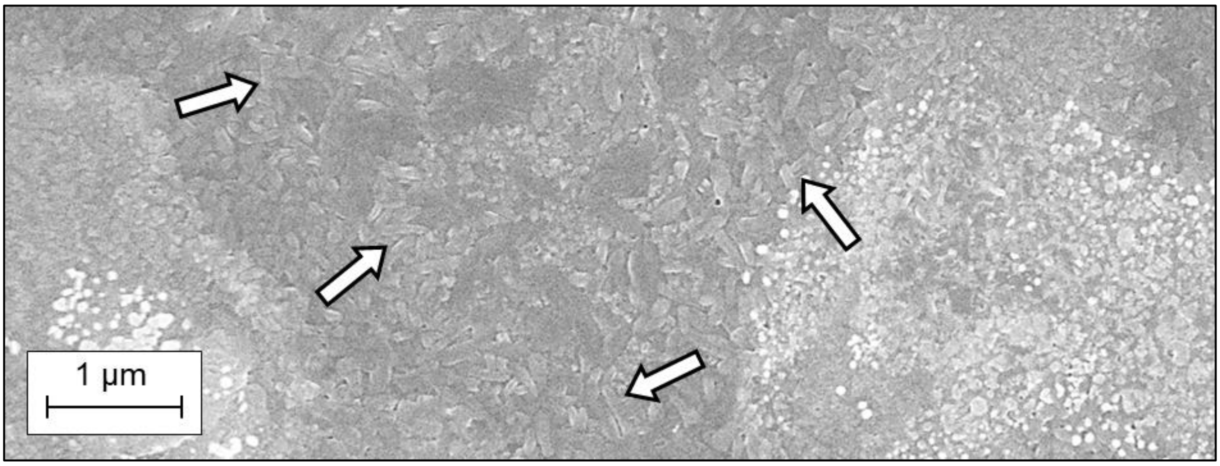

Figure C.8: SEM image of the surface of the KNN thin film heat treated in an atmosphere consisting of an 80/20 mixture of nitrogen and oxygen. Secondary phases are indicated with the white arrows.

The GI-XRD pattern of the KNN thin film on SiPt with the same precursor solution that was used for the KNN thin films presented prior is displayed in Figure C.9. The sample consists of 30 layers of KNN precursor solution deposited on a platinum coated silicon substrate. All the new Bragg reflections from the KNN film can be assigned to the indexed diffraction lines of $K_{0.5}Na_{0.5}NbO_3$ or SiPt. The sample was prepared by Ph.D. Nikolai Helth Gaukås.

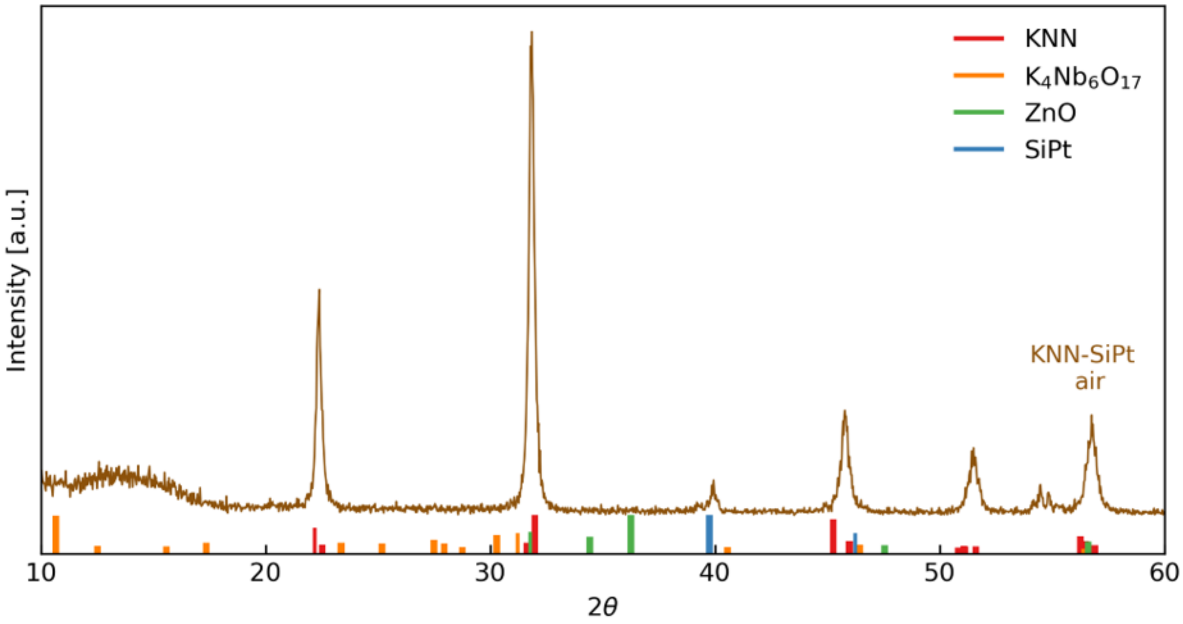

Figure C.9: GI-XRD pattern KNN-SiPt sample heat treated in air. All the new Bragg reflections from the KNN film can be assigned to the indexed diffraction lines of $K_{0.5}Na_{0.5}NbO_3$ (red lines, PDF card 00-061-0315 [34]) and SiPt (blue lines, PDF card 00-004-0802 [75]). The sample was prepared by Ph.D. Nikolai Helth Gaukås.

The GI-XRD pattern of the KNN thin film on ZnO-SiPt after annealing at 750 °C is displayed in Figure C.10. The corresponding pattern for KNN-ZnO-SiPt annealed at 700 °C is included for comparison. Nucleation of a new secondary phase; $K_2Nb_4O_{11}$ is observed at $2\theta = 15.9°$ and between $2\theta = 22°$ and $2\theta = 30°$, indicated with red arrows. All the new Bragg reflections for the KNN film can be assigned to the indexed diffraction lines of $K_{0.5}Na_{0.5}NbO_3$, $K_2Nb_4O_{11}$, ZnO or SiPt.

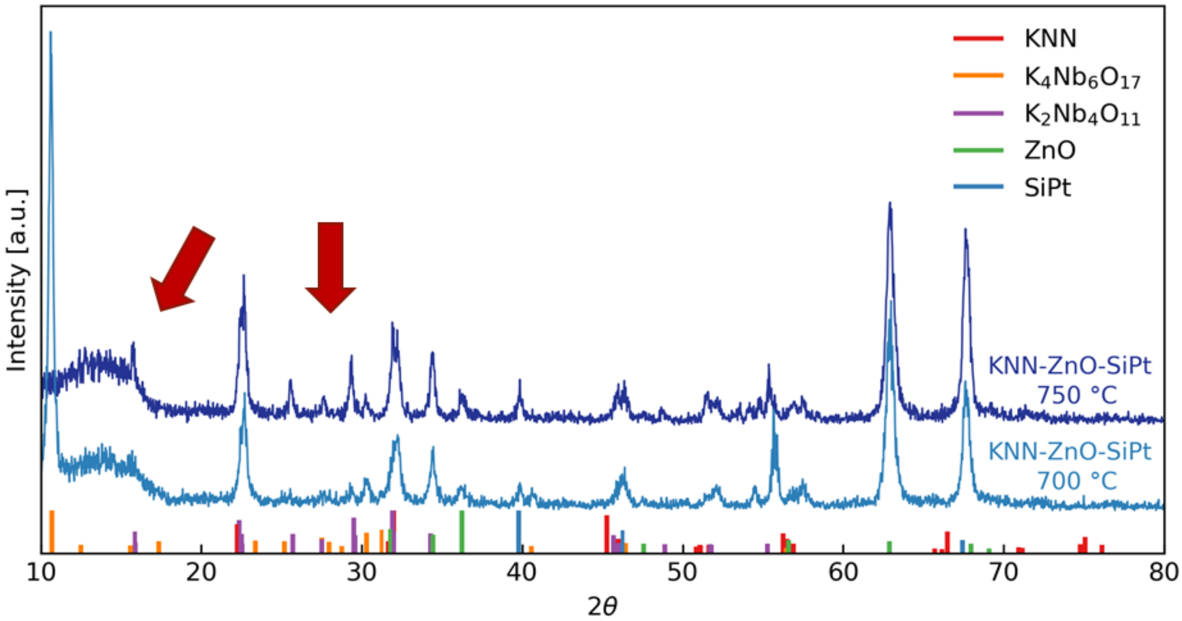

Figure C.10: GI-XRD pattern of the KNN-ZnO-SiPt thin film annealed at 750 °C. The GI-XRD pattern of the KNN-ZnO-SiPt thin film annealed at 700 °C is included for comparison. Nucleation of a new secondary phase; $K_2Nb_4O_{11}$ is observed, indicated with red arrows. All the Bragg reflections from the KNN film can be assigned to the indexed diffraction lines of $K_{0.5}Na_{0.5}NbO_3$ (red lines, PDF card 00-061-0315 [34]), $K_2Nb_4O_{11}$ (purple lines [82]), ZnO (green lines, PDF card 01-070-8070 [74]) or SiPt (blue lines, PDF card 00-004-0802 [75]).

C.4 Lattice mismatch between the BT and KNN layers

The lattice mismatch, measured in strain percentage, between the KNN thin film on top of the BT thin film calculated to be – 0.96 % using Equation C-1 [94]. The strain percentage is the induced strain between the BT and the KNN layer due to lattice mismatch, a_{KNN} is the lattice parameter for cubic KNN [95] and a_{BT} is the lattice parameter for cubic BT [76].

$$\% \, strain = \frac{a_{KNN} - a_{BT}}{a_{BT}} \cdot 100 \qquad \text{C-1}$$

$$\% \, strain = \frac{3.994 \text{ Å} - 4.031 \text{ Å}}{4.031 \text{ Å}} \cdot 100 = -0.96 \,\%$$

Appendix D Flexible KNN thin film

D.1 SEM images from the KNN-PDMS sample

Surface images of the flexible KNN thin film on PDMS support are displayed in Figure D.1 and Figure D.2. Severe fractures across the entire surface of the film were observed. The PDMS layer was cured at 60 °C for 4 h and the release process in 33 % acetic acid took ~2 h.

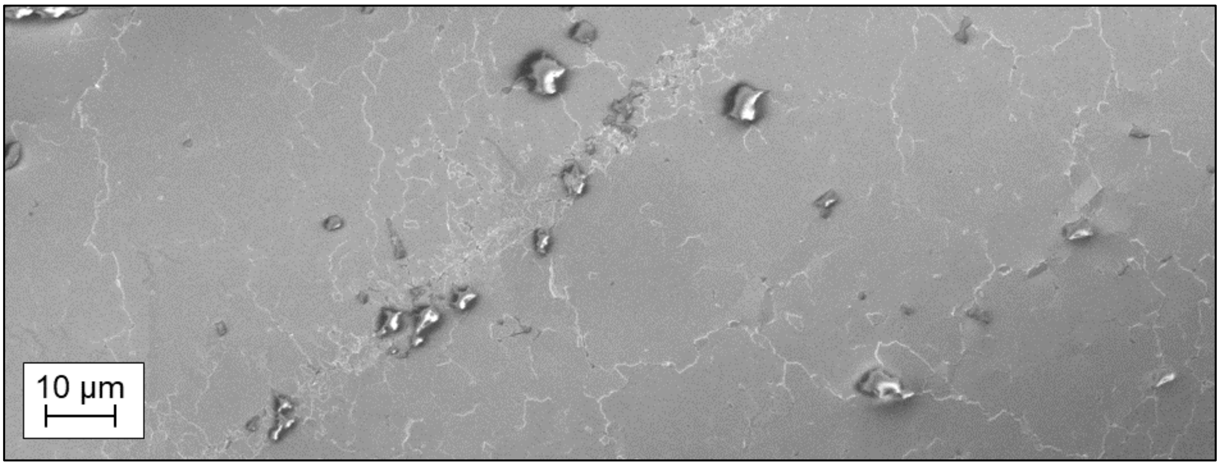

Figure D.1: SEM image of the surface of the KNN-PDMS sample at low magnitude. Severe fractures are observed across the entire surface.

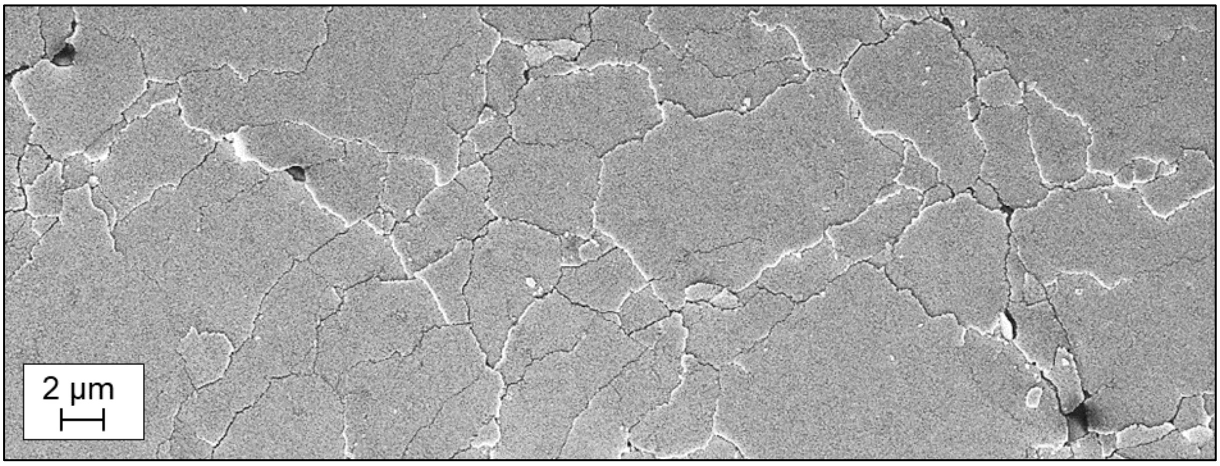

Figure D.2: SEM image of the surface of the KNN-PDMS sample at high magnitude. Severe fractures are observed across the entire surface.

Appendix E Thermal expansion

The measured thermal expansion coefficients, α, for silicon (Si), zinc oxide (ZnO), barium titanate ($BaTiO_3$), potassium sodium niobate ($K_{0.5}Na_{0.5}NbO_3$), sodium niobate ($NaNbO_3$) and potassium niobate ($KNbO_3$) are listed in Table E.1. In the KNN-BT-ZnO-SiPt sample, the thermal expansion coefficient increases in the following order: $\alpha_{Si} < \alpha_{KNN} < \alpha_{ZnO} < \alpha_{BT}$.

Table E.1: A list of all the measured thermal expansion coefficients, α, for silicon (Si), zinc oxide (ZnO), barium titanate ($BaTiO_3$), potassium sodium niobate ($K_{0.5}Na_{0.5}NbO_3$), sodium niobate ($NaNbO_3$) and potassium niobate ($KNbO_3$).

Material	**Temperature [°C]**	**Thermal expansion coefficient, α [$\cdot 10^{-6}$]**	**Ref.**
Si	27 – 1227	2.59	[96]
ZnO	27 –	5.63	[88]
$BaTiO_3$	150 – 200	11.34	[87]
$K_{0.5}Na_{0.5}NbO_3$	30 – 790	4.72*	[97]
$NaNbO_3$	350 – 800	10.28*	[98]
$KNbO_3$	350 – 800	4.67*	[98]

* Average value

NTNU
Norwegian University of
Science and Technology